Western University
Scholarship@Western

Digitized Theses | Digitized Special Collections

1977

A Study Of Meteor Trail Structure Using A Wide-aperture Antenna Array At High Radio Frequencies

Robert William Herring

Follow this and additional works at: https://ir.lib.uwo.ca/digitizedtheses

Recommended Citation
Herring, Robert William, "A Study Of Meteor Trail Structure Using A Wide-aperture Antenna Array At High Radio Frequencies" (1977). *Digitized Theses*. 1039.
https://ir.lib.uwo.ca/digitizedtheses/1039

This Dissertation is brought to you for free and open access by the Digitized Special Collections at Scholarship@Western. It has been accepted for inclusion in Digitized Theses by an authorized administrator of Scholarship@Western. For more information, please contact tadam@uwo.ca, wlswadmin@uwo.ca.

National Library of Canada

Cataloguing Branch
Canadian Theses Division

Ottawa, Canada
K1A 0N4

Bibliothèque nationale du Canada

Direction du catalogage
Division des thèses canadiennes

NOTICE

The quality of this microfiche is heavily dependent upon the quality of the original thesis submitted for microfilming. Every effort has been made to ensure the highest quality of reproduction possible.

If pages are missing, contact the university which granted the degree.

Some pages may have indistinct print especially if the original pages were typed with a poor typewriter ribbon or if the university sent us a poor photocopy.

Previously copyrighted materials (journal articles, published tests, etc.) are not filmed.

Reproduction in full or in part of this film is governed by the Canadian Copyright Act, R.S.C. 1970, c. C-30. Please read the authorization forms which accompany this thesis.

AVIS

La qualité de cette microfiche dépend grandement de la qualité de la thèse soumise au microfilmage. Nous avons tout fait pour assurer une qualité supérieure de reproduction.

S'il manque des pages, veuillez communiquer avec l'université qui a conféré le grade.

La qualité d'impression de certaines pages peut laisser à désirer, surtout si les pages originales ont été dactylographiées à l'aide d'un ruban usé ou si l'université nous a fait parvenir une photocopie de mauvaise qualité.

Les documents qui font déjà l'objet d'un droit d'auteur (articles de revue, examens publiés, etc.) ne sont pas microfilmés.

La reproduction, même partielle, de ce microfilm est soumise à la Loi canadienne sur le droit d'auteur, SRC 1970, c. C-30. Veuillez prendre connaissance des formules d'autorisation qui accompagnent cette thèse.

THIS DISSERTATION
HAS BEEN MICROFILMED
EXACTLY AS RECEIVED

LA THÈSE A ÉTÉ
MICROFILMÉE TELLE QUE
NOUS L'AVONS REÇUE

A STUDY OF METEOR TRAIL STRUCTURE USING A WIDE-APERTURE ANTENNA ARRAY AT HIGH RADIO FREQUENCIES

by

Robert William Herring

Department of Physics

Submitted in partial fulfillment

of the requirements for the degree of

Doctor of Philosophy

Faculty of Graduate Studies

The University of Western Ontario

London, Canada

February, 1977

© Robert William Herring 1977

ABSTRACT

The diffraction patterns of radio meteor echoes propagated over a 911 km path at frequencies between 20 and 30 MHz have been spatially sampled and recorded using a 1.18 km linear antenna array. The temporal and spatial variations of the recorded amplitudes and phases of three such echoes were examined, and the spatial Fourier transforms of the data were computed to yield angular spectra, or information on echo amplitude as a function of angle of arrival. Detailed analysis of the angular spectra, which showed evidence of resolved secondary echoes, indicated that, in two of the three cases examined, the secondary echoes could have been due to trails caused by fragments from the meteoroid which generated the main echo trail. For all three cases, the observed motions of the deduced main and secondary echo reflection points could be explained on the basis of trail rotations caused by vertical shears in the neutral winds.

Descriptions of the experimental equipment and development of the necessary theory are also included.

ACKNOWLEDGEMENTS

There are many people to whom a great debt of gratitude is owed, or this thesis would not exist. These people were associated with either the University or the Communications Research Centre, or are members of my family.

At the University, I want to thank my advisory committee members, namely Professors P.A. Forsyth, D. Moorcroft, G.F. Lyon and Y.P. Bow for their constructive criticisms, guidance and support during the course of this project. That their counsel sometimes fell on deaf ears was not their fault. I want also to thank all the other members of the faculty and fellow graduate students who shared many cups of coffee and words of wisdom with me.

Without the aid and support of many colleagues at the Communications Research Centre (CRC), I would never have begun this project. It was Mr. C. Collins, now retired, who originally encouraged me to go to Western, and made arrangements for the generous level of financial support I enjoyed while there. His quiet words of support were always greatly appreciated. Other members of the CRC who provided valuable assistance were Dr. D.W. Rice, who patiently explained how his receivers worked; Mr. L. Thiele, who patiently kept them operational, right up to the time he quit to go back farming for a living; and Mr. E.L. Winacott, Mr. R. Bourdon and Mr. J.P. Raymond, who looked after such diverse aspects of the system as the receiving antennas, the antenna cables, the clock, the A/D converter and the complete computing system hardware. Last, but certainly not least, I must thank Mr. J. Griffin, who gave up

his usual quiet New Year's celebration to travel alone to Sept. Iles, P.Q., where he operated the transmitter system on the 2nd and 3rd of January 1973. Without the efforts of all these people, no data could have been recorded. Thanks are also due to Dr. G. Atkinson, with whom I shared an office and many lively discussions for a year and a third after my return to CRC.

On the home front, much support and encouragement was forthcoming both from my parents and from my wife, Judy. The death of my Father, in November 1973, was a loss deeply felt, as he was always a source of optimism and support. It is to him that I dedicate this thesis. To all three of my immediate family, who had to put up with the manic-depressive cycles of a thesis writer, I offer my gratitude and thanks, and love.

Finally, it is with pleasure that I acknowledge and thank the Department of Communications for allowing me to take advantage of their almost excessively generous educational leave program over the period September 1971 to August 1974. Their financial support was greatly appreciated, especially by Judy, who was thus able to pursue her own academic career (M.B.A.) instead of "putting hubby through" (P.H.T.).

TABLE OF CONTENTS

LIST OF TABLES

LIST OF FIGURES

The author of this thesis has granted The University of Western Ontario a non-exclusive license to reproduce and distribute copies of this thesis to users of Western Libraries. Copyright remains with the author.

Electronic theses and dissertations available in The University of Western Ontario's institutional repository (Scholarship@Western) are solely for the purpose of private study and research. They may not be copied or reproduced, except as permitted by copyright laws, without written authority of the copyright owner. Any commercial use or publication is strictly prohibited.

The original copyright license attesting to these terms and signed by the author of this thesis may be found in the original print version of the thesis, held by Western Libraries.

The thesis approval page signed by the examining committee may also be found in the original print version of the thesis held in Western Libraries.

Please contact Western Libraries for further information:
E-mail: libadmin@uwo.ca
Telephone: (519) 661-2111 Ext. 84796
Web site: http://www.lib.uwo.ca/

CHAPTER 1

HISTORICAL REVIEW AND BASIC DEFINITIONS

1.0 Introduction

Historically meteors have been subjects of awe and mystery: "shooting stars" or "falling stars" associated in superstitious minds with births, deaths and cataclysmic events in the affairs of mankind. Brilliant meteors capable of arousing such emotions are in fact relatively rare. The overwhelming majority are of small size and, causing no brilliant streak of light, they pass unseen by the human eye.

All but the tiny micro-meteors, however, leave a wake consisting of an elongated cloud or trail of ionized meteoric and atmospheric constituents. Often these trails contain sufficient numbers of free electrons to be capable of scattering radio waves. The study of the characteristics of radio waves scattered by these trails, or radio meteor echoes, has yielded much information not only about the rates of occurrence of otherwise invisible meteors, but also about the physics and chemistry of the upper atmosphere at heights of 80 to 120 km where the trails are formed.

The extra terrestrial particles which, heated to the point of disintegration by the frictional effect of passing through the earth's atmosphere, ablate and give rise to meteor phenomena are called meteoroids, and are encountered by the earth as it orbits around the sun. Meteoroids which manage to penetrate to the earth's surface are called meteorites. Along some parts of its orbit the earth encounters

regions of enhanced meteoroid density, which give rise to meteor showers. Meteoroids of a particular shower share a common orbit around the sun, and thus the paths of shower meteors when extrapolated back appear to originate from a common point in the sky, called the radiant. When the radiant is low in the sky, the earth's gravity deflects the paths of the meteoroids downwards so that the radiant seems higher than it should; this effect is called zenith attraction. The majority of all meteors which are not associated with any shower, are referred to as being sporadic.

1.1 Early Radio Observations of Meteors

According to McKinley (1961) in his excellent book "Meteor Science and Engineering", Skellett (1931, 1932) of the Bell Telephone Laboratories was the first person to suggest that the unexpected observations of suddenly occurring short-lived radio echoes at night, as seen for example by Appleton (1930) while observing the reflection of radio waves from the ionosphere, might be due to meteor ionization. An experiment to verify this hypothesis, by attempting to correlate the visual observations of meteors with the occurrence of transient radio echoes, was first tried during a meteor shower in the autumn of 1931 by Schafer and Goodall (1932). Unfortunately the sky over the radio apparatus was obscured by clouds, but the following year (1932) the experiment was repeated successfully by Skellett (1935) himself.

As reported by McKinley (1961), observational work using radio techniques that was carried out during the 1930's was done at frequencies in the range 1-10 MHz as an adjunct to ionospheric research, and usually the transmitter and receiver were located close to each other

in the backscatter configuration. As well, unexplained sporadic reception of forward scattered signals over long distances at unusually high frequencies were occasionally noted in the literature (e.g., L.F. Jones (1933) detected 44 MHz signals at a distance of 238 miles from the transmitter), and Pierce (1938) suggested that the propagation of these signals also might be due to meteor trail effects.

1.2 Basic Parameters of Radio Meteor Echoes

The occurrence of a particularly intense Giacobinid meteor shower in October 1946 coupled with the availability of superior electronic equipment, particularly radar, developed during the Second World War provided the impetus for the post-war surge of interest in the radio study of meteors. Two of the first reports containing measurements of some of the basic parameters of radio meteor echoes made using these radars were published by Hey and Stewart (1947) and Eastwood and Mercer (1948).

These basic parameters are: echo range, or the distance from the (backscatter) radio apparatus to the meteor trail; the rapidly fluctuating echo phase observed during the formation of a meteor trail due to the finite velocity of the meteoroid; echo amplitude or echo power, which are related to, among other factors, the quantity of ionization per unit of trail length, which in turn is related to the initial mass of the meteoroid, the meteoroid velocity, and the local atmospheric density; echo-decay time and echo duration which are related to the processes which act to disperse the trail, such as diffusion, winds and electron attachment and recombination; echo polarization, or the angle of the radio-wave electric-field vector to the trail axis;

and echo body-Doppler, which is the relatively small Doppler frequency shift of the echo signal observed for some echoes, due to the motion of the neutral atmosphere containing the trail.

1.3 Relevant Radio Meteor Research Since 1960

The vast amount of research undertaken in the field of radio observations of meteors since the Second World War defies being summarized in a work such as this; the reader is again referred to the book by McKinley (1961) for a comprehensive review and summary of the work carried out in the period 1945-1960.

There are, however, two general comments which can be made about most work done to date. The first is that almost all experimental studies have been statistical in nature: that is, large quantities of data were accumulated from observations of hundreds or even thousands of radio meteor echoes, and these data were then averaged in some reasonable manner to estimate the parameters desired. The second is that in no case were the spatial diffraction patterns formed by the scattered radio signals observed and studied in detail. At best, interferometric techniques were used to estimate angles of arrival of the scattered signal with respect to the receiving system (Revah, 1969; Brown, 1972) and where multiple element antenna systems were employed (Brown, 1972), the signals received by various sets of elements were summed electronically before they were detected, simply in order to reduce the beamwidth of the antenna system and hence to eliminate ambiguities which could arise in the analysis of the data.

Nevertheless there are several studies of sufficient relevance to the present experiment to warrant mention. Rice and Forsyth (1963, 1964) and Rice (1964) found anomolous variations in the echo decay times for the same trail as observed at three different radio frequencies. They showed by performing some numerical integrations that variations in the line density, or number of electrons per unit length of trail, of order 50% of the mean line density, and of linear extent one-tenth to one principal Fresnel zone diameter (Section 3.3) could account for these anomolies. These variations were hypothesized to be due to some unspecified mechanism which resulted in the irregular deposition of electrons along the trail as it was being formed. Rice therefore devised an experimental technique to measure the line density of the trail as it was being formed, and found evidence for the existence of the hypothesized fluctuations.

A paper by Jones (1969) called this result into question and suggested that the observed dispersion in decay times might instead be due to the distorting effects of second-order vertical gradients in the horizontal neutral winds on the trails after their formation. Jones and Read (1972) showed on the basis of a general theoretical calculation that such wind-shear-gradient effects could in fact explain the observed dispersion in decay times for forward-scatter measurements, such as were performed by Rice, but that backscatter decay-time dispersion measurements were probably completely contaminated by extra-terrestrial radio noise.

Brown and Elford (1971) also performed numerical calculations based on a meteor trail model which combined a random irregular line density profile and the effect of a linear vertical shear of the hori-

zontal winds. They showed that this model too could account for large variations in observed echo decay times, for reasonable estimates of fluctuation magnitude and scale size, and wind shear. Their finding that the effect of linear wind shears alone acting on a trail without any irregularities were insufficient to account for the observed spread in echo decay times had also been deduced analytically by McIntosh (1969).

Other experimental studies of the effects of wind shears on meteor trails have been of a more direct nature. Revah (1969) used a sophisticated meteor radar system to obtain copious data which were analyzed statistically to yield a continuous description of the wind profiles as a function of altitude and time. The major result derived was the demonstration of the existence of propagating internal gravity waves with periods of a few hours. Phillips (1969), in contrast, used a much simpler single antenna backscatter apparatus to observe the amplitude fluctuations in persistent meteor echoes. These data also were analyzed statistically to deduce that the observed fluctuations were consistent with the existence of a horizontal wind velocity profile which is a sinusoidal function of altitude, with the amplitude of the sinusoid increasing exponentially with altitude. The results of Revah and Phillips are thus not inconsistent, and provide solid evidence for the existence of significant wind shears and wind-shear gradients at meteor heights.

Finally, it would be remiss not to mention the extensive Meteor Research Program of the Smithsonian Astrophysical Observatory, which has been summarized in an extensive final report by Cook *et al.* (1972). This program included among its many experiments the simultaneous opti-

cal and radio observations of meteors. The conclusion of that particular study was that meteoroids fragment as they ablate, consistent with the conclusions both of other works cited above, and of the present thesis.

1.4 Outline of the Thesis

In Chapter 1 the basic radio meteor terminology and both the early history and the current state of radio meteor research are reviewed. In particular it is brought out that there are two possible mechanisms for explaining anomolous meteor echo behavior; distortion of the meteor trails due to gradients in the vertical shears of the horizontal winds, and irregularities in the line density of the trails.

Chapter 2 describes in some detail the equipment used in the current experiment, and the constraints which led to the particular choice of spatial coordinates chosen for the geometrical theory developed in Chapter 3.

Chapter 3 contains other elementary theory necessary to undertake the analysis of the experimental results. The theory for describing and interpreting the spatial diffraction patterns of meteor echoes received from straight and distorted meteor trails with uniform and irregular reflection coefficient profiles is developed, and the theory of underdense, transitional and overdense reflection coefficients is reviewed. The elementary theory developed there is expanded as required in Chapter 5, where the experimental results are described and analyzed in detail.

Chapter 4 outlines the experimental details of recording the data and the methods used to reduce the raw data to a form amenable to physical interpretation. A least-squares techniques for estimating the angles

of arrival of the echoes as well as spatial and temporal filtering techniques and the Fourier transform technique used to estimate the angles of arrival of the observed secondary echo components are described.

Chapter 5 contains the detailed analysis of the reduced data from three different echoes. The data are shown to contain evidence of the existence of small but significant spatially resolved secondary echoes. It seems likely that these secondary echoes cannot be due solely to the effects of vertical shears of horizontal winds acting on single trails. Therefore a hypothesis that the secondary echoes were due to trails caused by fragments being cast off the main meteoroid is considered. It is shown that this fragmentation hypothesis is capable of explaining the observations in two of the three cases analyzed, and in all three cases, the observed motion of the secondary echo reflection points are explainable on the basis of wind shears consistent with those deduced from other previous observations. However, there is an absence of independent corroborative evidence indicating the occurrence of meteoroid fragmentation at the deduced heights of more than 100 km and with the deduced angular divergences of the fragment paths of more than 1°. Hence the fragmentation hypothesis must as yet be considered speculative.

Chapter 6 contains a qualitative summary of the results and the conclusions which can be drawn from them, and casts them in perspective with the results of previous radio experiments and some current theories of meteoroid structure. The energetic and momentum constraints of meteoroid fragmentation are considered in an appendix and are shown not to preclude the fragmentation hypothesis. Finally, suggestions for further studies are made.

CHAPTER 2

INSTRUMENTATION

2.0 Introduction

The equipment of the Communications Research Centre (CRC) High-Frequency Direction-Finding (HFDF) research facility was used to perform this experiment. This facility, located about 15 miles southwest of Ottawa, was designed to sample and record wavefront data received across a 3875-foot (1181.1 m) aperture, at frequencies in the high-frequency (HF) radio band (2-30 MHz). Although the equipment was intended primarily for the observation of radio signals reflected by the ionosphere, for this experiment signals scattered by meteor trail ionization were sampled and recorded.

2.1 Outline of the System Design

The HFDF system consisted of an array of up to 90 antenna elements, each connected by a calibrated cable to its own receiver. The receivers shared common local oscillators, so that the relative phases of signals from the different antenna elements were preserved. The final stage of each receiver included a phase-sensitive detector, and the two output signals (differing in phase by 90°) from each receiver were quantized by an analog-to-digital converter and recorded on digital magnetic tape. The receivers and ancillary recording and control equipment were housed in an underground laboratory near the centre of the antenna array.

2.2 Swept-Frequency Continuous-Wave Modulation

The designers of the CRC HFDF system chose the somewhat novel technique of swept-frequency continuous-wave (SFCW) modulation rather than the more common pulse-modulation method of estimating signal-propagation delays. This choice profoundly affected the design of the system, and it therefore seems appropriate to describe the SFCW-modulation technique in some detail immediately.

As the description SFCW implies, the transmitted signal is continuous in nature, and has constant amplitude. Its frequency, however, is being increased or decreased linearly with time; i.e., the frequency is being swept. Such a signal can be generated at HF-band frequencies to a high degree of precision (with undesired sidebands 40 dB or more below the desired signal level) by means of specially constructed digitally controlled frequency synthesizers. In the CRC HFDF system, synthesizers manufactured by the Barry Research Corporation were used. Frequency sweep-rates ranging from 25 kHz/sec to 10 MHz/sec were available; for the present experiment a sweep-rate of 100 kHz/sec was chosen (Section 4.1).

2.2.1 Bandwidth considerations

SFCW modulation allows the use of receivers with output bandwidths much narrower than those required for pulse-modulation receivers, because the instantaneous bandwidth of the desired SFCW signal is much narrower than the bandwidth required to pass the typical 20 μsec to 100 μsec pulse used in HF radio observations of the ionosphere. The narrower bandwidth also improves the signal-to-noise ratio (SNR) at the receiver output. Of course, if the receiver bandwidths are made too

narrow, rapid fluctuations in the received signal due to rapid variations in the propagation path will be obscured. This presents a severe restriction on the observation of radio meteor echoes while the meteor trail is being formed, when the bandwidth of the fluctuations in the echo signal at HF can exceed 1 kHz.

2.2.2 Estimation of Propagation-Delay Times

If it is assumed that Doppler shifts at the received signal frequency are negligible, SFCW modulation offers the possibility of determining the transit time of the signal over the propagation path. A transmitted SFCW signal has instantaneous frequency f_T (in Hz) given by

$$f_T = f_o + st \quad (0 \leq t \leq t_1) \tag{2.1}$$

where f_o = initial frequency (in Hz) at the start of the signal ($t = 0$)

t = time (in sec)

t_1 = duration of signal (in sec),

and s = frequency sweep rate (in Hz/sec).

At a point distant from the transmitter such that the signal transit time is τ (and it is assumed for simplicity that only one propagation path, of constant length, exists), the instantaneous frequency of the received signal, f_R (in Hz), is given by

$$f_R = f_o + s(t-\tau) \quad (\tau \leq t \leq t_1 + \tau) \tag{2.2}$$

If the received signal is mixed with a replica of the transmitted signal generated by a SFCW local oscillator and the difference frequency

Δf (in Hz) is extracted, then Δf is proportional to τ:

$$\Delta f = f_R - f_T = -s\tau \quad (\tau \leq t \leq t_1) \tag{2.3}$$

Negative difference frequencies are observable if a phase-sensitive detector is employed.

The extension of this concept to include the detection of multiple propagation paths and the estimation of their relative signal strengths and transit times by some form of spectral analysis of the receiver output signal is obvious.

If the transmitter and receiver SFCW oscillators are perfectly synchronized, the observed difference frequencies are typically in the audio band; e.g., for τ = 3.20 msec (corresponding to a propagation path of about 960 km) and s = 100 kHz/sec, then Δf = -320 Hz. Because it is easier to construct low-pass filters than band-pass filters, it is usual to retard the start of the sweep of the receiver local oscillator to reduce the magnitude of Δf. Thus if the local oscillator frequency f_T' is given by

$$f_T' = f_o + s(t - \tau_o) \quad (\tau_o \leq t \leq t_1 + \tau_o) \tag{2.4}$$

where τ_o is the time delay between the start of the transmitter and receiver SFCW oscillators, then the new difference frequency $\Delta f'$ is given by

$$\Delta f' = -s(\tau - \tau_o) \quad (\max.(\tau, \tau_o) \leq t \leq t_1) \tag{2.5}$$

A 2-30 MHz bandpass filter preceded the first mixer, in order to suppress interference from radio transmitters in the 0-2 MHz band and galactic noise at frequencies above 30 MHz where the system was not designed to operate. The first mixer mixed a locally generated SFCW signal exactly 40 MHz higher in frequency than the expected received SFCW signal, and the difference signal, centred at an intermediate frequency of 40 MHz, was extracted by filtering. This signal was then successively amplified and mixed down, first to a 2 MHz and then to a 100 kHz intermediate frequency. Finally the signal was passed through a phase-sensitive detector and mixed down to D.C.. Two output signals were thus generated, labelled I (for "in-phase") and Q (for "quadrature") in Fig. 2.3, with I leading Q in phase by 90^{o}. The I and Q signals were low-pass filtered as mentioned in Section 2.2.2 both to improve the output signal-to-noise ratio and to reduce the bandwidth of the signal to that which could be adequately sampled by the digital recording system.

An automatic gain control (AGC) circuit was included in each receiver, to allow the receivers to cope with the large dynamic range of signal amplitudes often encountered in SFCW signals propagated by ionospheric reflection. The instantaneous AGC signal levels could have been recorded for subsequent calculation of the instantaneous receiver gains, but for this experiment the AGC's were disabled and the receivers were calibrated and operated in a linear mode.

The equalization of the gross phase shifts impressed on the received signals by the different receivers was not a design criterion, but care was taken to ensure that the differential phase shift between any pair of receivers as a function of frequency was small. Measure-

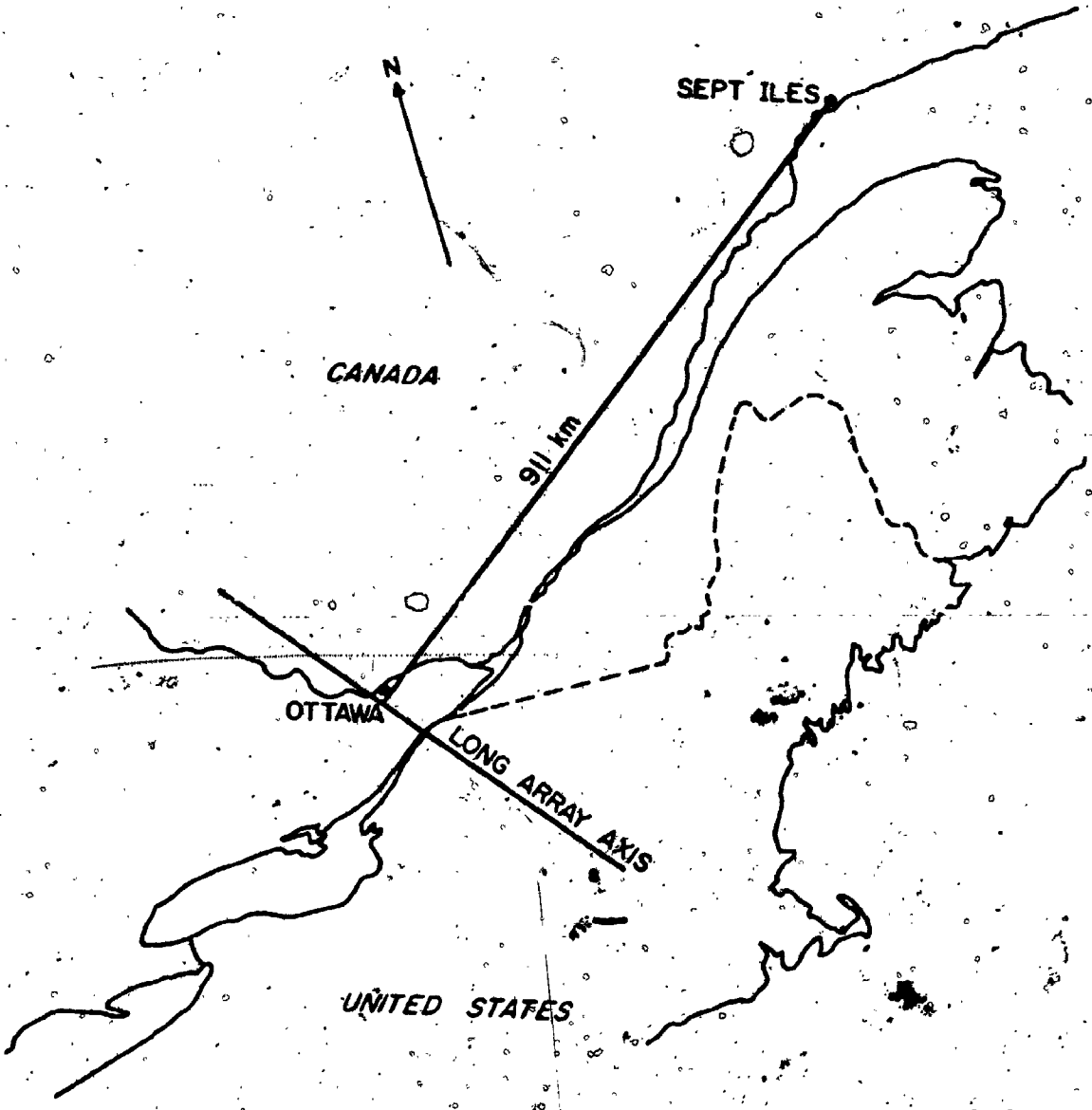

Figure 2.1. The path geography

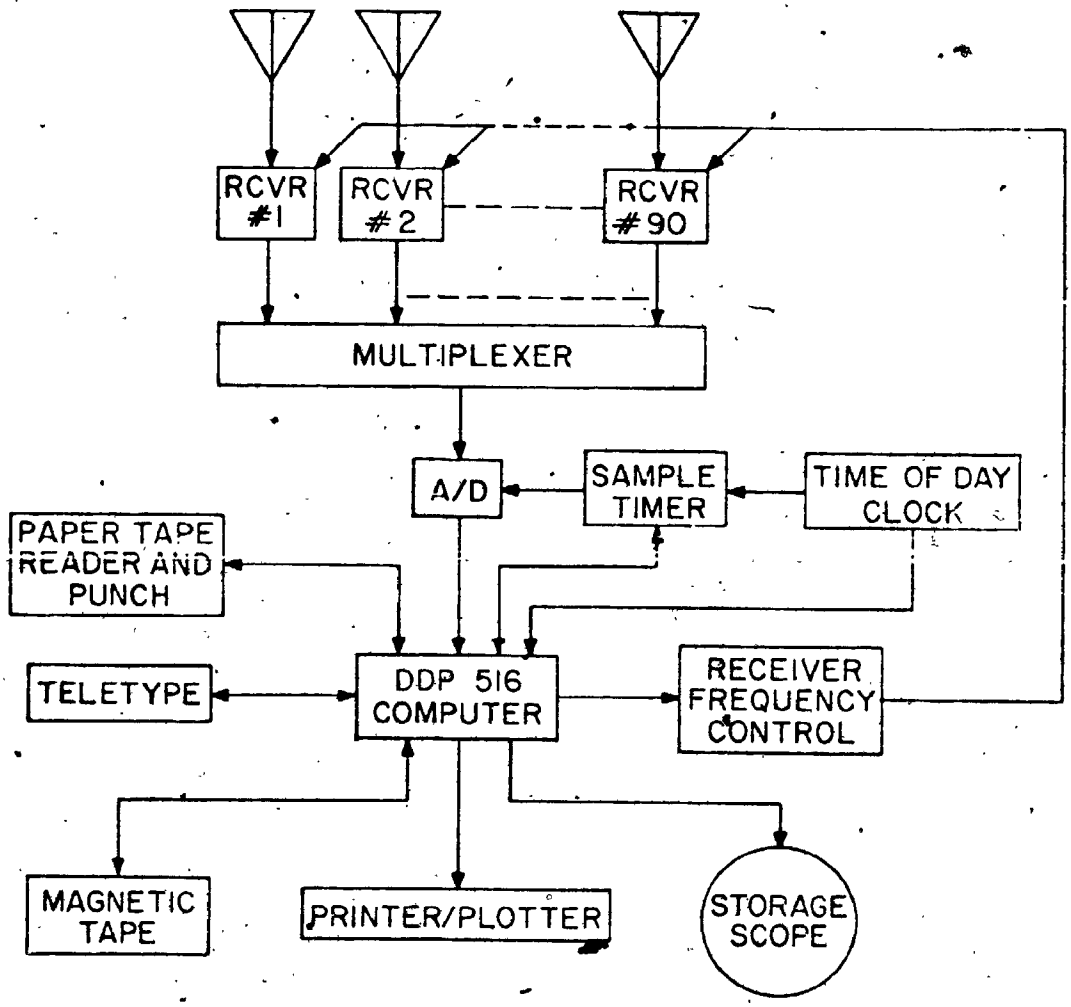

Figure 2.4. Block diagram of the control and recording system

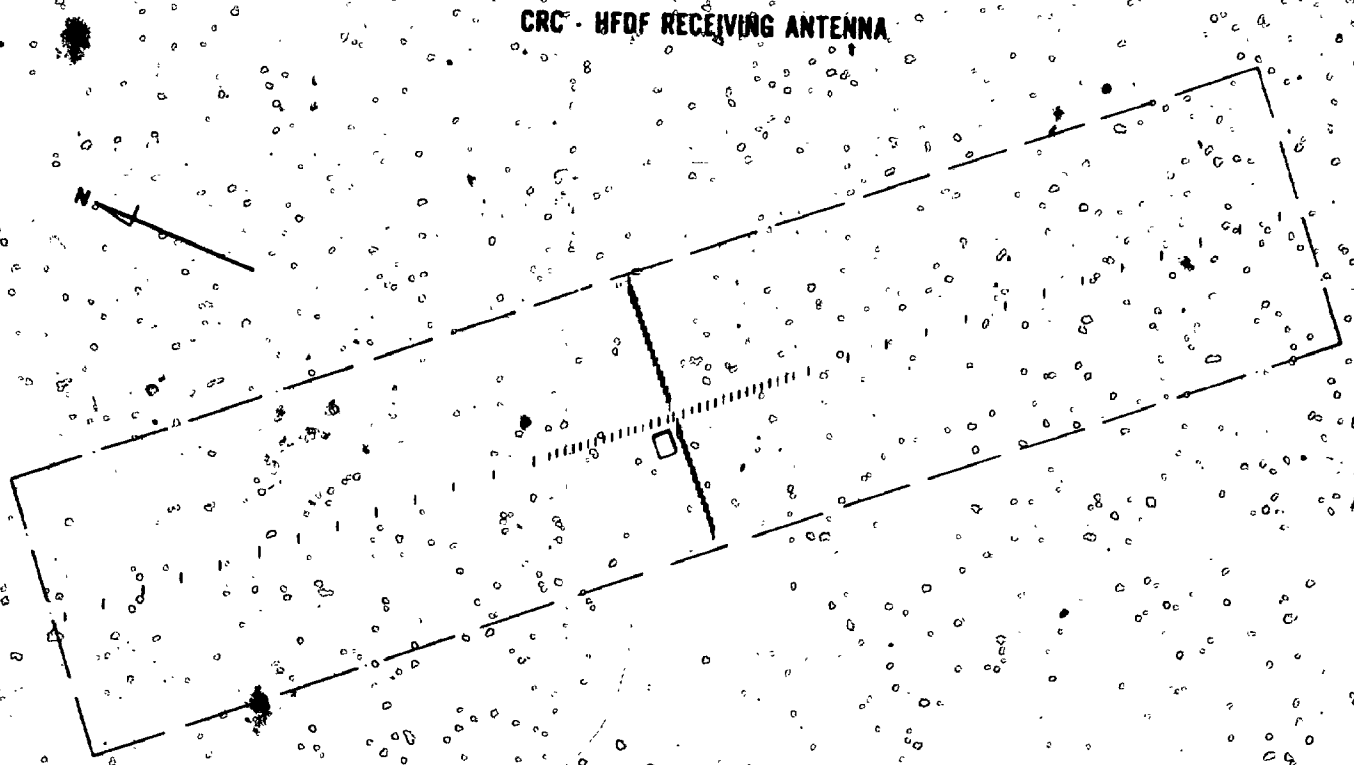

Figure 2.2. The receiving antenna array

elements at a uniform inter-element separation of 125 feet could be laid out.

The cross array was orthogonal to and identical to the inner sub-array of the long array.

For this experiment, only 64 receivers were available. All 58 positions of the long array were monitored, and the remaining six receivers were connected to six elements in the cross array. These elements were placed symmetrically at 125 foot intervals inwards starting from the outermost positions of the cross array.

2.3.3 The Antenna Elements

The antenna elements used for this experiment were a slightly modified version of the elevated feed monopole antenna described by Hatch *et al.* (1966). Unfortunately, to date no comprehensive measurements of either the absolute gain or the radiation pattern of these antennas have been made, but Hatch *et al.* have published theoretically derived elevation angle gain patterns. These indicate that for antennas of 28-foot height, as used here, usable sensitivity over the entire 2-30 MHz frequency band is always maintained for elevation angles less than 20°. Further, galactic or so-called "sky" noise from near the zenith, the usual direction of its greatest intensity since ionospheric absorption attenuates it more strongly for lower elevation angles, is sharply discriminated against by the high angle null in the elevation gain pattern. This effect improves the signal-to-noise ratio. The expected azimuthal gain pattern is, of course, omnidirectional.

An elevated feed position, in addition to ensuring a slowly varying elevation-angle gain pattern as a function of frequency, also produces an antenna with a smoothly varying impedance versus frequency characteristic. For SFCW modulation this is a very important consideration, because resonances in the system could easily corrupt the data.

The antenna elements were coupled to 50 ohm coaxial cables by means of specially designed impedance matching transformers. These transformers were designed to load the antenna in such a manner as to further smooth the impedance versus frequency characteristic as measured at the transformer output terminals. Tests of the transformers showed that their amplitude and phase characteristics were identical to within RMS deviations of order ± 0.5 dB of loss ($\pm 5\%$ in amplitude) and $\pm 3^{\circ}$ of phase over the 2-30 MHz frequency band, so that they were one of the major sources of systematic error in the data.

2.3.4 The Antenna Cables

High-precision 50 ohm coaxial cables (Alucel AL 1250 P, manufactured by Canada Wire and Cable Ltd.) were used to connect the antennas to the receivers. These cables were ½ inch in diameter, with solid copper inner conductor, foamed plastic dielectric, solid aluminum outer conductor, and a vinyl outer sheath. They were buried to a depth of six feet to protect them from physical damage and to provide a thermally stable environment.

The cables can be considered as comprising two sets. One set consisted of cables approximately 488 feet long, connecting the inner sub-array and the cross-array antenna positions to the underground

laboratory. The outer set consisted of cables approximately 2085 feet long, connecting the two outer sub-array antenna positions to the underground laboratory.

The cables in each set have been matched amongst themselves over the 2-30 MHz frequency band, to a tolerance of ± 2 cm of phase length (1° of phase at 30 MHz). This was done by means of a complex SFCW phase matching technique (E.L. Winacott, private communication). An empirical formula (Appendix A, eqn. (A.1)) relating to within $\pm 1^{\circ}$ the absolute phase length difference between the inner and outer sub-array cables as a function of radio frequency and cable temperature has been derived by Mr. Winacott, and this formula was used to eliminate the systematic differences between phase observations made using one or the other sets of cables.

The attenuation characteristics of the cables as a function of frequency were less well known, not having been extensively measured. A few tests have been made, however, which indicated that the manufacturer's specifications gave an estimate of the cable attenuation factor to within about 0.2 dB for the long cables.

Appendix A contains details of the cable amplitude and phase calibration formulae.

2.3.5 The Receivers

The receivers, which were specially designed by D.W. Rice, consisted basically of three mixers and three amplifying stages followed by a phase-sensitive detector. A block diagram of a receiver is presented in Fig. 2.3, and the receiver performance characteristics are summarized in Table 2.1.

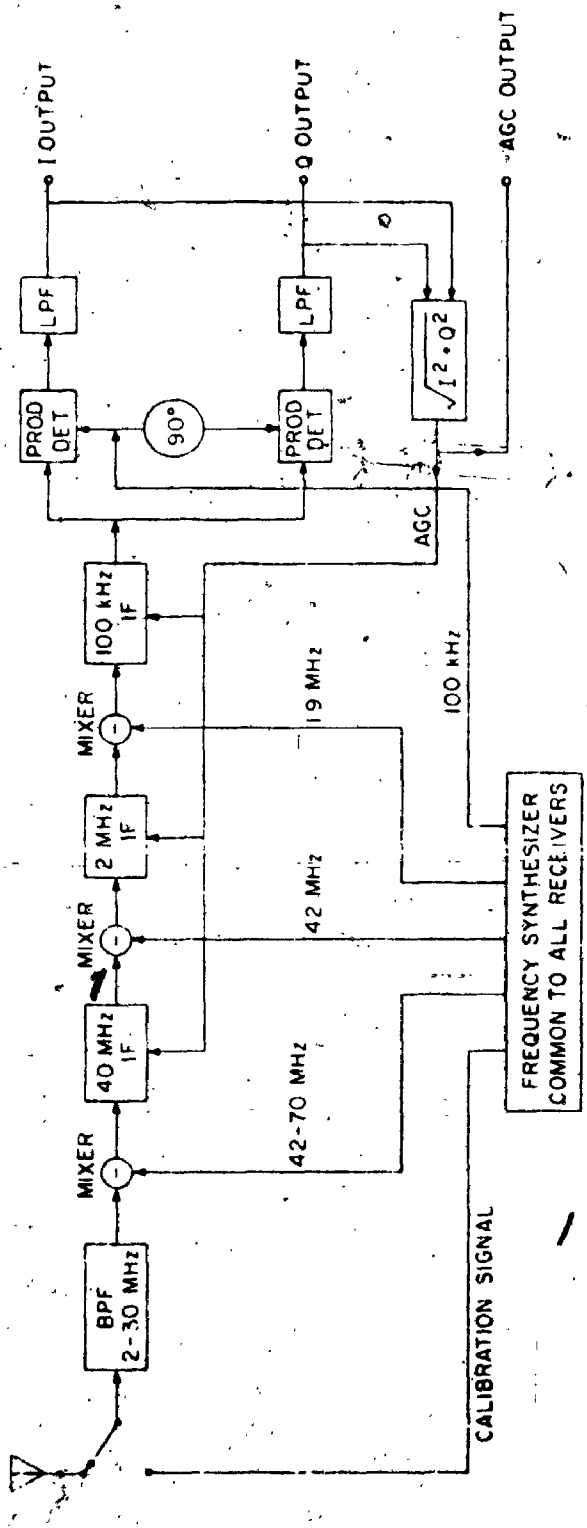

Figure 2.3 Block diagram of a receiver

TABLE 2.1

Summary of Receiver Characteristics

Input impedance	50 ohms
Noise figure	12 dB above kTB (T = 300°K)
Output bandwidth (-3 dB)	±15 Hz
Filter attenuation characteristic	24 dB/octave
Maximum output amplitude	10 V
Amplitude gain factor (for this experiment)	$\sim 3.2 \times 10^6$
Expected RMS noise voltage at each receiver output due to receiver noise (15 Hz BW)	22 mV
Measured standard deviation of corrected receiver gains	3.5% (0.3 dB)
Measured standard deviation of corrected receiver phases	2°

A 2-30 MHz bandpass filter preceded the first mixer, in order to suppress interference from radio transmitters in the 0-2 MHz band and galactic noise at frequencies above 30 MHz where the system was not designed to operate. The first mixer mixed a locally generated SFCW signal exactly 40 MHz higher in frequency than the expected received SFCW signal, and the difference signal, centred at an intermediate frequency of 40 MHz, was extracted by filtering. This signal was then successively amplified and mixed down, first to a 2 MHz and then to a 100 kHz intermediate frequency. Finally the signal was passed through a phase-sensitive detector and mixed down to D.C.. Two output signals were thus generated, labelled I (for "in-phase") and Q (for "quadrature") in Fig. 2.3, with I leading Q in phase by 90^{o}. The I and Q signals were low-pass filtered as mentioned in Section 2.2.2 both to improve the output signal-to-noise ratio and to reduce the bandwidth of the signal to that which could be adequately sampled by the digital recording system.

An automatic gain control (AGC) circuit was included in each receiver, to allow the receivers to cope with the large dynamic range of signal amplitudes often encountered in SFCW signals propagated by ionospheric reflection. The instantaneous AGC signal levels could have been recorded for subsequent calculation of the instantaneous receiver gains, but for this experiment the AGC's were disabled and the receivers were calibrated and operated in a linear mode.

The equalization of the gross phase shifts impressed on the received signals by the different receivers was not a design criterion, but care was taken to ensure that the differential phase shift between any pair of receivers as a function of frequency was small. Measure-

ments of this characteristic for the receivers used in this experiment showed that, over the 20-30 MHz frequency band, the maximum differential phase deviation was about 12°, and it was a smoothly varying function of frequency.

The effect of both the gross and frequency dependent differential phase shifts and differences in the gains of the different receivers, as well as the effects of gain imbalance and departures from phase quadrature in the individual receiver phase sensitive detectors could be compensated for by the procedures outlined in Appendix A.2. The contribution to the uncertainties in the data due to receiver effects were thus reduced to standard deviations of 0.3 dB in gain or 3.5% in amplitude and 2° in phase.

2.3.6 The Computerized Control and Data Recording System

The central position occupied by the computer in the HFDF system is shown in Fig. 2.4. The computer acted in a dual role: it controlled the sampling, quantizing and recording of the data, and it could also be used for processing some calibration data and performing simple real-time data analysis. The latter capabilities were used in the present experiment only to confirm that the system was functioning properly and to record, process and display ionograms, which were used to check the synchronization of the transmitter and receiver clocks.

A brief description of the data recording process follows. When the time of day clock reached the time selected for the start of a SFCW signal transmission, a time delay τ_o (Section 2.2.2) was allowed to elapse; then a sweep of the local SFCW oscillator (denoted as the "receiver frequency controller" in Fig. 2.4) was initiated and the

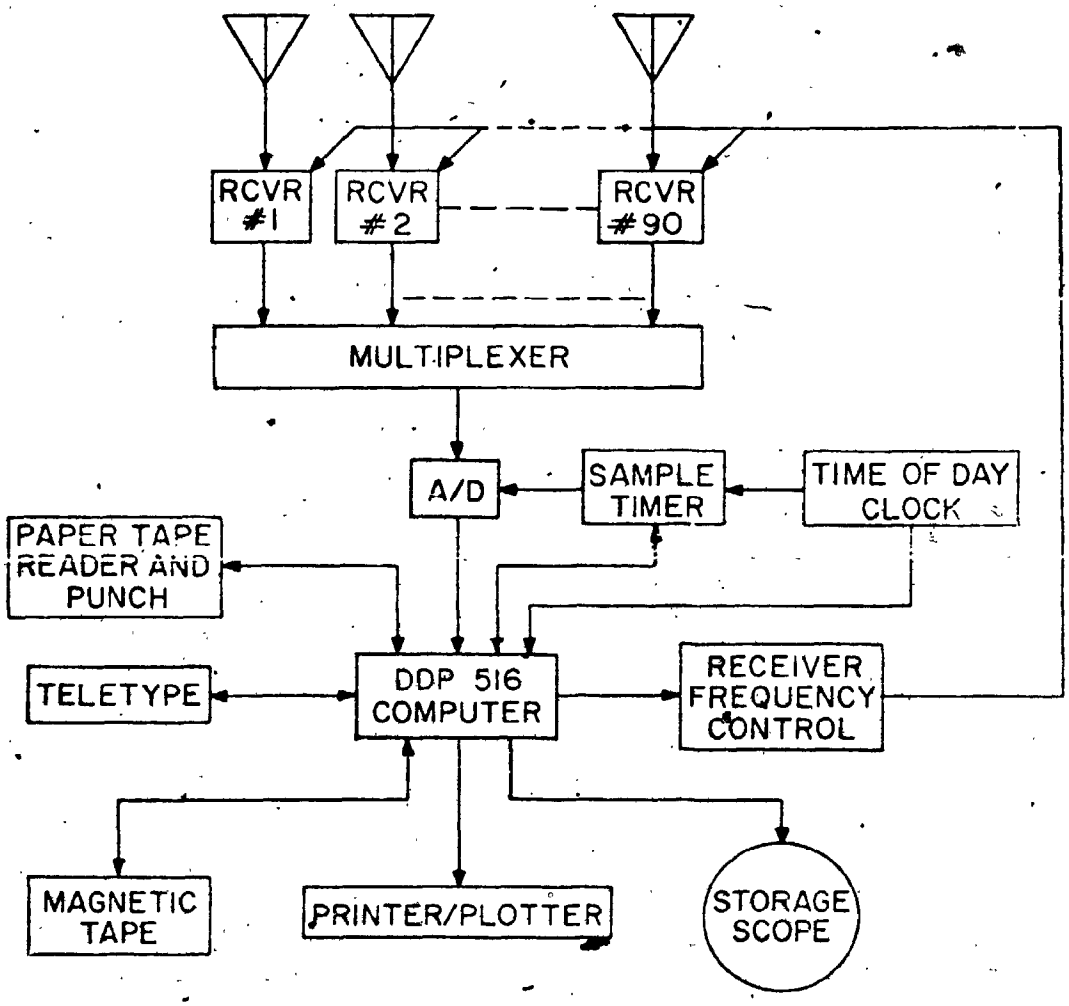

Figure 2.4. Block diagram of the control and recording system

sample timer was turned on. The sample timer was a pulse generator which was monitored by the computer, which in turn controlled the multiplexer and analog-to-digital converter (denoted as "A/D" in Fig. 2.4). Each time a control pulse was emitted by the sample timer, the 128 outputs of the 64 receivers were sequentially scanned by the multiplexer and each output signal voltage in turn was quantized into one of 4096 discrete levels by the analog-to-digital converter, at a converter-limited rate of 43,000 conversions per second. Each quantized datum was immediately transferred to the memory of the computer via a direct memory access channel, and when sufficient data had been accumulated there, the computer transferred them to the digital magnetic tape recorder via another direct memory access channel, at a recorder-limited maximum average rate of 24,000 data per second.

The choice of sequential rather than simultaneous sampling of the receiver outputs was based on the relative costs of the two techniques. The bias introduced into the data by sequential sampling was compensated for as described in Appendix A.3.

2.4 Summary of Systematic Error Effects

Tables 2.2 and 2.3 summarize the contributions to the overall standard deviations to be expected in amplitude and phase measurements due to systematic distortion effects. Receiver thermal noise has been ignored. The combined effect of systematic gain and phase errors was to yield a signal-to-distortion ratio of 22 dB at the outputs of each receiver.

TABLE 2.2

Summary of Systematic Gain Errors

Antenna transformer gain variations	5%
Error in attenuation variation between long and short antenna cables (after corrections)	2%
Receiver-to-receiver gain variation (after correction)	3.5%
Combined (RMS) systematic gain errors	6.4%

TABLE 2.3

Summary of Systematic Phase Errors

Standard deviation of antenna transformer phase errors	3°
Standard deviation of antenna cable phase errors	1°
Standard deviation of receiver-to-receiver phase variation (after correction)	2°
Combined (RMS) standard deviation of systematic phase errors	4°

CHAPTER 3

THEORY

3.0 Introduction

The theoretical study of forward scattering of radio waves by meteor trails is certainly not new, the topic having been thoroughly treated for the underdense, undistorted trail case by Eshelman (1952) over two decades ago. Additional references to this subject as well as a development of the theory itself are given by McKinley (1961). It is necessary to re-derive the theory here, however, in order to define the scattering geometry in terms of parameters observable by the present experimental apparatus.

The content of this chapter can be summarized as follows. A spherical incident wave radiated by a point-source transmitter will be assumed to be scattered by a meteor trail with arbitrary reflection-coefficient profile. The trail axis will first be approximated by a straight line, and later in the development, distortions from the initial straight-line axis model will be incorporated. An expression for calculating possible phase paths from the transmitter via the meteor trail to any point near an arbitrary local origin will be derived, and this expression in conjunction with the reflection coefficient profile can be integrated along the length of the trail to yield the desired spatial diffraction pattern. The properties of the theoretical diffraction pattern will then be investigated in order to determine how experimentally observed patterns might vary as a function of trail distortions and reflection coefficient fluctuations. Finally, for completeness, the basic theory describing the reflection coefficients

of meteor trails as a function of time and line density will be reviewed.

3.1 Definition of the Coordinate System

Figure 3.1 shows the coordinate system chosen for this analysis. The transmitter is located at the point T, and the centre of the receiving array is located at the point R, a distance $2z_o$ away. The point 0 is located at the mid-point of the chord TR, and is the origin of the central (ξ,η,ζ) Cartesian coordinate system. Except for the backscatter case, the point 0 is located beneath the surface of the earth. The point R is the origin of the (x,y,z) coordinate system to which the locations of the receiving antenna elements are referenced. Points along the meteor trail are refereneed to a third coordinate system, (ξ', η', ζ'), located with its origin at the point (ξ_o, η_o, ζ_o). A set of unit vectors $(\hat{i}, \hat{j}, \hat{k})$ is defined with its members parallel to the respective axes of both the (ξ,η,ζ) and (x,y,z) coordinate systems.

The following useful vectors are defined in Fig. 3.1:

$$\underline{\rho_o} = \xi_o\hat{i} + \eta_o\hat{j} + \zeta_o\hat{k} \qquad (3.1a)$$

$$\underline{\rho'} = \xi'\hat{i} + \eta'\hat{j} + \zeta'\hat{k} \qquad (3.1b)$$

$$\underline{r} = x\hat{i} + y\hat{j} + z\hat{k} \qquad (3.1c)$$

$$\underline{R_{10}} = \underline{\rho_o} + z_o\hat{k} \qquad (3.1d)$$

$$\underline{R_{20}} = -\underline{\rho_o} + z_o\hat{k} \qquad (3.1e)$$

$$\underline{R_1} = \underline{R_{10}} + \underline{\rho'} \qquad (3.1f)$$

$$\underline{R_2} = \underline{R_{20}} - \underline{\rho'} + \underline{r} \qquad (3.1g)$$

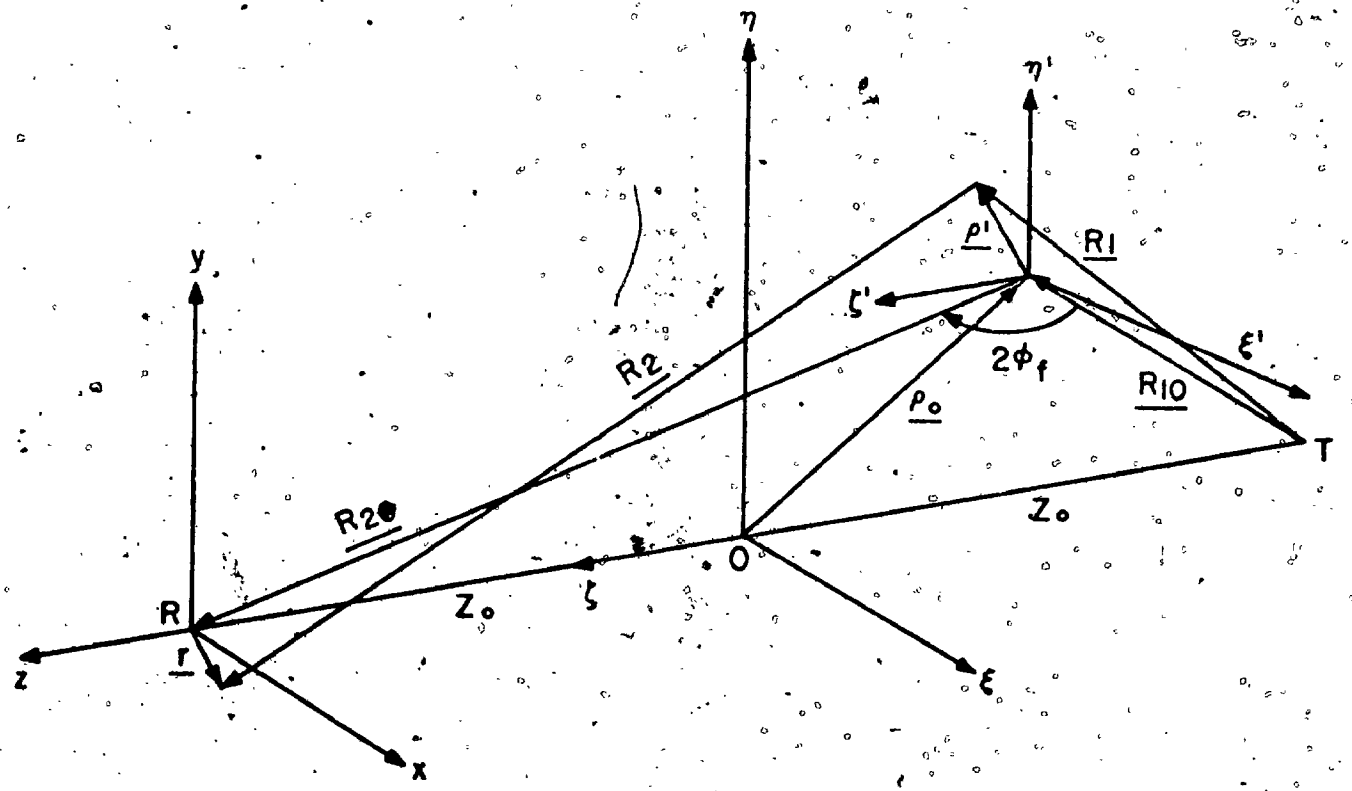

Figure 3.1. The coordinate system

The vectors $\underline{R}_{10}$, $\underline{R}_1$, $\underline{R}_{20}$ and $\underline{R}_2$ are directed approximately parallel to the direction of propagation of the radio waves.

3.2 The General Phase Expression

By expanding expressions for R_1 and R_2 in Taylor series about their respective central values R_{10} and R_{20} it can be shown that, to second order in ρ' and r:

$$R_1 + R_2 = R_{10} + R_{20} + 2(\underline{R}_{10}/R_{10} - \underline{R}_{20}/R_{20}) \cdot \underline{\rho}' + 2(\underline{R}_{20} \cdot \underline{r})/R_{20}$$
$$+ \frac{1}{R_{10}} \left\{ \rho'^2 - \left[(\underline{R}_{10} \cdot \underline{\rho}')/R_{10} \right]^2 \right\} \qquad (3.2)$$
$$+ \frac{1}{R_{20}} \left\{ |\underline{\rho}' - \underline{r}|^2 - \left[\underline{R}_{20} \cdot (\underline{\rho}' - \underline{r})/R_{20} \right]^2 \right\}$$

Letting the radio wavelength be denoted by λ and the magnitude of the propagation vector by $k = 2\pi/\lambda$ allows the phase path distance (in radians) $\Phi(\underline{\rho}', \underline{r}) = k(R_1 + R_2)$ to be written as

$$\Phi(\underline{\rho}', \underline{r}) = (\underline{k}_{10} - \underline{k}_{20}) \cdot \underline{\rho}' + \underline{k}_{20} \cdot \underline{r}$$
$$+ \frac{\pi}{2} \frac{1}{F_{10}^2} \left\{ \rho'^2 - \left[\underline{R}_{10} \cdot \underline{\rho}'/R_{10} \right]^2 \right\} \qquad (3.3)$$
$$+ \frac{\pi}{2} \frac{1}{F_{20}^2} \left\{ |\underline{\rho}' - \underline{r}|^2 - \left[\underline{R}_{20} \cdot (\underline{\rho}' - \underline{r})/R_{20} \right]^2 \right\}$$
$$+ \Phi_o$$

where

$$\underline{k_{10}} = k(\underline{R_{10}}/R_{10}) \qquad (3.4a)$$

$$\underline{k_{20}} = k(\underline{R_{20}}/R_{20}) \qquad (3.4b)$$

$$F_{10}^2 = R_{10}\,\lambda/2 \qquad (3.4c)$$

$$F_{20}^2 = R_{20}\,\lambda/2 \qquad (3.4d)$$

and

$$\Phi_o = k(R_{10} + R_{20}) \qquad (3.4e)$$

Φ_o is a constant which subsequently will be ignored.

3.3 The Straight-line Trail Model

For the straight-line trail model, the vector $\underline{\rho'}$ can be expressed in the form

$$\underline{\rho'} = \ell(\alpha\hat{i} + \beta\hat{j} + \gamma\hat{k}) \qquad (3.5)$$

where α, β and γ are direction cosines which can be calculated for a particular propagation geometry if the celestial coordinates of the meteor radiant are known, and ℓ is a measure of length along the trail axis from the point (ξ_o, η_o, ζ_o). A unit vector

$$\hat{\ell} = \alpha\hat{i} + \beta\hat{j} + \gamma\hat{k} \quad , \qquad (3.6)$$

pointing in the direction of meteor travel, can be defined so that $\Phi(\underline{\rho'},\underline{r}) = \Phi_s(\ell,\underline{r})$ and in particular

$$\Phi_S(\ell,0) = (\underline{k}_{10} - \underline{k}_{20}) \cdot \hat{\ell}\,\ell + \frac{\ell^2}{F_{10}^2}\left\{1 - \left[\underline{R}_{10} \cdot \hat{\ell}/R_{10}\right]^2\right\} + \frac{\ell^2}{F_{20}^2}\left\{1 - \left[\underline{R}_{20} \cdot \hat{\ell}/R_{20}\right]^2\right\} \tag{3.7}$$

The subscript S denotes a straight-line trail model.

The condition that the point (ξ_o, η_o, ζ_o) be the point of stationary phase or geometric specular reflection point is imposed by requiring the condition

$$\left(\frac{\partial\Phi}{\partial\ell}\right)_{\substack{\ell=0 \\ r=0}} = (\underline{k}_{10} - \underline{k}_{20}) \cdot \hat{\ell} = 0 \tag{3.8}$$

be satisfied. This leads to the usual law of reflection: angle of incidence equals angle of reflection.

It is now helpful to consider the prolate spheroid with foci at T and R and passing through the point (ξ_o, η_o, ζ_o), which can be defined by the equation

$$\xi^2 + \eta^2 + \zeta^2\left[1 - (Z_0/R_0)^2\right] = R_0^2\left[1 - (Z_0/R_0)^2\right] \tag{3.9}$$

where

$$R_0 = \frac{1}{2}(R_{10} + R_{20}) \tag{3.10}$$

A vector $\underline{N}(\xi,\eta,\zeta)$ outwardly normal to the surface of this spheroid is found by taking the gradient of the above expression:

$$\underline{N}(\xi,\eta,\zeta) = \xi\hat{i} + \eta\hat{j} + \zeta[1 - (Z_0/R_0)^2]\hat{k} \tag{3.11}$$

and in particular at the point (ξ_o,η_o,ζ_o)

$$\underline{N_0}(\xi_o,\eta_o,\zeta_o) = \underline{\rho_o} - \zeta_o(Z_0/R_0)^2\hat{k} \tag{3.12}$$

It can be shown that

$$\underline{k_{10}} + \underline{k_{20}} = (k/R_{00})[\underline{\rho_o} - \zeta_o(Z_0/R_0)^2\hat{k}] \tag{3.13}$$

where

$$(1/R_{00}) = (1/R_{10}) + (1/R_{20}). \tag{3.14}$$

Consequently, from eqns. (3.8), (3.13) and (3.12)

$$\underline{N_0} \cdot \underline{\ell} = 0 \tag{3.15}$$

so that the meteor trail is tangent to the prolate spheroid at the specular reflection point.

Because of the validity of eqn. (3.15) it can be shown that

$$\cos(\underline{k_{10}},\hat{\ell}) = \gamma\, Z_0/R_0 = \cos(\underline{k_{20}},\hat{\ell}) \tag{3.16}$$

where for example $\cos(\underline{k_{10}},\hat{\ell})$ is the cosine of the angle between the vectors $\underline{k_{10}}$ and $\hat{\ell}$.

Further algebraic manipulation yields a final expression for the phase path length from T to $\underline{r}$ via an arbitrary point on the straight line trail:

$$\Phi_S(\ell,\underline{r}) = \underline{k_{20}}\cdot\underline{r} + \frac{\pi}{2}\frac{\ell^2 - 2\ell\,\ell_{oo}(\underline{r})}{F_o^2} + \frac{\pi}{2}\frac{\sin^2(\underline{k_{20}},\underline{r})}{F_{20}^2}\,r^2 \quad (3.17)$$

where

$$\ell_{oo}(\underline{r}) = rM(\underline{r})\left[\frac{R_{10}}{2R_o}\right]\Big/\sin^2(\underline{k_o},\hat{\ell}) \quad (3.18)$$

is the point of stationary phase on the trail for an observation made at the point $\underline{r}$, and

$$M(\underline{r}) = \cos(\hat{\ell},\underline{r}) - \cos(\underline{k_o},\hat{\ell})\cos(\underline{k_{20}},\underline{r}) \quad (3.19)$$

is an angularly-dependent projection factor; also

$$\cos(\underline{k_o},\hat{\ell}) = \gamma\, Z_0/R_0, \quad (3.20)$$

$$F_o^2 = \frac{R_{00}\,\lambda}{2\sin^2(\underline{k_o},\hat{\ell})} \quad (3.21)$$

$$R_{10}/R_0 = 1 + \zeta_o Z_0/R_0^2\,. \quad (3.22)$$

In passing, it is noted that the characteristic length F_o is $1/\sqrt{2}$ times the usual definition of the radius of the principal Fresnel zone as defined in the classical Fresnel diffraction theory of forward scattering from meteor trails (McKinley, 1961).

3.4 The Distorted-Trail Model

To account for distortions from an initial straight-line trail model, the vector $\underline{\rho'}$ can be written as the sum of two terms:

$$\underline{\rho}'(\ell,t) = \underline{\ell} + \underline{\rho}''(\ell,t) \tag{3.23}$$

where $\underline{\rho}''(\ell,t)$ is the vector displacement at the time t of an elemental segment of length $d\ell$ and initial position $\underline{\ell}$ at time t=0. Such distortions could be caused by neutral winds. It is assumed that $\underline{\rho}''(\ell,0) = 0$.

By substituting eqn. (3.23) into eqn. (3.3) and expanding it can be shown that, to second order in ρ'' and ℓ, the phase path via a distorted trail, $\Phi_D(\ell,\underline{r},t)$, is given by

$$\begin{aligned}\Phi_D(\ell,\underline{r},t) = \phi_S(\ell,\underline{r}) &+ 2k(\underline{\rho}''\cdot\hat{n}_o)\cos\phi_f + \frac{\pi}{2}\Big\{2(\underline{\rho}''\cdot\underline{\ell}) \\ &+ 2\ell\cos(\underline{k}_o\cdot\hat{\ell})[(\underline{\rho}''\cdot\hat{n}_o)(\zeta_o Z_0/R_0^2)\cos\phi_f - (\underline{\rho}''\cdot\hat{p}_o)\sin\phi_f] \\ &+ (\underline{\rho}''\cdot\hat{m}_o)^2 + (\underline{\rho}''\cdot\hat{n}_o)^2\sin^2\phi_f \\ &+ (\underline{\rho}''\cdot\hat{p}_o)^2\cos^2\phi_f\Big\}/\Big\{F_o^2\sin^2(\underline{k}_o,\hat{\ell})\Big\}\end{aligned} \tag{3.24}$$

where $\hat{m}_o$, $\hat{n}_o$, $\hat{p}_o$ comprise a right-hand set of unit vectors as defined below, and

$$\cos\phi_f = \left[\frac{1 - (Z_0/R_0)^2}{1 - (\zeta_o Z_0/R_0^2)^2}\right]^{\frac{1}{2}} \tag{3.25}$$

where $2\phi_f$ is the usual forward scatter angle (McKinley, 1961), measured in the plane of propagation. In terms of the present definitions, $2\phi_f$ is the angle between the vectors $-\underline{R}_{10}$ and $\underline{R}_{20}$.

The "transverse" unit vector $\hat{m}_o$ is defined by the expression

$$\hat{m}_o = [1 - (\zeta_o/R_0)^2]^{-\frac{1}{2}}\,[1 - (Z_0/R_0)^2]^{-\frac{1}{2}}\,\{\eta_o\hat{i} - \xi_o\hat{j}\}/R_0 \tag{3.26}$$

and is normal to the plane of propagation. The "normal" unit vector is defined by

$$\hat{n}_o = [1 - (\zeta_o Z_0/R_0^2)^2]^{-\frac{1}{2}} [1 - (Z_0/R_0)^2]^{-\frac{1}{2}} \{\underline{\rho}_o - \zeta_o (Z_0/R_0)^2 \hat{k}\}/R_0 \tag{3.27}$$

and is parallel to $\underline{N}_0$. The "parallel" unit vector $\hat{p}_o$ is defined by

$$\hat{p}_o = [1 - (\zeta_o/R_0)^2]^{-\frac{1}{2}} [1 - (\zeta_o Z_0/R_0^2)^2]^{-\frac{1}{2}} \{\hat{k} - (\zeta_o/R_0)\, \underline{\rho}_o/R_0\} \tag{3.28}$$

and is directed roughly parallel to the direction of signal propagation. The vectors $\hat{n}_o$ and $\hat{p}_o$ lie in the plane of propagation.

For the present experiment it is reasonable to neglect in eqn. (3.24) the terms containing products of ρ'' and ℓ, which correspond to axial displacement of the trail, as well as the second order terms in ρ'' and r, to yield a simplified expression for $\Phi_D(\ell,\underline{r},t)$:

$$\Phi_D(\ell,\underline{r},t) = \underline{k}_{20}\cdot\underline{r} + \frac{\pi}{2} \frac{\{\ell^2 - 2\ell\, \ell_{oo}(\underline{r})\}}{F_o^2} + 2k(\underline{\rho}''\cdot\hat{n}_o) \cos\phi_f \tag{3.29}$$

The critical points of $\Phi_D(\ell,\underline{r},t)$ can be found by evaluating

$$\left(\frac{\partial \Phi_D}{\partial \ell}\right)_{\underline{r},t} = 0 \tag{3.30}$$

which leads to the result

$$\ell_s(\underline{r},t) = \ell_{oo}(\underline{r}) - \left\{2R_{oo}/\sin^2(\underline{k}_o,\hat{\ell})\right\} \cos\phi_f \left[\frac{\partial \underline{\rho}''}{\partial \ell}\right]_{\ell=\ell_s} \cdot \hat{n}_o \tag{3.31}$$

The solutions $\ell_s(\underline{r},t)$ of eqn. (3.31) are points of stationary phase on the distorted trail. It is expected that most of the contributions to the received signal amplitude will arise from the vicinity of these stationary-phase points.

3.5 The Received Echo Signal

The contribution to the complex amplitude of the electric field observed at the point $\underline{r}$ due to the signal reflected by the element of meteor trail of length $d\ell$ at the point $\underline{\ell} + \underline{\rho}''(\ell,t)$ is approximately

$$dE(\ell,\underline{r},k) = \frac{V_0}{R_{10}R_{20}}\, g(\ell,t)\, \exp\left[j\Phi_D(\ell,\underline{r})\right] d\ell \quad . \qquad (3.32)$$

where $g(\ell,t)$ is the reflection coefficient of the trail, and is a function both of time and of position along the trail axis, and

$$V_0 = (P_0 G\, Z_0)^{\frac{1}{2}}/4\pi \qquad (3.33)$$

where P_0 is the transmitter power, G is the transmitter antenna gain in the direction of propagation towards the trail, relative to an isotropic radiator, and Z_0 is the impedance of free space (~377 ohms). The total amplitude of the scattered field at the point $\underline{r}$ at time t is found by integrating eqn. (3.33) over the entire length of the trail:

$$E(\underline{r},t) = \frac{V_0}{R_{10}R_{20}} \int_{\text{trail}} g(\ell,t)\, \exp\left[j\Phi_D(\ell,\underline{r},t)\right] d\ell \qquad (3.34)$$

It can be seen that eqn. (3.34) is a Fresnel-diffraction integral.

3.5.1 The Echo Received from a Distorted Trail with a Uniform Reflection-Coefficient Profile

If in the vicinity of a stationary phase point $\ell_s(\underline{r},t)$ the reflection coefficient can be regarded as essentially constant with an effective value $g_o[\ell_s(0),t]$, then eqn. (3.34) can be formally integrated using the principle of stationary phase to yield the result for the distorted trail case (denoted by the subscript d):

$$E_D(\underline{r},t) = \exp\{j\underline{k}_{20}\cdot\underline{r}\} \times \sum_s E_{D,s}(\underline{r},t)\cdot\exp\{-jk(\ell_s/R_{20})\underline{M}(\underline{r})r\} \quad (3.35)$$

where

$$E_{D,s}(\underline{r},t) = \frac{V_0}{R_{10}R_{20}} L_s g(\ell_s,t) \exp\left\{j\left[\frac{\pi}{2}\left(\frac{\ell_s}{F_o}\right)^2 + 2k(\underline{\rho}''(\ell_s)\cdot\hat{n}_o)\cos\phi_f\right]\right\} \quad (3.36)$$

is almost independent of $\underline{r}$. The summation over s indicates a summation of an unknown number of stationary phase points. For each allowed value for s, L_s is a complex quantity with the dimension of length, such that $|L_s|$ represents the effective length of trail in the vicinity of $\ell_s(0)$ which contributes to the signal received at $\underline{r}$; the amplitude of this signal component is proportional to $|L_s g_o|$. It is assumed that $g_o(\ell_s,t)$ is uniform over a length of trail much greater than $|L_s|$. As well, eqn. (3.35) shows that each component of the received signal will have a linear spatial-phase gradient which is directly related to the location of the point on the trail from which the signal is scattered.

For the special case of the undistorted trail, with $\underline{\rho}''(\ell,t) \equiv 0$, then $L_s = L_o$ where

$$L_o = \sqrt{2}\, F_o\, e^{j\pi/4} \quad (3.37)$$

In general, a particular model for $\underline{\rho}''(\ell,t)$ must be chosen before numerical values of L_s can be estimated.

3.5.2 The Echo Received from a Trail with an Irregular Reflection-Coefficient Profile

There is both visual (Jacchia, 1955) and radio (Rice, 1964; Rice and Forsyth, 1964) evidence that the deposition of electrons by an ablating meteoroid may be quite irregular. A simple model for the reflection-coefficient profile of a non-uniform trail, which has as its principal merit its amenability to analysis although it also illustrates the underlying physical principles, can be based on the consideration of the reflection-coefficient profile as a series of an unknown number of segments of enhanced reflectivity. These segments may or may not overlap. The axial profile of the reflection coefficient for each of these segments is assumed to be Gaussian, with random peak reflectivity and random position along the axis of the trail. As well, the trail may have a basic uniform reflection-coefficient profile $g_o(\ell,t)$, so that the net profile $g(\ell,t)$ can be described by the equation

$$g(\ell,t) = g_o(\ell,t) + g_f(\ell,t) \qquad (3.38)$$

where $g_f(\ell,t)$ is the fluctuating component of $g(\ell,t)$:

$$g_f(\ell,t) = \sum_i g_i(t) \exp\left[-\left\{\frac{\ell - \ell_i}{L_i}\right\}^2\right] \qquad (3.39)$$

The summation over i indicates a summation over the unknown number of irregularities, and for each allowed value of i, $g_i(t)$ is the time-

dependent random peak reflection coefficient for an irregularity of scale-size L_i, centred on the random axial location ℓ_i.

For the special case of the undistorted trail, $g_f(\ell,t)$ from eqn. (3.39) can be substituted directly into eqn. (3.34); the integral can then be evaluated immediately to yield

$$E_f(\underline{r},t) = \exp\left\{jk_{20}\underline{\cdot r}\right\} \sum_i E_{f,i}(\underline{r},t) \qquad (3.40)$$

where

$$E_{f,i}(\underline{r},t) = \frac{V_0\sqrt{\pi}}{R_{10}R_{20}} g_i(t) \left(\frac{1}{L_i^2} - j\frac{\pi}{2F_o^2}\right)^{-\frac{1}{2}} \times \exp\left\{\frac{-[\ell_i^2 - 2\ell_i\,\ell_{oo}(\underline{r})]}{L_i^2 + j\,2F_o^2/\pi}\right\} \qquad (3.41)$$

is the received field scattered by the i^{th} irregularity. As usual, terms of second order in ℓ_{oo} (and hence in r) have been neglected in eqn. (3.41).

Some manipulation of eqn. (3.41) shows that for the case of "large-scale" irregularities, i.e.,

$$L_i^2 >> 2F_o^2/\pi \qquad (3.42)$$

then

$$E_{f,i}(\underline{r},t) = \frac{V_0L_0}{R_{10}R_{20}} g_i(t) \exp\left\{\frac{-[\ell_i^2 - 2\ell_i\,\ell_{oo}(\underline{r})]}{L_i^2}\right\} \qquad (3.43)$$

so that for $\ell_{oo}(\underline{r}) << L_i$, only a small fractional amplitude variation due to the i^{th} irregularity would be observed across the antenna array, regardless of the irregularity location ℓ_i or the magnitude of $g_i(t)$.

For the converse case of "small-scale" irregularities, i.e.,

$$L_i^2 << 2F_o^2/\pi \tag{3.44}$$

then

$$E_{f,i}(\underline{r},t) = \frac{V_0\sqrt{\pi}L_i}{R_{10}R_{20}} g_i(t) \exp\left\{j\frac{\pi}{2}\left(\frac{\ell_i}{F_o}\right)^2\right\} \times \exp\{-jk(\ell_i/R_{20})M(\underline{r})r\} \tag{3.45}$$

(cf. eqn. (3.36)) where here the effective length of the scattering irregularity is $\sqrt{\pi}L_i$ and the amplitude of the scattered signal component is proportional to $|L_i g_i(t)|$. Again a linear spatial phase gradient directly related to the location of the scattering irregularity on the trail axis will be observed in the received echo signal.

For the intermediate-scale irregularities with

$$L_i^2 \approx 2F_o^2/\pi \tag{3.46}$$

it can be shown that

$$E_{f,i}(\underline{r},t) = \frac{V_0F_0}{R_{10}R_{20}} g_i(t) \exp\left\{\frac{-[\ell_i^2 - 2\ell_i \ell_{po}(\underline{r})]}{2L_i^2}\right\}$$

$$\times \exp\left\{j\frac{\pi}{2}\left(\frac{\ell_i}{F_o}\right)^2 - \frac{1}{2}k(\ell_i/R_{20})M(\underline{r})r\right\} \tag{3.47}$$

Equation (3.47) shows that both a spatial-amplitude variation and a spatial-phase gradient will be observed for this case, but the phase gradient will be less than that for the "small-scale" irregularity case with the same geometric location (eqn. (3.45)), and the amplitude variation will also be less than that for the "large-scale"

irregularity case with the same geometry and peak reflection coefficient (eqn. (3.38)).

3.5.3 A Special Case - The Echo Received from a Single Additional Scattering Centre

For the special case of a main-echo signal plus a single additional secondary-signal component, the total electric-field amplitude observed at an antenna site is given by

$$E(\underline{r},t) = \left\{E_o(\underline{r},t) + E_1(\underline{r},t)\ \exp[-jk_1 r]\right\} \exp[j\underline{k}_{20}\cdot\underline{r}] \qquad (3.48)$$

where, from eqn. (3.36),

$$E_o(\underline{r},t) = \frac{V_0 L_0}{R_{10}R_{20}}\, g(0,t)\, \exp\left\{j\,\frac{\pi}{2}\,\frac{\ell_o^2}{F_o^2}\right\} \qquad (3.49)$$

$$k_1 = M(r)\, k\, \ell_1/R_{20} \qquad (3.50)$$

and $E_1(\underline{r},t)$ is the complex electric-field component due to the secondary signal scattered from the vicinity of a point ℓ_1 on the trail axis.

For the case of a distorted trail with a stationary phase point located at $\ell = \ell_1$, from eqns. (3.35) and (3.36):

$$E_1(\underline{r},t) = \frac{V_0 L_{s,1}}{R_{10}R_{20}}\, g(\ell_1,t)\, \exp\left\{j\left[\frac{\pi}{2}\,\frac{\ell_1^2}{F_o^2} + 2k[\rho''(\ell_1)\cdot\hat{n}_o]\cos\phi_f\right]\right\} \qquad (3.51)$$

For the case of an irregular trail with a single small-scale irregularity located at $\ell = \ell_1$, from eqn. (3.45)

$$E_1(\underline{r},t) = \frac{V_0 \sqrt{\pi}\, L_{i,1}}{R_{10}R_{20}}\, g_1(t)\, \exp\left\{j\,\frac{\pi}{2}\,\frac{\ell_1^2}{F_o^2}\right\} \qquad (3.52)$$

For either case, the observable parameter $|E(\underline{r},t)|$ is given by

$$|E(\underline{r},t)| = |E_o(\underline{r},t)| \{1 + |E_1(\underline{r},t)/E_o(\underline{r},t)|^2 + 2|E_1(\underline{r},t)/E_o(\underline{r},t)| \cos[k_1 r + \phi_d(\underline{r},t)]\}^{\frac{1}{2}} \quad (3.53)$$

where

$$\phi_d(\underline{r},t) = 2k[\underline{\rho}''(\ell_1) - \underline{\rho}''(\ell_o)]\cdot\hat{n}_o \cos\phi_f + \frac{\pi}{2}\frac{\ell_1^2 - \ell_o^2}{F_o^2} + \phi_g \quad (3.54)$$

is the difference in phase between the complex electric-field amplitudes E_o and E_1, and incorporates both the geometrically induced phase shift between E_o and E_1 and any phase shift ϕ_g caused by differences in the reflection coefficients associated with the two different portions of the trail.

In view of the comments preceding eqns. (3.36) and (3.45), it seems reasonable to neglect the weak dependence of E_o, E_1 and ϕ_d on r. Then

$$\frac{1}{|E_o|}\frac{\partial|E|}{\partial r} = \frac{-|E_1/E_o|\, k_1 \sin(k_1 r + \phi_d)}{\{1 + |E_1/E_o|^2 + 2|E_1/E_o| \cos(k_1 r + \phi_d)\}^{\frac{1}{2}}} \quad (3.55)$$

Under the further assumption that

$$E_1/E_o < 0.3 \quad (3.56)$$

then to within about 5%

$$|E(\underline{r},t)| = |E_o(\underline{r},t)| + |E_1(\underline{r},t)| \cos[k_1 r + \phi_d(\underline{r},t)] \quad (3.57)$$

and

$$\frac{1}{|E_o|}\frac{\partial|E|}{\partial r} = \frac{-|E_1/E_o|k_1 \sin(k_1 r + \phi_d)}{1 + |E_1/E_o| \cos(k_1 r + \phi_d)} \tag{3.58}$$

The phase $\phi(\underline{r},t)$ (in radians) of $E(\underline{r},t)$ is given to within an unknown additive constant by

$$\phi(\underline{r},t) = \arctan\left\{-|E_1/E_o| \sin(k_1 r + \phi_d) / [1 + |E_1/E_o| \cos(k_1 r + \phi_d)]\right\} \tag{3.59}$$

If the inequality (3.56) is satisfied, then $\phi(\underline{r},t)$ is given to within 3% by

$$\phi(\underline{r},t) = \frac{-|E_1/E_o| \sin(k_1 r + \phi_d)}{1 + |E_1/E_o| \cos(k_1 r + \phi_d)} \tag{3.60}$$

Differentiation of eqn. (3.60) yields an estimate of $\partial\phi/\partial r$ accurate to within about 10%:

$$\frac{\partial\phi}{\partial r} = \frac{-|E_1/E_o|k_1 \cos(k_1 r + \phi_d)}{1 + |E_1/E_o| \cos(k_1 r + \phi_d)} \tag{3.61}$$

The preceding discussion has shown that, for the case of a single secondary signal of small amplitude, quasi-sinusoidal fluctuations in the echo amplitude and phase will be observed across the antenna array. Moreover, the amplitude and phase fluctuations, as well as their first derivatives, will be in phase quadrature.

For the particular case

$$|k_1| \cdot \Delta r < \pi \tag{3.62}$$

where Δr is the effective length of the antenna array, the angular separation between the main and secondary echo signals will be less than half the classical beamwidth ($\lambda/\Delta r$) of the antenna array, and the scale-size of the fluctuations will be greater than the length of the array. For this case the quadrature relationship between the spatial derivatives of the echo amplitude and phase is still true, and equations describing the approximately constant spatial slopes are

$$\frac{1}{|E_o|}\frac{\partial|E|}{\partial r} \approx \frac{-|E_1/E_o|\ k_1 \sin\phi_d(0,t)}{1 + |E_1/E_o| \cos\phi_d(0,t)} \tag{3.63}$$

and

$$\frac{\partial\phi}{\partial r} \approx \frac{-|E_1/E_o|\ k_1 \cos\phi_d(0,t)}{1 + |E_1/E_o| \cos\phi_d(0,t)} \tag{3.64}$$

Temporal variations in the spatial amplitude and phase slopes are apparently due primarily to temporal variations in ϕ_d. It can be shown that, for the case of the distorted-trail model, the effect of spatial displacements in the normal ($\hat{n}_o$) direction have an effect at least an order of magnitude greater than an equal displacement in the tangential plane (Section 3.4), so that to good approximation

$$\frac{\partial\phi_d}{\partial t} = 2k\frac{\partial}{\partial t}[\underline{\rho}''(\ell_1) - \underline{\rho}''(\ell_o)]\cdot\hat{n}_o \cos\phi_f \,. \tag{3.65}$$

In terms of this model, $\partial\phi_d/\partial t$ is related to the spatial gradient along the trail axis of the wind component in the direction of $\hat{n}_o$. Of course, the very existence of closely-spaced stationary phase points (or reflection points) would imply the existence of small-scale components of wind-shear structure as well.

For the case of an irregular trail and a complete absence of distorting winds, the only way for ϕ_d to vary with time is if the phase of the reflection coefficient varies differentially with time along the axis of the trail. This effect could occur if the reflection characteristics of the irregularities were to vary significantly with time as the trail diffuses.

3.5.4 The Spatial Fourier Transform of the Complex Amplitude of the Received Signal

In the present experiment it was possible to estimate numerically the spatial Fourier transform of the complex signal amplitude received across a linear antenna array. This operation yields the angular spectrum of the received signal convolved with the radiation pattern of the antenna array, so that the angular resolution of the calculated angular spectrum is thus limited. Nevertheless this is a straightforward technique for measuring the gross features of the angular spectrum of the received echo signal and thus for determining the apparent locations of any reflection points along the trail axis.

If Δr is defined as the effective length of the antenna array (i.e., Δr is the product of the number of equi-spaced antenna elements in the array and the inter-element spacing) and $\underline{\Delta r}$ is a vector of magnitude Δr and directed along the array axis in the (arbitrary) direction of positive $\underline{r}$, then the desired Fourier transform is

$$\tilde{E}[\cos(\underline{\tilde{k}_{20}},\underline{\Delta r}),t] = \frac{1}{\Delta r}\int_{-\frac{1}{2}\Delta r}^{\frac{1}{2}\Delta r} w(r)E(\underline{r},t)\exp\{-j\underline{\tilde{k}_{20}}\cdot\underline{r}\}dr \qquad (3.66)$$

where

$$|\underline{\tilde{k}_{20}}| = 2\pi/\lambda \qquad (3.67)$$

so that $\tilde{\underline{k}}_{20}$ is an estimator of the angle between the vectors $\tilde{\underline{k}}_{20}$ and $\underline{\Delta r}$, and w(r) is an amplitude weighting function used to suppress unwanted sidelobes induced in the computed spectrum by the finite range of integration.

For the case of the uniform distorted-trail model, the estimated angular spectrum $\tilde{E}_D[\cos(\tilde{\underline{k}}_{20},\hat{r}),t]$ is given by (from eqn. (3.35))

$$\tilde{E}_D[\cos(\tilde{\underline{k}}_{20},\hat{r}),t] = \sum_s E_{D,s}(0,t) \times W\left\{\frac{1}{2} k\Delta r\,[\cos(\tilde{\underline{k}}_{20},\hat{r}) - \cos(\underline{k}_{20},\hat{r}) + (\ell_s/R_{20})M(\hat{r})]\right\} \tag{3.68}$$

where

$$W\left\{\frac{1}{2}\,\underline{k}\cdot\underline{\Delta r}\right\} = \frac{1}{\Delta r}\int_{-\frac{1}{2}\Delta r}^{\frac{1}{2}\Delta r} w(r)\exp\{-j\underline{k}\cdot\underline{r}\}dr \tag{3.69}$$

is the Fourier transform of w(r) and the radiation pattern of the array for the wavelength λ, assuming the individual antenna elements have constant sensitivity over the relatively small angular range of interest.

Similarly, for the "small-scale" irregularity case of the fluctuating reflection-coefficient profile model, the estimated angular spectrum of the received signal $E_f[\cos(\tilde{\underline{k}}_{20},\hat{r}),t]$ is given by (from eqn. (3.45))

$$E_f[\cos(\tilde{\underline{k}}_{20},\hat{r}),t] = \sum_i E_{f,i}(0,t) \times W\left\{\frac{1}{2} k\Delta r\,[\cos(\tilde{\underline{k}}_{20},\hat{r}) - \cos(\underline{k}_{20},\hat{r}) + (\ell_i/R_{20})M(\hat{r})]\right\} \tag{3.70}$$

To this angular spectrum must be added the intense signal specularly scattered in the direction of $\underline{k}_{20}$ and given by

$$E_o\left[\cos(\tilde{k}_{20},\hat{r}),t\right] = E_{D,o}(0,t)\, W\left[\frac{1}{2}\,\Delta r \cdot (\tilde{k}_{20} - k_{20})\right] \qquad (3.71)$$

It can be seen from eqns. (3.68) and (3.70) that the precision with which the angular position of the individual echo components can be observed will be degraded by the finite beamwidth of the antenna array, and that individual components which lie within this beamwidth cannot be resolved; they will, however, result in a non-zero net amplitude being observed from their particular direction. This last assertion is based on the concept that, because of the phase term $\frac{1}{2}\pi(\ell_i/F_o)^2$ or $\frac{1}{2}\pi(\ell_s/F_o)^2$ of each individual component, the random values of ℓ_i or ℓ_s will result in each echo component having random phase. The expected amplitude of the sum of these components will in general be non-zero (cf. the Rayleigh distribution).

It is impossible to pursue this topic further without choosing a particular model for the statistical distribution of the scattering strengths σ, i.e., the products $g_i L_i$ and $g_o|L_s|$. For the simple (and likely unrealistic) case that the magnitudes of the scattering strengths are uniformly distributed over the interval

$$0 \leq \sigma \leq \sigma_{max} \qquad (3.72)$$

then the expected signal amplitude contained within the beamwidth in the direction of $\tilde{k}_{20}$ will be proportional to

$$(1/3)^{\frac{1}{2}} N(\tilde{k}_{20})\sigma_{max}$$

where $N(\tilde{k}_{20})$ is the number of scattering centres contained within the beamwidth centred on the direction of $\tilde{k}_{20}$. Thus it can be seen that

the effect of many weak scatterers could be the same as that of a somewhat smaller number of stronger scatterers, i.e., a fairly slowly varying angular spectrum, but the angular spectrum of a very small number of quite strong scatterers should be more highly structured.

3.6 The Reflection Coefficient and Echo Types

Much effort has been expended on determining the functional form of the reflection coefficient $g(\ell,t)$ and much of this effort has been summarized recently by Jones and Collins (1974). Basically, meteor echoes fall into three classes: underdense, overdense and transitional. The class of an individual echo is determined by the nature of the reflection coefficient of the associated meteor trail, and the parameter of a trail which has the greatest influence on its reflection coefficient is its line density.

An underdense echo is typically characterized by a fast rise ($<\frac{1}{4}$ second) to a peak amplitude, followed by an exponential decay with a time constant of order $\frac{1}{2}$ second. The fast rise in the echo amplitude occurs as the meteoroid passes through the specular reflection point and deposits there the electrons which reflect the transmitted signal.

An overdense echo is typically characterized by a fast rise in amplitude similar to that of the underdense echo, followed by a slower increase in amplitude and a long duration of order of one to tens and occasionally hundreds of seconds. Overdense echoes often display marked amplitude fading due to the constructive and destructive interference of echoes reflected from different parts of the same trail. An early and reasonable suggestion (McKinley and Millman, 1949) was that such multiple echoes could be caused by either the formation of additional specular reflection points as the trail is distorted by

ambient neutral wind shears, or the formation of scattering centres consisting of diffusing dense clouds of ionization due to irregular ablation of the meteoroid which generated the trail. Overdense echoes often terminate abruptly. It should also be noted that not all overdense echoes are characterized by a fast amplitude rise: some rise slowly. This is thought to be caused by the slow rotation of at least part of the trail by winds, so that the specular reflection condition is satisfied only after the trail has been formed.

Transitional echoes, as the name implies, are somewhere between underdense and overdense in behavior. They first display a brief period of overdense-type behavior, during which the echo amplitude continues to increase after its initial sharp rise; this is followed by an underdense-type exponential amplitude decay, although with a longer time constant than for a true underdense echo from an underdense trail occurring at the same height.

3.6.1 Underdense Echoes

For meteor trails with line densities less than 10^{13} electrons per metre, it can be shown that the electrons can be considered as independent scatterers of the incident radio wave (Born approximation), and the trail is referred to as being underdense. Then its reflection coefficient $g_{un}(\ell,t)$ is given by

$$g_{un}(\ell,t) = q_{eff}(\ell,t)\sqrt{\sigma_e}\cos\theta_p \qquad (3.73)$$

where q_{eff} is the effective line density of the trail and is defined by eqn. (3.75) below, $\sigma_e = \mu_o^2 e^4/4\pi m_e^2 \approx 1.0 \times 10^{-28} m^2$ is the classical electron scattering cross-section in rationalized MKS units and θ_p is

the angle between the incident electric-field vector and the electric-field vector of the wave scattered in the direction of the receiving antenna system.

It is usual to consider a trail model with the radial distribution of the volume density N of the electrons about the trail axis given by

$$N(\ell,\rho_T,t) = \left\{q_o(\ell)/\pi[4D(\ell)t + \rho^2_{T,0}(\ell)]\right\} \exp\left\{-\rho_T^2/[4D(\ell)t + \rho^2_{T,0}(\ell)]\right\}. \tag{3.74}$$

where $q_o(\ell)$ is the total number of electrons per unit length of trail (initial line density), $\rho_T(\ell)$ is the radial distance from the trail axis, $\rho_{T,0}(\ell)$ is the initial trail radius just after trail formation, and $D(\ell)$ is the ambipolar diffusion coefficient. All of these parameters are assumed to be functions of the axial location ℓ.

On the basis of this model, it can be shown (e.g., McKinley, 1961) that

$$q_{eff}(\ell,t) = q_o(\ell)\exp(-4\pi^2\rho^2_{T,0}/\lambda^2\sec^2\phi_f)\exp[-t/T_{un}(\ell)] \tag{3.75}$$

where

$$T_{un}(\ell) = \frac{\lambda^2\sec^2\phi_f}{16\pi^2 D(\ell)} \tag{3.76}$$

and λ and ϕ_f are as defined earlier (Section 3.2 and eqn. (3.25) respectively).

Finally, an approximate expression for $E_{un}(\underline{r},t)$, the received complex electric-field amplitude of the wave reflected by an underdense meteor trail, can be written as

$$E_{un}(\underline{r},t) = \frac{V_0}{R_{10}R_{20}} \int_{trail} g_{un}(\ell,t) \exp[j\phi_D(\ell,\underline{r},t)]d\ell \qquad (3.77)$$

where

$$g_{un}(\ell,t) = [illegible]_o(\ell) \sqrt{\sigma_e} \cos\theta_p \exp[-4\pi^2\rho_{T,0}^2(\ell)/\lambda^2\sec^2\phi_f] \exp[-t/T_{un}(\ell)] \qquad (3.78)$$

is the explicit expression for the underdense reflection coefficient.

3.6.2 Overdense Echoes

A meteor trail is considered to be overdense when the electron density of the trail plasma is sufficiently great that the incident radio wave does not fully penetrate the meteor trail, but rather undergoes critical reflection and is reflected as if by a metallic cylinder (Greenhow, 1952). This model is approximately valid for trails with line densities greater than 10^{15} electrons per metre. A more accurate model considered by Manning (1953, 1963) takes into account refraction of the incident wave by the electrons surrounding the apparent reflecting cylinder, but this latter approach is amenable only to direct numerical calculation. Qualitative understanding can be gained, however, by examination of the reflecting cylinder model for forward scattering (Hines and Forsyth, 1957), even though Jones and Collins (1974) have shown by numerical integration of the full-wave reflection equations that the reflection coefficient thus obtained is about 10% too large in the limiting case of backscatter geometry.

Hines and Forsyth showed that for a cylindrical meteor trail with uniform radius $\rho_c(t)$ and infinite length, the power flux of the reflected signal as observed at the receiving antenna, S_{HF}, is given (in MKS units) by

$$S_{HF}(t) = \frac{P_0 G\, \rho_c(t)\, \cos^2\theta_p\, \cos\phi_f}{8\pi\, R_{10} R_{20} (R_{10} + R_{20})\, \sin^2(k_o, \ell)} \qquad (3.79)$$

By equating $S_{HF}(t)$ with $|E(o,t)|^2/Z_0$ as given by eqn. (3.34) for the particular case of an infinite, straight trail with constant reflection coefficient, it can readily be shown that the squared magnitude of the effective reflection coefficient g_{ov} is given by

$$|g_{ov}(t)|^2 = \frac{\pi \rho_c(t)}{\lambda} \cos^2\theta_p \cos\phi_f \qquad (3.80)$$

If it is assumed that $g_{ov}(t)$ introduces only a phase shift which is constant along the length of the trail and hence can be ignored and it is further assumed that $\rho_c(t)$ can be replaced by $\rho_c(\ell,t)$, a slowly varying function of ℓ such that everywhere

$$\left| \left(\frac{\partial g}{\partial \ell} \right)_t \right| \ll \frac{1}{F_o} , \qquad (3.81)$$

then finally

$$g_{ov}(\ell,t) = [(\pi/\lambda)\rho_c(\ell,t)\cos^2\theta_p \cos\phi_f]^{\frac{1}{2}} \qquad (3.82)$$

It can be seen that the behavior of $g_{ov}(\ell,t)$ is governed by the effective value of $\rho_c(\ell,t)$.

Hines and Forsyth proceeded by assuming that since the critical electron density N_c required to refract an electromagnetic wave through an included angle $2\phi_f$ is given by

$$N_c = \pi \cos^2\phi_f/\lambda^2 r_e \qquad (3.83)$$

where $r_e = (\sigma_e/4\pi)^{\frac{1}{2}} \approx 2.8 \times 10^{-15}$ m is the classical electron radius, an effective value for ρ_c could be derived by substituting eqn. (3.83) for N_c into eqn. (3.74). The resulting formula for calculating $\rho_c(\ell,t)$ is then

$$\rho_c(\ell,t) = \left\{[4D(\ell)t + \rho^2_{T,0}(\ell)] \ln \left[\frac{q_o(\ell)\, r_e \lambda^2 \sec^2\phi_f}{\pi^2[4D(\ell)t + \rho^2_{T,0}(\ell)]}\right]\right\}^{\frac{1}{2}} \qquad (3.84)$$

Equation (3.84) can be rewritten in the normalized form

$$\rho_c(\ell,t) = \rho_{c,max}(\ell)\left\{X(\ell,t)[1 - \ln X(\ell,t)]\right\}^{\frac{1}{2}} \qquad (3.85)$$

where

$$X(\ell,t) = [4D(\ell)t + \rho^2_{T,0}(\ell)]/\rho^2_{c,max}(\ell) \qquad (3.86)$$

and

$$\rho_{c,max}(\ell) = \frac{[q_o(\ell)\, r_e]^{\frac{1}{2}} \lambda \sec\phi_f}{\pi \exp\left[\frac{1}{2}\right]} \qquad (3.87)$$

is the maximum value of $\rho_c(\ell,t)$, which occurs at the time

$$t_{max}(\ell) = [\rho^2_{c,max}(\ell) - \rho^2_{T,0}(\ell)]/4D(\ell) \qquad (3.88)$$

The Hines and Forsyth model predicts that $g_{ov}(\ell,t)$ will fall to zero when $\rho_c(\ell,t)$ falls to zero. This happens when $\ln X(\ell,t) = 1$, which occurs at the time $T_{ov}(\ell)$, where

$$T_{ov}(\ell) = \frac{\rho_{c,max}^2(\ell)\exp(1) - \rho_{T,0}^2(\ell)}{4D(\ell)} \qquad (3.89)$$

$T_{ov}(0)$ is thus the expected duration of the overdense echo as predicted by this model.

The ray-tracing results of Manning (1959) show that $T_{ov} \propto \sec^{\mu}\phi_f$ where μ ranges from the value 0.3 for a trail oriented perpendicular to the transmitter-receiver axis to the value 2 for a trail oriented parallel to the transmitter-receiver axis. This discrepancy from the constant value of 2 predicted by the Hines and Forsyth model Manning attributed to the neglect of the refracting effects of the outer electrons of the trail.

After the reflecting cylinder has vanished, the remaining electron cloud will have diffused radially to such a great extent (i.e., several wavelengths across) that it will scatter only incoherently and hence very weakly. Therefore T_{ov} does in fact define a sharp cutoff of echo amplitude.

Finally, an approximate expression for $E_{ov}(\underline{r},t)$, the electric field of a radio wave reflected by an overdense meteor trail, can be written as

$$E(\underline{r},t) = \frac{V_0}{R_{10}R_{20}} \int_{trail} g_{ov}(\ell,t)\exp[j\Phi_D(\ell,\underline{r},t)]d\ell \qquad (3.90)$$

where

$$g_{ov} = \left\{q_0(\ell)r_e\exp(-1)[X(\ell,t)(1 - \ell n\, X(\ell,t))]\right\}^{\frac{1}{4}}\cos\theta_p \qquad (3.91)$$

is the explicit expression for the Hines and Forsyth overdense reflection coefficient.

3.6.3 Transitional Echoes

The transition region between underdense and overdense echoes occurs for trails having line densities in the range 10^{13} electrons per metre to 10^{15} electrons per metre (Jones and Collins, 1974). For this range of line densities the reflection coefficient changes from varying linearly as the line density q_o to varying as the fourth root of q_o. There appears to be no simple physical model which both can account for this change and is also amenable to non-numerical analysis.

The behavior of transitional echoes, as described in Section 3.6 above, can however be understood qualitatively on the bases of the discussions in Sections 3.6.1 and 3.6.2. Immediately after a transitional trail has been formed, the overdense-trail model may be able to describe its behavior for a brief time; but the critical-cylinder radius quickly falls to zero (if indeed it was ever non-zero, as in the case of less dense transitional trails). At this time, however, the trail has not yet diffused sufficiently for the electrons from different parts of its cross-section either to re-radiate independently or to interfere destructively. Thus its echo does not behave in a true underdense manner. The situation is that of an almost-planar incident electromagnetic wave being refracted by a dielectric cylinder with a Gaussian radial variation of index of refraction. It is this problem which Jones and Collins have examined numerically.

The relevance of transitional echoes to the present experiment is two-fold. Firstly, the limited sensitivity of the system used meant that most detected echoes were either transitional or overdense. Secondly, if a meteoroid were to ablate irregularly, and in particular to emit bursts of ionization, a trail in the transitional regime would

be more likely to have irregularities which were overdense in nature. It should be possible to detect such overdense secondary scatterers, if they existed, by observing their time-dependent behavior.

CHAPTER 4

DATA RECORDING AND REDUCTION

4.0 Period of Observations

The data were recorded on the afternoon of 3 January 1973, during the annual occurrence of the Quadrantid meteor shower. It was decided to observe shower rather than sporadic meteors, so that the initial orientations of the trails would be known. This knowledge was later used to deduce the locations of the trails in the sky. The Quadrantid shower was chosen partly because of its high peak intensity and favorable radiant location and partly by default: previous attempts to record data during the latter half of 1972 had been thwarted by equipment malfunctions and failures.

In the days of early January at times near 1600 EST the Quadrantid radiant lies west of lower transit relative to the path mid-point. The shower meteoroids then pass from north-west to south-east nearly orthogonal to the transmitter-receiver path and at a zenith angle of about 68°. This geometry shortens the radius of the principal Fresnel zone as much as possible and coincidently places the longer axis of the antenna array as nearly parallel as possible to the axes of the trails, thus affording the greatest possible resolving power along the trail axes.

4.1 Recording Procedure

The data were recorded using the antenna layout described in Section 2.3.3, according to the following cyclic schedule. One 2400-

foot reel of digital magnetic tape was filled with data during each half-hour cycle. At the beginning of each cycle, an ionogram covering the frequency range 3 to 30 MHz was recorded, digitally processed, and displayed on the graphic printer. The main purpose of the ionograms was to verify that the transmitter was synchronized and operating. This procedure required approximately three and one-half minutes. About one-half minute later, at the start of the fourth minute of the cycle, the first of ten consecutive frequency sweeps running from 20.0 to 30.0 MHz at a sweep-rate of 100 kHz/sec was initiated. Subsequent sweeps were initiated at successive two-minute intervals, with no data being recorded during the intervening 20-second intervals. This schedule allowed six minutes and 20 seconds at the end of each half-hour cycle for the operator to rewind and change the magnetic tape.

The choices of frequency limits and sweep rate were made on the following bases. At frequencies below 20 MHz, significant interference due to ionospherically propagated signals from fixed-frequency transmitters was observed. The upper frequency limit of the system was 30 MHz. Between these limits a sweep rate of 100 kHz/sec yielded continuous observations over a 100 second recording period and a reasonable path-length window of about 90 km using 15 Hz receiver output low-pass filters (Section 2.2.2).

One second before the start of each frequency sweep, a descriptive header was written on the tape. Each header uniquely identified the subsequent data and specified the systematic parameters under which they were recorded. A typical data header is reproduced as Fig. 4.1.

```
DAY   3, 16:40:00 (1973)
D.F. RECORDING                          PROGRAM IONDF 1.4   NOV 1972

LOW LIMIT FREQUENCY (MHZ) = 20.000000
HIGH LIMIT FREQUENCY (MHZ) = 30.000000
SWEEP RATE (KHZ/SEC) =  100.00
SWEEP MODE (UP,DOWN,ALT.)  : UP
NUMBER OF SWEEPS (UP OR DOWN) =  1.0
BANDWIDTH OF RECEIVER OUTPUT FILTER (HZ) =  15.0
NUMBER OF RECEIVERS= 64.
NUMBER OF OUTPUTS PER RECEIVER = 2.
FIRST RCVR IS #  27.
SCAN RATE (HZ) =  64.00
DF RANGE OFFSET (MSEC) =  0.55
```

Figure 4.1. A typical data header

The information contained in each header included: sweep start time, sweep lower limit frequency, sweep upper limit frequency, sweep rate, sweep mode (always "up", or from lower to upper-limit frequency), number of frequency sweeps per cycle (always 1), the bandwidth of the receiver output low-pass filters, the number of outputs per receiver (2 for this experiment, but could have been 3 if the automatic gain control signals had been recorded), the first receiver number (a value used by the computer to set the start location for a multiplexer scan of the receiver outputs), the scan rate (the number of times per second that each pair of receiver outputs was sampled) and the DF range offset (the differential delay times τ_o (Section 2.2.2) introduced by the sample timer to shift the frequencies of the expected output signals to within the receiver output passband). The DF range offset is a differential time delay added to another time delay of about 2.68 msec previously introduced by the sample timer to compensate for the minimum echo delay time of about 3 msec.

4.2 Preliminary Reduction of the Data

The recorded data were read from the digital magnetic tape into the memory of the Control Data Corporation CYBER 73 Computer at the Computing Centre of the University of Western Ontario, and data from the two outputs of a single receiver were selected for analysis. These data were partitioned into segments of ¼ second duration, and a Hanning (cosine-bell) window was applied to each segment of data. The digital Fourier transform of each segment of data was then calculated using the complex fast Fourier transform routine FAST4 (written by the author) and the common logarithms of the squared magnitudes of the estimated frequency spectrum were calculated.

The set of spectra thus produced was displayed on the computer line-printer in the form of a quasi-intensity-modulated plot of receiver output frequency (which is linearly related to echo range) versus instantaneous radio frequency (which is linearly related to time) at the start of each quarter-second segment. Signals showing the characteristic fast rise in amplitude of a meteor echo for which the trail formation has been observed were searched for visually. A sample record showing a meteor echo is displayed as Fig. 4.2.

The numerals "0", "1", "2", "3" ... in Fig. 4.2 represent the magnitude of the receiver output voltage at a particular offset range, in units of 5 dB below 10 volts amplitude. Thus a "0" represents a voltage in the range 5.62 to 10.0 volts, a "1" represents a voltage in the range 3.16 to 5.62 volts, etc.. This crude processing technique, in which such effects as antenna-cable attenuation, receiver gain correction and receiver-output gain and phase imbalances were ignored, was efficient in its use of computer time and also gave sufficient resolution in estimates of both propagation path length ($\pm$3 km) and time (¼ second) to allow unambiguous detection of radio meteor echoes. More elaborate processing schemes at this stage would have been wasteful, as only about 3% of any tape contained potentially useful data.

4.3 Detailed Reduction of the Data

In Chapter 3 it was shown that the echo signal from an initially straight meteor trail as observed across the antenna array will consist of a strong specular component and perhaps some small superimposed distortions. The specular component will give rise to a constant amplitude and a linearly varying phase across the array; the effects of

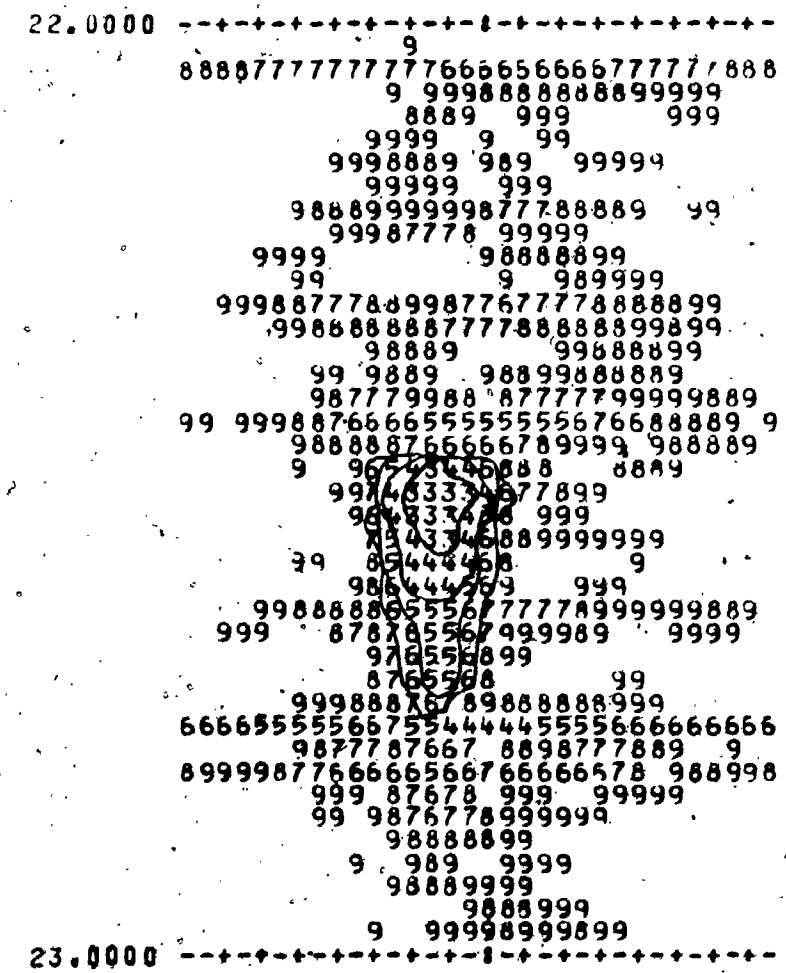

Figure 4.2. Range-time plot of a meteor echo observed at 16:40:24.750 EST on January 3, 1973

small-amplitude echoes scattered from other parts of the trail will appear as small additive fluctuations in the amplitude and phase across the array.

It appeared that an appropriate data-reduction technique could be based on the least-squares fitting of straight lines to the observed amplitude and phase data, and then analyzing the determined phase slopes, average amplitudes, amplitude slopes, and residual amplitude and phase fluctuations. The least-squares best fit (LSBF) technique was applied in an iterative fashion, as outlined below.

4.3.1 Estimation of Echo Amplitude and Angle of Arrival

The first step in the procedure was to read a single scan of data from the 64 receivers into the memory of the CYBER 73 computer, and to calibrate these data using the methods outlined in Appendix A. The amplitudes and phases of the data were extracted, and the 360° phase discontinuities in the phase data were corrected by using a LSBF phase-slope derived from the phases observed at 25-foot intervals in the middle of the array. A straight-line LSBF subroutine was then applied to the corrected phases of the outputs from the 32 receivers connected to antennas spaced at 125 foot intervals along the long array axis. This was done to estimate the instantaneous time-varying phase at the centre of the array. If the RMS scatter of the 32 phases about the fitted linear phase estimate was greater than 75° (an arbitrarily chosen limit beyond which the estimated angle of arrival as derived from the phase-slope was almost always grossly in error) the scan of data was not further analyzed. Instead, the raw data and the estimated angle of arrival were printed, and the next scan of data

was read. Otherwise the estimated initial phase was subtracted from each phase datum of the scan, to eliminate the time-varying phase component due to the range-related difference frequency. This procedure shifted all the receiver-output frequencies to zero, in a process akin to complex demodulation. Estimates of the standard deviation of the initial phase ranged typically from about 1° of phase at peak echo amplitude to about 8° near the end of the echo.

The amplitude and shifted phase data were then recast in complex-quadrature (I + jQ) form, and the reconstituted data from the 58 receivers in the long array were passed through a bank of 58 recursive digital filters which simulated RC exponential integrators (Gold and Rader, 1969). The effective time constant of the filters was 1/16 second, for a 3 dB bandwidth of $\pm$2.5 Hz and an effective noise bandwidth of 7.4 Hz ($\pm$3.7 Hz) if the noise bandwidth of the receivers is assumed for ease of calculation to be 32 Hz ($\pm$16 Hz). This filtering procedure resulted in an improvement of about 6.4 dB in signal-to-noise ratio (SNR).

The amplitudes and phases of the filtered complex data were again extracted and a LSBF straight line was again fitted to the phase data from the 32 receivers with 125 foot antenna spacing. This time the fitted linear phase variation was subtracted from the phase data from all 58 receivers in the long array, to reduce the spatial frequency and any residual phase-shift in the data to near zero. The data were again recast in complex quadrature form, and a 375-foot running mean was passed over the complex data from all 58 receivers in the long array. This procedure smoothed the data, incorporated the information from the 26 additional receivers in the centre of the array,

standard deviation of the individual receiver outputs about a LSBF straight line fitted to the absolute amplitudes observed across the antenna array. The points marked by X's are sets of data for which a LSBF line could not be fitted to the phase data, due to the effect of interfering fixed-frequency transmissions (Section 4.3.1 and Appendix C). Particular times of interest are indicated by arrows at the times "A", "B", "C" and "D".

Figure 5.2 shows the temporal behavior of the LSBF linear phase-slope estimate of the angle of arrival $(\underline{k}_{20}, \hat{r})$. The errors bars indicate a spread of plus and minus the estimated standard deviation of the estimated angle, and the vertical bar at the right of the figure indicates the estimated angular change to be expected for an axial change of 1 km in the location of the specular reflection point. The arrows at A", "B", "C" and "D" correspond to the same times as those in Figure 5.1.

Figure 5.3 shows the temporal bahavior of the fractional amplitude variation of the echo signal received across the antenna array. This parameter is defined as the LSBF estimate of the linear slope of the amplitude across the array, multiplied by half the length of the array and divided by the mean absolute amplitude; thus, from eqn. (3.58), this parameter should be an indicator of the presence in the received signal amplitude diffraction pattern of scale sizes greater than the length of the array. The error bars again indicate a spread of plus and minus one standard deviation as calculated from the estimated standard deviation of the amplitude slope, and again the arrows at "A", "B", "C" and "D" correspond to the same times as those in Figures 5.1 and 5.2

From the estimated initial angle of arrival, the estimated echo range $2R_o$, an assumed location of the Quadrantid radiant point with

$$\Delta(\underline{k_{20}},\hat{r}) = (\lambda/360^{o})\ \csc(\underline{k_{20}},\hat{r})\ \Delta(\partial\phi/\partial r). \qquad (4.2)$$

A LSBF straight line was also fitted to the amplitudes, and such parameters as the normalized amplitudes and the phase deviations from the LSBF linear phase front for each receiver, the mean signal amplitude and its standard deviation (in volts), the amplitude slope and its standard deviation (in volts/metre), the F-ratio of the scatter of the amplitudes about their mean value relative to their scatter about the LSBF stright line, as well as the initial phase angle and its standard deviation (in degrees of phase), the phase slope and its standard deviation (in degrees of phase/metre), the calculated angle of arrival and its standard deviation (in degrees of angular deviation from $(\underline{k_{20}},\hat{r}) = 90^{o}$), and the RMS scatter of the individual phase data about the LSBF straight line (in degrees of phase) were output by the computer.

4.3.2 Detection of Secondary Echoes

Because small-magnitude quasi-sinusoidal amplitude and phase fluctuations with lifetimes of several integrator time-constants were observed in the data (Section 5.1 *et seq.*), it was decided to digitally Fourier transform the data from the antenna array or spatial domain to the angle-of-arrival domain. This procedure offered the possibility of determining if these amplitude and phase fluctuations were, in fact, due to the existence of secondary echoes scattered by the meteor trail and arriving at angles sufficiently remote from $(\underline{k_{20}},\hat{r})$ to be resolvable.

At time-intervals of $1/16^{th}$ second, sets of 32 data recorded at 125-foot (38.1 m) antenna element spacing were recast into complex-

quadrature form, after the final LSBF linear phase slope across the array had been subtracted. Before the digital Fourier transform was computed, each set of data was multiplied by a Dolph-Chebyshev weighting function (Dolph, 1946). (The spatial weighting functions were calculated using the Fourier-transform technique developed by Stegen (1953).) Amplitude weighting of the spatial-domain data was used in order to reduce the amplitude of unwanted sidelobes in the computed angular spectra (Section 3.5.4).

There were two reasons for choosing Dolph-Chebyshev weighting functions. First, for antenna element separations of more than one-half wavelength, Dolph-Chebyshev weighting yields an optimum compromise of maximum angular resolution for a specified uniform sidelobe level (Riblet, 1947). Second, the flexibility of having sidelobe level variable as an independent parameter ensured that angular resolution was not needlessly degraded in attempts to achieve sidelobe suppression beyond that realizable in the face of the limits set by systematic distortions and external noise levels. Such needless degradation can occur when fixed-parameter weighting functions such as the cosine-bell (Hanning) or the elevated cosine-bell (Hamming) functions are used.

CHAPTER 5

EXPERIMENTAL RESULTS

5.0 Introduction

Approximately thirty-five meteor echoes that were recorded on the afternoon of 3 January 1973 showed the expected fast amplitude rise (less than ½ second) characteristic of an echo for which the trail formation has been observed. Of these thirty-five echoes, three typical examples have been analyzed in detail below. These three echoes were chosen on the basis of their amplitude behavior, which ranged from smooth underdense to both smooth and slightly fluctuating transitional, their apparent good signal-to-noise ratio (SNR), the absence of strong fluctuations in angle of arrival, and relative freedom from external interference. As well, the observed echo ranges and angles of arrival were consistent with the assumption that all three echoes were due to Quadrantid meteors. The use of shower meteors permitted quantitative estimates of the trail locations (Appendix B) and the magnitudes of the observed wind shears (Section 5.1 *et seq.*).

The echo parameters investigated were derived using the techniques described in Section 4.3.1. These parameters are: the temporal history of the absolute amplitude of the echo, averaged across the antenna array; the echo angle of arrival as deduced from the least-squares best-fit (LSBF) linear phase slope across the array; and the fractional variation of the echo amplitude observed across the array. This last parameter is defined by the expression

$$\frac{\Delta|E|}{|E|_{avg}} = \frac{\frac{1}{2}\Delta r}{|E|_{avg}} \left(\frac{\partial|E|}{\partial r}\right)_{LSBF} \qquad (5.1)$$

where $|E|_{avg}$ is the spatial average of the instantaneous echo amplitude observed across the array, $(\partial|E|/\partial r)_{LSBF}$ is the instantaneous LSBF estimate of the slope of the absolute amplitude across the array, Δr is the effective length of the antenna array (Section 3.5.4), and $\Delta|E|/|E|_{avg}$ is the fractional amplitude variation (cf. Section 3.5.3).

The data were also investigated for evidence of secondary echoes. These investigations included visual examination of plots of the instantaneous echo amplitude and phase across the array and application of the spatial Fourier-transform techniques described in Section 4.3.2. As well, additional theoretical concepts beyond those of Chapter 3 were developed to interpret the results of these investigations.

5.1 Echo I - An Underdense Echo

The first echo to be investigated was an apparently underdense echo observed starting at 16:10:20.375 EST on 3 January 1973. For convenience this echo is referred to as Echo I below.

5.1.1 Spatially Averaged Parameters - Echo I

Figure 5.1 shows the temporal behavior of the absolute amplitude of Echo I, averaged across the antenna array using the procedure described in Section 4.3.1. The longer error bars indicate a spread of plus and minus the estimated instantaneous standard deviation of the individual receiver outputs about the average absolute amplitude, and the shorter error bars indicate a spread of plus and minus the estimated

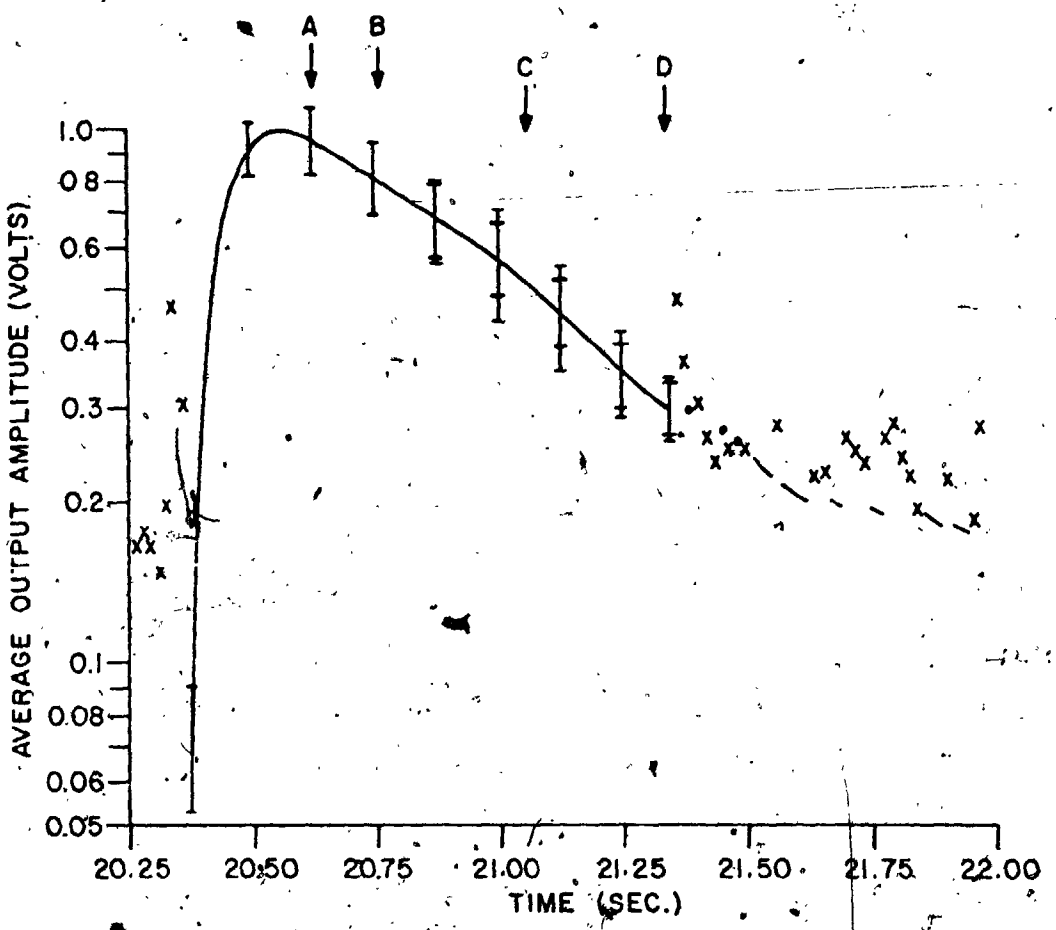

Figure 5.1. Spatially averaged amplitude - Echo I

standard deviation of the individual receiver outputs about a LSBF straight line fitted to the absolute amplitudes observed across the antenna array. The points marked by X's are sets of data for which a LSBF line could not be fitted to the phase data, due to the effect of interfering fixed-frequency transmissions (Section 4.3.1 and Appendix C). Particular times of interest are indicated by arrows at the times "A", "B", "C" and "D".

Figure 5.2 shows the temporal behavior of the LSBF linear phase-slope estimate of the angle of arrival $(\underline{k}_{20}, \hat{r})$. The errors bars indicate a spread of plus and minus the estimated standard deviation of the estimated angle, and the vertical bar at the right of the figure indicates the estimated angular change to be expected for an axial change of 1 km in the location of the specular reflection point. The arrows at A", "B", "C" and "D" correspond to the same times as those in Figure 5.1.

Figure 5.3 shows the temporal bahavior of the fractional amplitude variation of the echo signal received across the antenna array. This parameter is defined as the LSBF estimate of the linear slope of the amplitude across the array, multiplied by half the length of the array and divided by the mean absolute amplitude; thus, from eqn. (3.58), this parameter should be an indicator of the presence in the received signal amplitude diffraction pattern of scale sizes greater than the length of the array. The error bars again indicate a spread of plus and minus one standard deviation as calculated from the estimated standard deviation of the amplitude slope, and again the arrows at "A", "B", "C" and "D" correspond to the same times as those in Figures 5.1 and 5.2

From the estimated initial angle of arrival, the estimated echo range $2R_o$, an assumed location of the Quadrantid radiant point with

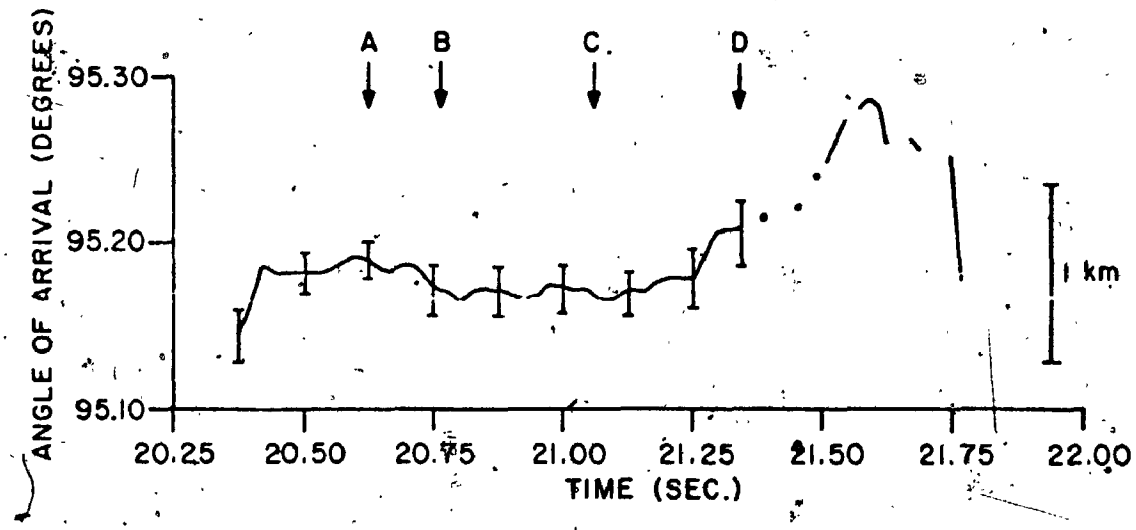

Figure 5.2. Angle of arrival from LSBE phase slope - Echo I

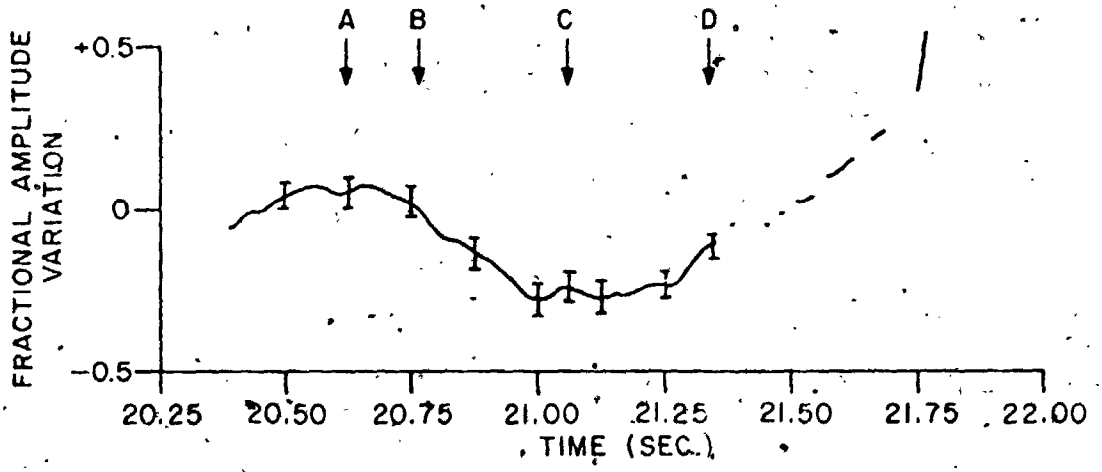

Figure 5.3. Fractional amplitude variation - Echo I

celestial coordinates of Right Ascension = 232°, Declination = 50° (Millman, 1973), and a detailed knowledge of the antenna locations, it was possible to estimate several geometric parameters pertaining to the location of the meteor trail (Appendix B and Sections 3.1-3.3). These parameters have been summarized in Table 5.1. It is noted in passing that the estimated errors in the parameters quoted in Table 5.1 were based solely on the uncertainty of ±3 km in the observation of $2R_o$; no account has been taken of the effects of zenith attraction or possible errors in the assumed location of the radiant point.

In Figure 5.1, the plotted data are weighted means of the absolute echo amplitudes from 58 receiver outputs. Hence the estimated standard deviations of the means are at most $1/6^{th}$ of the indicated error bars. At the time indicated by the arrow "C", there was a discontinuity in the slope of the logarithm of these mean amplitudes. The measured decay time constant between the times "A" and "C" is 0.73 seconds, and between the times "C" and "D" is 0.50 seconds. From eqn. (3.76) estimated values of the ambipolar diffusion coefficient D, based on these two estimates of T_{un}, a radio wavelength of 13.6 m and an estimated value for sec ϕ_f of 3.5, are 20 m^2/sec and 28 m^2/sec respectively. If it is assumed that D(h) as a function of height is given by an empirical formula based on the experimental results of Greenhow and Neufeld (1955):

$$D(h) = 5.8 \exp[(h-95)/6.5] \qquad (5.2)$$

where h is the height in km above the surface of the earth and D is in m^2/sec, then estimated heights of reflection based on these two values of T_{un} would be 103.0 km and 105.2 km respectively. While these height estimates may be in absolute error by as much as ±5 km, their 2.2 km

TABLE 5.1

Geometric Parameters of the Analyzed Echoes

TIME	ECHO I 16:10:20	ECHO II 16:40:24	ECHO III 15:51:17
$2R_o$ (km)	948 ± 3	948 ± 3	945 ± 3
R_{20} (km)	480 ± 16	644 ± 16	439 ± 17
h (km)	106 ± 4	101 ± 3	100 ± 5
$(\underline{k_{20}}, \hat{r})$ (°)	95.18 ± 0.01	92.96 ± 0.01	96.11 ± 0.02
$(\hat{\ell}, \hat{r})$ (°)	21.4	18.8	23.7
$(\underline{k_{20}}, \hat{\ell})$ (°)	90.2	86.5	92.4
χ (°)	68.5	71.4	66.5
ϕ_f (°)	73.9 ± 0.5	72.7 ± 0.8	74.4 ± 0.5
λ (m)	13.6	13.0	10.9
F_o (km)	1.27	1.17	1.13
$M(\hat{r})$	0.93	0.95	0.91
α	0.9302	0.9457	0.9157
β	-0.3671	-0.3186	-0.3996
γ	-0.0037	-0.0639	-0.0436
ξ_o (km)	48.2 ± 1.6	39.7 ± 1.0	50.7 ± 2.0
η_o (km)	122.2 ± 4.2	115.1 ± 2.4	115.8 ± 4.6
ζ_o (km)	-7.6 ± 15	-117.6 ± 15	35.0 ± 16
$\hat{n}_o \cdot \hat{i}$	0.3653	0.3225	0.3990
$\hat{n}_o \cdot \hat{j}$	0.9241	0.9349	0.9113
$\hat{n}_o \cdot \hat{k}$	-4.4×10^{-3}	-0.1189	2.0×10^{-2}

difference, which is dependent only on the assumed scale height for D(h) of 6.5 km, ought to be accurate to within 1 km. Also, these height estimates compare favorably with the geometric estimate for the height of reflection of 106(±4) km.

For an estimated local zenith angle of 68.5°, a vertical displacement of 2.2 km would correspond to a displacement of -6.0 km along the trail axis. Using either eqn. (3.68) or eqn. (3.70) and estimated values for R_{20} of 480 km and $M(\hat{r})$ of 0.93, it can be shown that such a displacement of the specular reflection point would lead to a readily observed decrease of -0.67° in the angle of arrival. Figure 5.2 shows no such decrease.

Figure 5.3, however, shows that a significant negative fluctuation in the fractional amplitude deviation across the array began to occur almost as soon as the mean signal amplitude began to decay, indicating that the amplitude of the signal received at the northwest end of the array was decaying more slowly than that received at the southeast end. This fluctuation reached its greatest magnitude at the time "C", the time of occurrence of the discontinuity in the amplitude decay time constant, and then began to become smaller.

5.1.2 Spatial Phase and Amplitude Observations - Echo I

Figures 5.4 and 5.5 show representative samples at 1/16th second intervals of the basic data from which the averaged data shown in Figures 5.2 and 5.3 were derived. In both Figures 5.4 and 5.5, time is increasing downwards, and the data are plotted as vertical offsets from equi-spaced horizontal baselines. Distance along the array axis is increasing from left to right, with the left-hand end of each base-

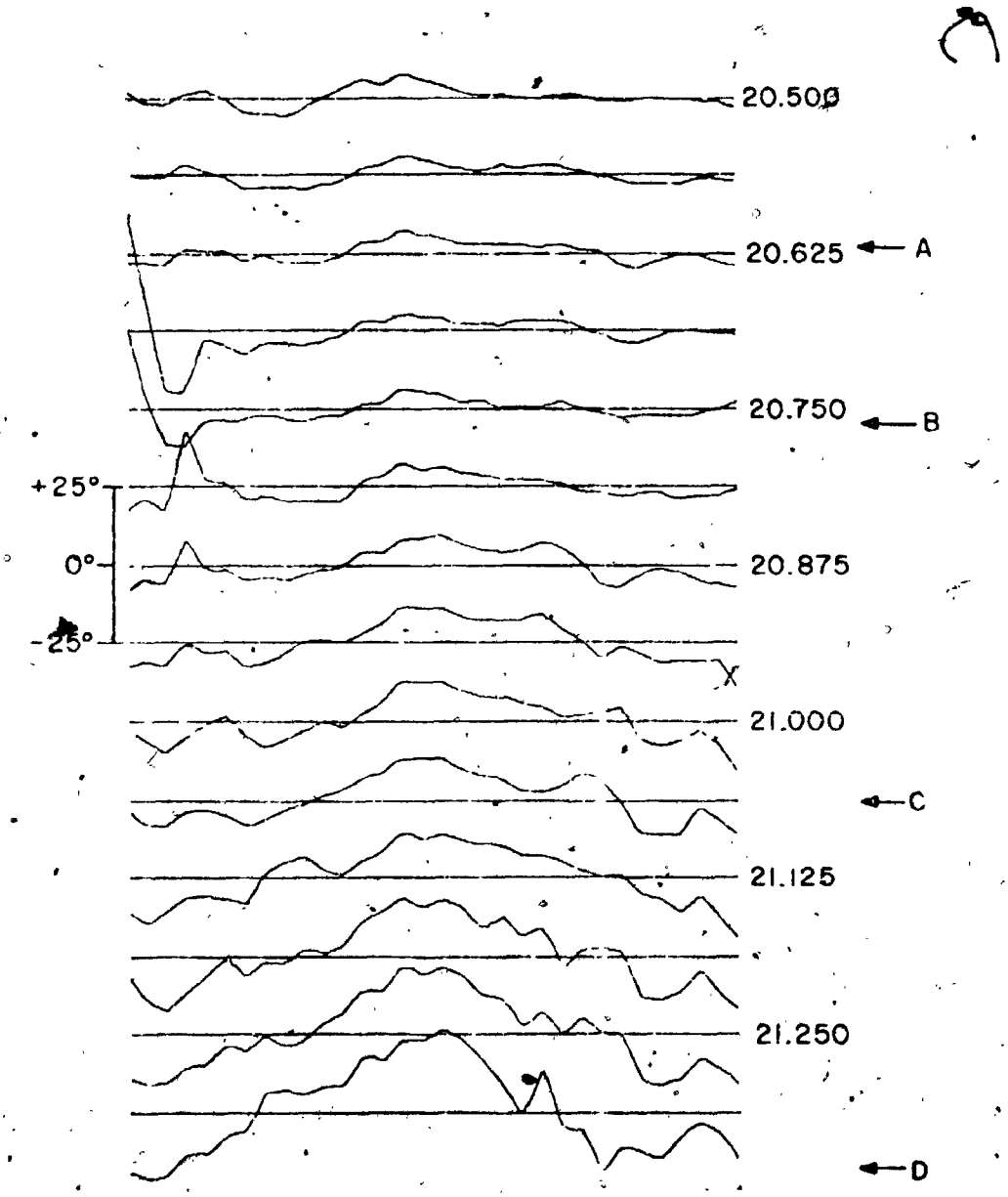

Figure 5.4. Spatial phase fluctuations - Echo I

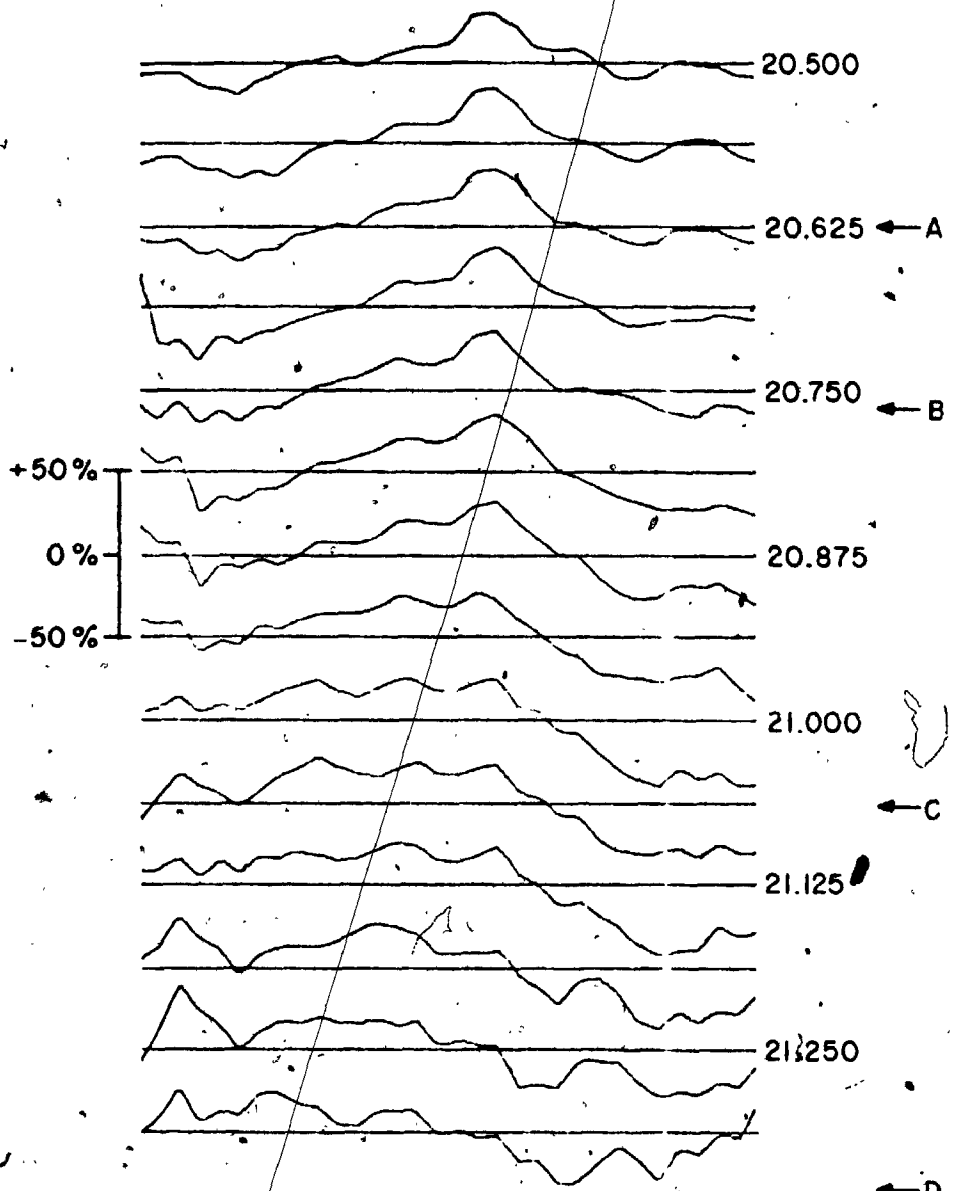

Figure 5.5. Spatial amplitude fluctuations - Echo I

line corresponding to the northwest (negative) end of the array. Again arrows mark times "A", "B", "C" and "D", which are the same times as marked in Figures 5.1 through 5.3.

Figure 5.4 shows the smoothed phase deviations across the antenna array after the LSBF linear phase slope has been subtracted. The vertical bar indicates a differential phase change of $\pm 25^{o}$.

Figure 5.5 shows the smoothed and normalized absolute echo amplitude observed at the receiver outputs from across the array. The vertical bar indicates a fractional change in absolute amplitude of $\pm 50\%$ relative to the mean absolute amplitude across the array.

Both figures show that there existed spatial fluctuations in the echo amplitude and phase with scale-size comparable to and less than 1.2 km length of the array, and the relative magnitude of these fluctuations tended to increase and the scale-size to decrease as the echo amplitude decayed.

As well, there is evidence in both figures of the effects of external noise and systematic distortion on the data. For example, about $1/16^{th}$ second after the time "A", the effect of an interfering noise-burst was observed in the outputs of the receiver connected to the northwest end of the array. The amplitude and phase discontinuities due to this noise-burst died out within about two integrator time-constants ($1/8^{th}$ second). The small-scale irregularities apparent in the data recorded near the end of the echo are also attributed to external noise effects, which became more dominant as the echo amplitude decayed and the SNR decreased. As well, these figures show the presence in the data of small, constant-magnitude fluctuations having fixed locations along the array axis. This spatial stationarity

suggests that these irregularities were associated with particular antenna-receiver channels. The initial RMS amplitude fluctuations due to all causes were of order 10%, or about 1 dB, and the initial RMS phase fluctuations were due to all causes of order 10^{o}. These were about twice the magnitude of the total systematic distortion effects described in Section 2.4.

It is possible to explain the time-varying characteristics of the data at least qualitatively in terms of the small-magnitude, single secondary-signal model of Section 3.5.3. Figure 5.1 shows that at the time "C" the logarithm of the mean echo amplitude lay above a straight line joining the amplitudes observed at the times "A" and "D". If, as appears plausible from Figures 5.4 and 5.5, it can be assumed that until about the time "C", the inequality (3.62) was valid for these data, then eqn. (3.57) suggests that ϕ_d must for at least some of the period between the time "A" and "D" lie in one of the ranges:

$$\left(2n - \frac{1}{2}\right)\pi < \phi_d < \left(2n + \frac{1}{2}\right)\pi, \quad n = 0, \pm 1, \pm 2, \ldots \tag{5.3}$$

Figures 5.2 and 5.3, considered in conjunction with eqns. (3.64) and (3.63), further suggest that since $\partial\phi/\partial r$ showed a slight temporal drift in the positive sense (cf. eqn. (4.1)) and $\partial|E|/\partial r$ showed a significant temporal drift in the negative sense, then additional constraints can be placed on ϕ_d and k_1:

$$\left(2n - \frac{1}{2}\right)\pi < \phi_d < 2n\pi, \quad n = 0, \pm 1, \pm 2, \ldots \tag{5.4}$$

and

2 2

OF/DE

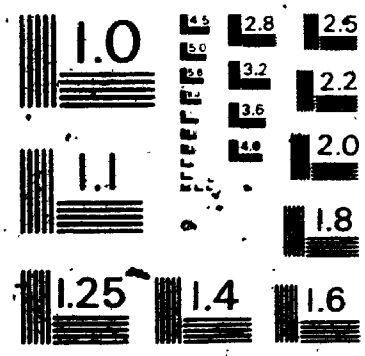

PY RESOLUTION TEST CHART
REAU OF STANDARDS - 1963 - A

ARC - 374

$$k_1 < 0. \qquad (5.5)$$

Moreover, the change in sign from positive to negative of the amplitude slope at the time "B" is consistent with the hypothesis that ϕ_d passed through the value $2n\pi$ at that time. The termination of the positive drift observed in the phase slope between the times "A" and "B" as indicated by the negative drift in the angle of arrival between these times is also consistent with this hypothesis. It can be conjectured that the absence of an immediate tendency for an increasing shift of the angle of arrival could be due to the countervailing effect of a slow increase in the magnitude of either $|k_1|$ or $|E_1/E_o|$ or both; this occurrence would tend also to enhance the rate of increase of negative amplitude slope, as was observed.

At the time "C" and subsequently, Figures 5.3 and 5.4 show the increasing magnitude and decreasing scale size of time-varying quasi-sinusoidal structure in the echo phase and amplitude. This change suggests that the angular separation between the main and secondary echo signals increased and that the constraint imposed by the inequality (3.62) was no longer valid. Therefore the spatial Fourier transforms of the echo signal were investigated to determine if this conjecture had any basis.

5.1.3 Angular Spectra - Echo I

Figure 5.6 shows a contour plot of the spatial Fourier transforms of the smoothed complex data observed across the array, and is based on the same information as contained in Figures 5.1, 5.4 and 5.5. Because the LSBF linear phase slope was subtracted from the data, the centre axis of the contour plot corresponds to the instantaneous angle

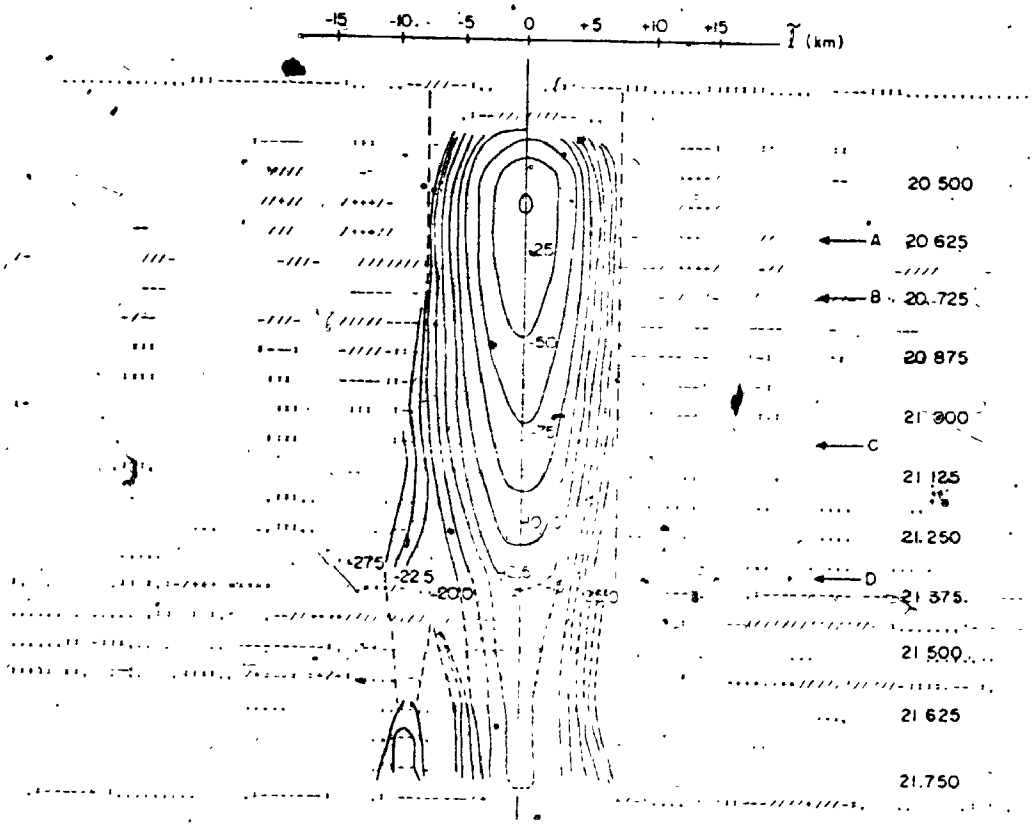

Figure 5.6. Angular spectra - Echo I

of arrival as plotted in Figure 5.2. The contour lines are labelled in decibels relative to 1 volt of receiver output amplitude (dBV) and are plotted at 2.5 dB intervals. Increasing time was plotted downwards along the vertical axis, and the distance $\tilde{\ell}$ (in km) along the trail axis from the instantaneous LSBF phase-slope estimate of the specular reflection point was plotted along the horizontal axis. The parameter $\tilde{\ell}$ was calculated from the equation

$$\tilde{\ell} = [\cos(\underline{k}_{20},\hat{r}) - \cos(\underline{k}_{20},\hat{r})]R_{20}/M(\hat{r}) \qquad (5.6)$$

which can be derived easily from the condition which makes the argument of W in eqn. (3.68) or (3.70) vanish. Again the arrows at the times "A", "B", "C" and "D" correspond to the same times as those in Figures 5.1 through 5.5.

Spatial Fourier transforms of the data were computed using a Dolph-Chebyshev array weighting function to produce expected sidelobe levels of -20 dB, -25 dB and -30 dB below the main signal peak amplitude. For this set of data, the choice of -25 dB sidelobe level offered the optimum compromise between angular resolution and sidelobe level, in that the angular resolution for the -30 dB sidelobe case was sufficiently degraded to partially obscure the observed secondary signal, and the -20 dB sidelobes were judged to be too close in level to the secondary signal.

The computed spectra for the -25 dB sidelobe level case are shown in Figure 5.6. Contours of constant signal level are shown only for signal levels which both exceeded the expected sidelobe level relative to the instantaneous peak signal level by at least 5 dB, and

also exceeded the expected output noise level of -37.6 dBV (Section 4.3.1; Appendix C) by at least 5 dB. These 5 dB margins were adopted in order to ensure that noise and spurious systematic distortion effects would be ignored.

The vertical dashed lines symmetrically spaced on either side of the central axis at distances $\tilde{\ell} = \pm 7.5$ km indicate the theoretically expected location of the first null in the angular response pattern for a single incident plane-wave signal. Possible peaks in the contour plot due to any weaker signals scattered from segments of the trail within axial distances of 7.5 km from the main specular reflection point would be partially to totally obscured, depending on the relative amplitudes of the main and weaker signals, the axial separation between the scattering centres, and the relative phase difference between the two signals.

It can be seen that an asymmetry was present in the observed response pattern. This asymmetry becomes quite pronounced after the time "C", so that just before the echo was obscured by interference at the time "D", the amplitude of the secondary signal was about 1/3 to 1/4 that of the main echo signal, and its angular displacement from the main echo was or order -0.72^{o} (-0.012 radian). This can be translated using eqn. (5.6) into an equivalent displacement of the secondary signal reflection point of -6.5 km along the initial trail axis, or an upward vertical displacement of 2.4 km.

In view of the fact that no sudden temporal discontinuities appeared in these data, it is concluded that the large-scale fluctuations observed in the amplitude and phase across the array earlier in the life of the trail were due to the same cause. The relative motion

of the reflection points of the main and secondary echo signals implies that motion of the trail was involved in the underlying process; the main cause of such motions was likely neutral winds and wind shears.

5.1.4 The Data in Terms of Wind Shears - Echo I

It is interesting and fruitful to speculate on the possible magnitudes and directions of winds and wind shears (or spatial wind gradients) which might lead to the observed phenomena. It was argued in the discussion leading to the derivation of eqn. (3.31) that only distortions of the trail in the "normal" direction can have significant effect in varying the phase path-length between the transmitter and receiver. Equation (3.31) can be recast in the form

$$\tilde{\ell}_s(t) \approx - R_o \left[\frac{1 - (Z_o/R_o)^2}{\cos^2\phi_f \sin^2(\underline{k}_o, \tilde{\ell})} \right] \cos\phi_f \frac{\partial}{\partial \ell} (\underline{\rho}'' \cdot \hat{n}_o)_{\ell=\ell_s} \qquad (5.7)$$

where $\tilde{\ell}_s(t)$ is the observed estimated axial location of a scattering centre and the factor in square brackets is of order unity. For the trail under immediate consideration, eqn. (5.7) can be reduced to

$$\tilde{\ell}_s(t) = -(131 \pm 4) \frac{\partial}{\partial \ell} (\underline{\rho}'' \cdot \hat{n}_o)_{\ell=\ell_s} \qquad (5.8)$$

where all distances are measured in kilometres. Equation (5.8) is the same equation that would result in the case of backscatter geometry ($Z_o = 0$) for an echo observed at a slant range of 131 km. It should also be noted that when eqn. (5.8) is inverted below to estimate $\partial/\partial\ell\ (\underline{\rho}'' \cdot \hat{n}_o)_{\ell=\ell_s}$, the uncertainties in estimating $\tilde{\ell}_s$ are much more significant than the 3% uncertainty in the numerical constant.

In order to see more clearly what was happening to the echo as time progressed, the observed angles of arrival $(\tilde{k}_{20}, \hat{r})$ and the estimated locations of the scattering centres along the trail axis relative to the initial specular reflection point $\ell=0$ have been scaled from the data shown in Figures 5.2 and 5.6 and plotted as a function of time in Figure 5.7. Two additional ordinate scales have also been incorporated in Figure 5.7: $\delta h = -\ell \cos \chi$, which is the vertical displacement of a scattering centre located in the initial trail axis relative to $\ell=0$, and $\partial/\partial\ell(\underline{\rho}'' \cdot \hat{n}_o)$ as derived by inverting eqn. (5.8). This last parameter is the tangent of the small angle through which the trail would have to have been rotated in the $(\hat{n}_o, \hat{\ell})$ plane at the point $\ell=\tilde{\ell}_s$ in order to give rise to a local region of stationary phase.

The steeply sloped thin line at the left side of the plot shows the estimated instantaneous position of the meteoroid as a function of time for an assumed meteoroid speed of 41 km/sec (McKinley, 1961). Its location is based on the assumption that the meteoroid was crossing the principal stationary phase point simultaneously with the observed sharp rise in echo signal level.

The limited resolving power of the array and the unfortunate occurrence of the noise burst permitted only three relatively unobscured observations of the location of the secondary scattering centre. These three observations, however, fall on a sloping straight line in Figure 5.6. From the slope of this straight line can be inferred the spatial gradient of the winds in the $(\hat{n}_o, \hat{\ell})$ plane required to induce the observed apparent motion of the scattering centre. In the present case, the measured slope (taking into account the effect of finite meteoroid velocity) corresponds to a mean gradient in the "normal"

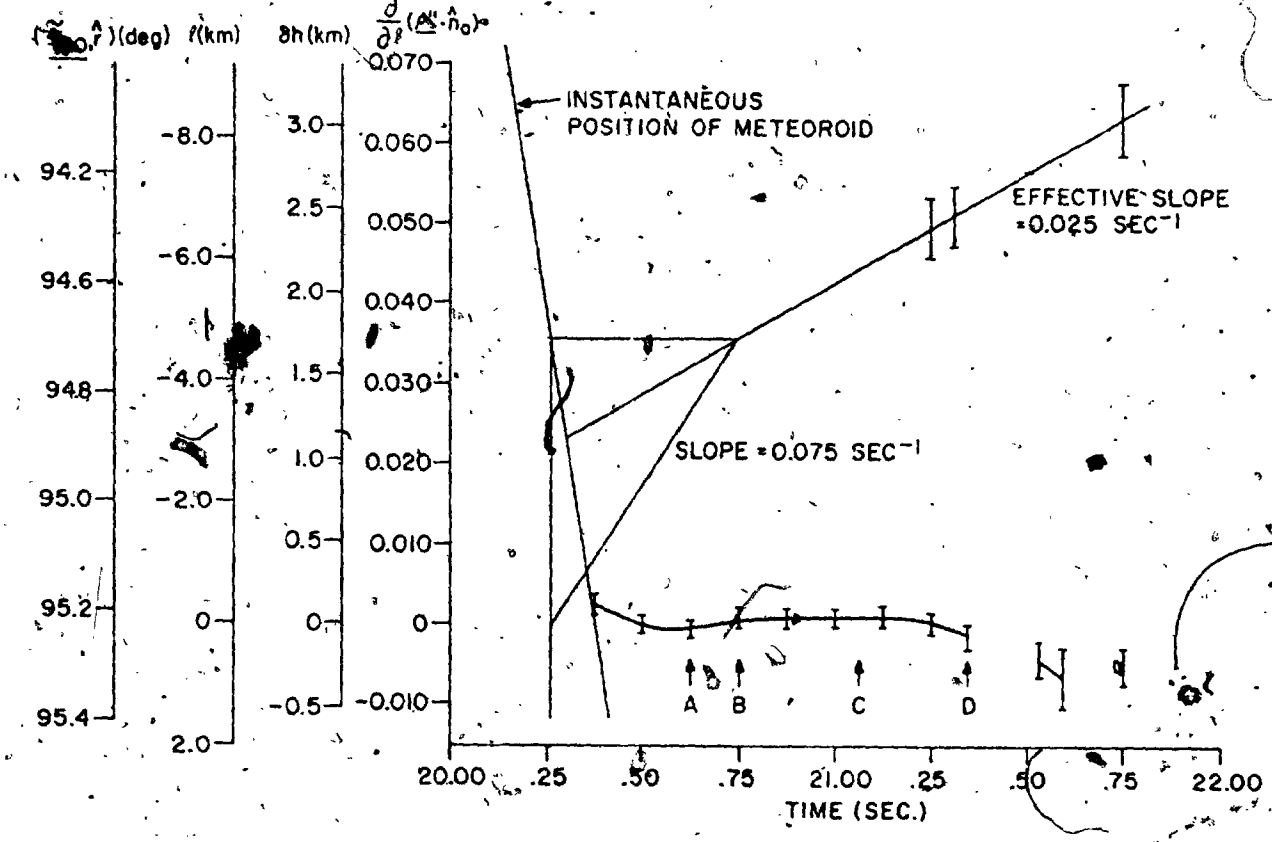

Figure 5.7. Estimated locations of echo scattering centres - Echo I

component of the wind of 25 m/sec per kilometre of displacement along the trail axis, and this gradient extended over an axial distance of at least 1.8 km. If the actual winds are assumed to have been essentially horizontal and uniform over horizontal distances greater than a few tens of kilometres, then the observed slope would correspond to a vertical gradient of the horizontal wind component in the $(\hat{n}_o, \hat{\ell})$ plane of -67 m/sec per kilometre of vertical displacement, extending over a vertical distance of about 660 metres. This would infer a total change in the appropriate horizontal wind velocity component of about -45 m/sec over this height range. Observations of such wind-shear components have been reported previously by Bedinger *et al.* (1968).

There remains a problem with this explanation, however. An extrapolation (which takes account of the finite meteoroid velocity) back to the time of local formation of the trail shows that there remained an unaccounted rotation of the trail of at least 1.1° from its assumed initial orientation. This rotation could be accounted for in two ways. One way would be that the gradient increased with decreasing height to a maximum at some height between that of the main and secondary echoes. The maximum local gradient can be estimated by extrapolating back to the time of first observation of the effect of the assumed second stationary phase point and then estimating the gradient by calculating the ratio of the required angular rotation and the time within which it must have taken place. The earliest signs of the presence of a secondary echo component occurred at the time "B". In this case, an angular rotation of the trail of 2.1° would had to have occurred in a time of 0.48 seconds, implying a wind shear in the $\hat{n}_o$ direction of 0.075 sec^{-1} or 75 m/sec per kilometre of axial distance.

Such a shear would correspond to a vertical gradient in the horizontal wind of -200 m/sec per kilometre of vertical displacement. The lack of any previous reports of such magnitude of wind shear casts doubts on the reality of such an occurrence here. The other hypothesis, that the meteoroid fragmented and produced multiple trails, will be developed below.

5.1.5 The Data in Terms of Meteoroid Fragmentation - Echo I

An alternative hypothesis to that of the preceding section is that of the near-simultaneous occurrence of multiple trails, perhaps due to the fragmentation of a single initial meteoroid, or perhaps due to the chance passage of more than one meteoroid. In either case, however, there is an additional degree of freedom which must be considered. Specifically, an echo observed at an angle of arrival $(\underline{k}_{20}, \hat{r})$ could have been caused either by a trail which was lying in the $(\hat{n}_o, \hat{\ell})$ plane of the main echo trail and which underwent a component of rotation in that plane, or by a trail at a different location in the sky corresponding to approximately the same path range and which had not been rotated, i.e., was parallel to the main trail, or by some combination of these two cases. The two extreme cases will be examined below.

In the case that the secondary echo trail is assumed to have formed initially in the $(\hat{n}_o, \hat{\ell})$ plane of the main echo trail, then the following analysis is applicable. If the meteoroid broke apart in such a way that a substantial fragment of it passed the point $\ell = -4.7$ km simultaneously with the fragment which caused the main echo signal, and with an angle of divergence of about 1.4^o from the trajectory of the main echo fragment as measured in the $(\hat{n}_o, \hat{\ell})$ plane, then the inferred

vertical shear of the horizontal wind of -67 m/sec/km acting for the 0.48 sec which elapsed before the secondary echo was observed would be sufficient to account for the necessary 0.7° of rotation required to bring the fragment trail into a suitable orientation. The lack of echoes from such a fragment trail earlier in the data (i.e., from lower heights) could be explained on the basis that either the fragment burned out between ℓ = -4.7 km and ℓ = 0, or the wind shear changed between these two points. The latter possibility is also supported by the relatively small shift observed in the reflection point of the main echo component, which would imply the presence there of only a very small component of wind shear.

As a check on whether or not the secondary echo was in fact associated with the same meteoroid as the main echo, the relative rates of amplitude decay between the main echo and the secondary echo can be compared. Since the secondary echo apparently corresponded to a greater height than the main echo, it would be expected to have shown a faster decay rate than the main echo. Therefore the ratios of the amplitudes were compared for that portion of the echo history when the secondary echo was spatially resolved from the main echo and uncontaminated estimates of the component amplitudes could be made.

It is a straightforward matter to show from eqns. (3.76) and (5.2) that the theoretical time variation of the difference in decibels between the main and secondary echo amplitudes when both echo components are due to initially uniform infinite-length underdense trails is given by

$$\rho_A(\text{dB}) \doteq -20 \log_{10}[\exp(1)] \times \left[\frac{4\pi}{\lambda \sec \phi_f}\right]^2 \times 5.8 \exp\left[\frac{h_o - 95}{6.5}\right]$$

$$\times [t_o - t_s \exp(-\tilde{\ell}_s \cos \chi / 6.5)] + \rho_{AO}$$

or

$$\rho_A(\text{dB}) = \frac{7.96 \times 10^3}{[\lambda \sec \phi_f]^2} \exp\left[\frac{h_o - 95}{6.5}\right]$$

$$\times [t_o - t_s \exp(-\tilde{\ell}_s \cos \chi / 6.5)] + \rho_{AO} \qquad (5.9)$$

where λ is the radio wavelength (in metres), ϕ_f is the forward scattering angle, h_o is the estimated height of reflection of the main echo (in kilometres), $-\tilde{\ell}_s \cos \chi$ is the estimated difference in reflection height between the main and secondary echo signals (in kilometres), t_o and t_s are the elapsed times (in seconds) since the time of local formation of the trail components, and the constant ρ_{AO} is a measure (in decibels) of the ratio of the product of the unknown initial reflection coefficients and effective lengths of the trail segments contributing to the two echo components.

For the present case eqn. (5.9) reduces to

$$\rho_A(\text{dB}) = -3.3 \times [t_o - t_s \exp(-\tilde{\ell}_s \cos \chi / 6.5] + \rho_{AO} \qquad (5.10)$$

Table 5.2 shows the results of comparing the theoretical values of ρ_A calculated using eqn. (5.10) with an assumed value for ρ_{AO} of zero and those values of ρ_A scaled from the data from which Figure 5.6 was plotted. The column labelled "Difference" shows the difference in decibels between the theoretical and experimentally measured values.

TABLE 5.2

Comparison of Theoretical and Observed Amplitude Ratios for Echo I

t_o (sec)	t_s (sec)	$-\tilde{\ell}_s \cos \chi$ (km)	ρ_A (dB) THEORY	ρ_A (dB) OBSERVED	DIFFERENCE (dB)
0.875	1.025	2.4	2.0	12.6	-10.6
0.938	1.100	2.55	2.3	11.2	- 8.9
1.375	1.570	3.3	4.1	12.6	- 8.5

For initially uniform and infinite trail segments, this difference would remain constant and be a measure of the ratio of the initial reflection coefficients only; the fact that this difference decreased with time indicates that the observed relative strength of the secondary echo was increasing with time with respect to that predicted by the theoretical model. This discrepancy is consistent with the assertions above that either the meteor fragment responsible for the secondary echo burned out above $\ell=0$ or that there was a change with height of the wind shear between ℓ = 4.7 km and $\ell=0$.

Chemiluminescent rocket trail observations at heights between 80 km and 120 km have shown the frequent occurrence of regions of uniform wind shear, separated by thin regions where there exist very abrupt changes of vertical gradients of the horizontal winds. These changes have been reported to occur within vertical distances of less than 100 m (Bedinger *et al.*, 1968). Such observations are consistent with the results reported above, as well as those of Section 5.3.4.

It can be assumed instead that the secondary echo trail was formed parallel to the main echo trail at an initial angle of arrival of 94.9°, as might be inferred from Figure 5.7, and that the path range $2R_o$ was 948 km. A numerical analysis of the geometry showed that the apparent height of reflection would have been about 200 m lower than that of the main echo, and the reflection point would have been about 24 km closer to the transmitter.

An examination of the geometric parameters for estimated initial angles of arrival between 94.9° and 95.18° showed that the calculated height of reflection remained very close to 106 km and the apparent horizontal displacement decreased as the assumed initial deviation in

the angle of arrival was decreased, as would be expected intuitively. Further examination of the geometry showed that, if it were assumed that the secondary echo trail lay initially exactly parallel to the main echo trail but at a slightly greater height (e.g., 108 km) and hence slightly greater range (e.g., 949 km) than the main echo trail, then the horizontal separation between the trail axes would have been of order 8 km for an assumed initial angle of arrival of 95.18° and of order 24 km for an assumed initial angle of arrival of 94.9°.

It thus becomes obvious that for reasonable alternative choices of geometric parameters, it is necessary to conclude that either two independent meteoric fragments generated trails parallel to each other within a few kilometres to a few tens of kilometres of horizontal separation and of order one to two kilometres of vertical separation, or that two major fragments of a single parent meteoroid, diverging by about 1.3° in the $(\hat{n}_o, \hat{\ell})$ plane must have occurred. However, the self-consistency of the analysis based on the model of diverging fragments from a common parent lends support to that model.

A final analysis will be based on the assumption that indeed the two trail components were due to fragments from a common parent. It can be assumed that the initial rotation of the secondary echo trail in the $(\hat{n}_o, \hat{\ell})$ plane was equal to $\delta\chi$, the angle of divergence of the two particles in that plane. Then the approximate relation

$$\delta\chi \approx \frac{\partial}{\partial \ell} (\underline{\rho}'' \cdot \hat{n}_o)_{t=0} \qquad (5.11)$$

is valid for small values of $\delta\chi$ and at the time $t=0$ that the secondary echo trail was formed. The parameter $\delta\chi$ can be estimated by extra-

polating the estimated rate of trail rotation back to the time of local meteoroid passage, as was shown earlier.

It is shown in Appendix D that if $\delta\chi$, the angle of trail divergence, and δh, the initial difference in height between the main and secondary echo reflection points, are known or can be estimated, then Δh, the difference in height above the main trail initial specular reflection point at which the parent meteoroid fragmented, is given to good approximation by

$$\Delta h = \frac{\delta h + \tilde{\ell}_m \cos \chi}{\delta\chi \tan \chi} - \tilde{\ell}_m \cos \chi \qquad (5.12)$$

where here $\tilde{\ell}_m$ is the minimum value for $\tilde{\ell}_s$ observed over the lifetime of the secondary echo. If it is assumed that to a first approximation the quantities $\tilde{\ell}_m \cos \chi = -3.0$ km and $\delta\chi = 0.023$ radian, as scaled from Figure 5.6, then eqn. (5.12) becomes

$$\Delta h = 17.2 (\delta h - 3.0) + 3.0 \qquad (5.13)$$

Since the secondary echo was observed at heights at least 3.0 km above the main specular reflection point, then the point of fragmentation of the parent meteoroid must have occurred at some even greater height. If it is assumed that the secondary echo trail extended one complete Fresnel zone radius aboye the observed maximum estimated secondary echo height, then the incremental height of fragmentation Δh must have been at least 3.8 km. This corresponds to an actual height of fragmentation of about 110 km.

For a value of 3.8 km for Δh, eqn. (5.13) yields a value for δh of about 3.05 km, or about 50 m above the simple geometric estimate

$\tilde{\ell}_m \cos \chi$ of 3.0 km. Such a small incremental height difference is not directly observable by the present system, and the observation time was too short to permit an indirect height difference estimate based on decay time measurements. If instead a value for Δh of 10 km is assumed, corresponding to fragmentation at a height of 116 km, then eqn. (5.13) yields a value δh = 3.4 km, or about 400 m above the simple geometric estimate. Even this order of height difference is not observable, since as can be inferred from Table 5.1 it would correspond to a difference in echo path range of about only 0.3 km relative to the main echo path range.

In summary, the behavior of this echo indicated the presence of two separate meteor trails, which could well have been produced by the fragmentation of a single meteoroid at heights above which the echoes were observed. It also appeared that the presence of significant, height-varying shears of the horizontal winds were necessary to explain the observed angular behavior of this echo.

5.2 Echo II - A Smooth Transitional Echo

The second echo to be investigated was an almost-underdense transitional echo observed starting at 16:40:24.750 EST on 3 January 1973. The pertinent geometric parameters of this echo, referred to below as Echo II, have also been summarized in Table 5.1.

5.2.1 Spatially Averaged Parameters - Echo II

Figure 5.8 shows the temporal behavior of the absolute amplitude of Echo II, averaged across the array. The initial rise in amplitude as the meteor trail was formed and as limited by the 1/16th second time

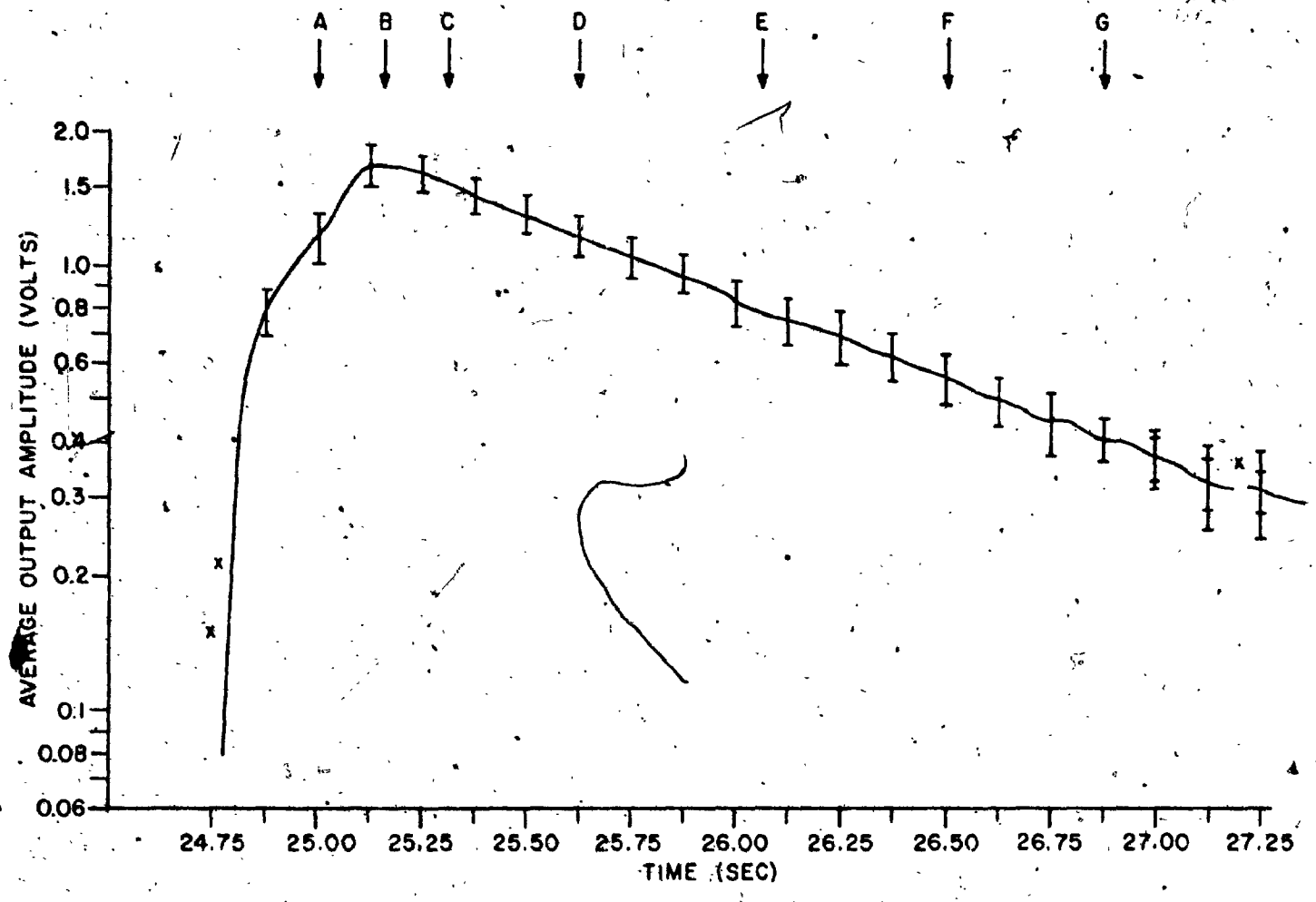

Figure 5.8. Spatially averaged amplitude -- Echo II

constant of the digital integrator (Section 4.3.1) was essentially complete by the time "A". The echo amplitude continued to rise for a further 0.16 second in the manner characteristic of a transitional echo, but the short duration of this part of the echo life and the apparent linearity of the temporal decay of the logarithm of the echo amplitude indicate that the trail was almost underdense.

After the time "B", the echo amplitude decayed exponentially with a time constant of 1.18 seconds, and showed only minor amplitude fluctuations until finally the echo was lost in noise. From eqn. (3.76), the value estimated for the ambipolar diffusion coefficient D was 10.2 m^2/sec, and from eqn. (5.2) the inferred height of reflection was 99 ($\pm$5) km, again in reasonable agreement with the direct geometric estimate of 101 ($\pm$3) km (Table 5.1).

Figure 5.9 shows that for the first 0.6 seconds of the life of the echo, to the time "C", no significant change occurred in the angle of arrival as estimated from the LSBF linear phase slope across the array. Beginning from the time "C", for the next 1.4 seconds, to the time "F", a slow increase of 0.07° occurred. This would correspond to a downward axial shift of the specular reflection point of 0.8 km, or a downward shift in height of about 0.3 km. For the final 0.8 seconds of the echo life, from the time "F", the estimated standard deviation of the angle of arrival increased as the echo continued to decay. This was a manifestation of the increasing RMS deviation of the phase about the LSBF lines.

Figure 5.10 shows the presence of a small initial positive fractional amplitude variation across the array. The magnitude of this variation increased to a local maximum at the time "A", and then de-

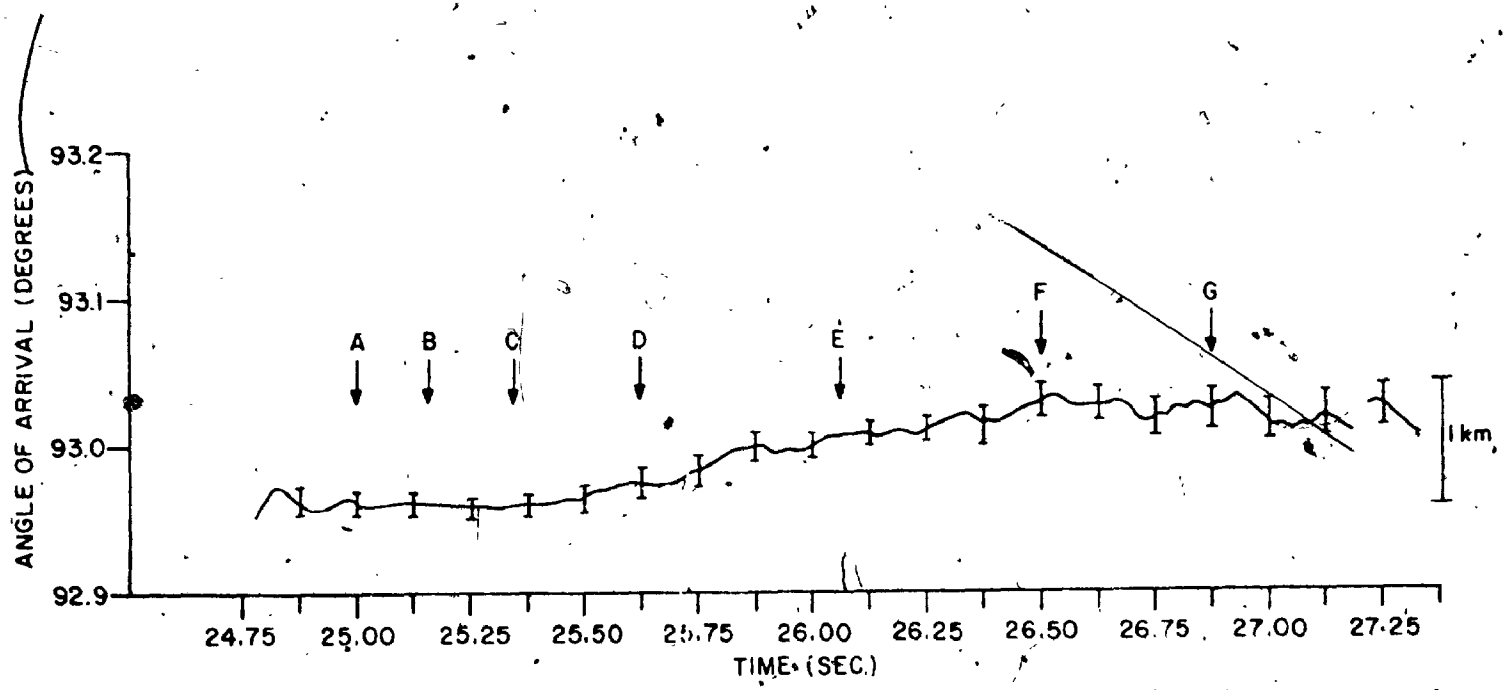

Figure 5.9. Angle of arrival from LSBF phase slope - Echo II

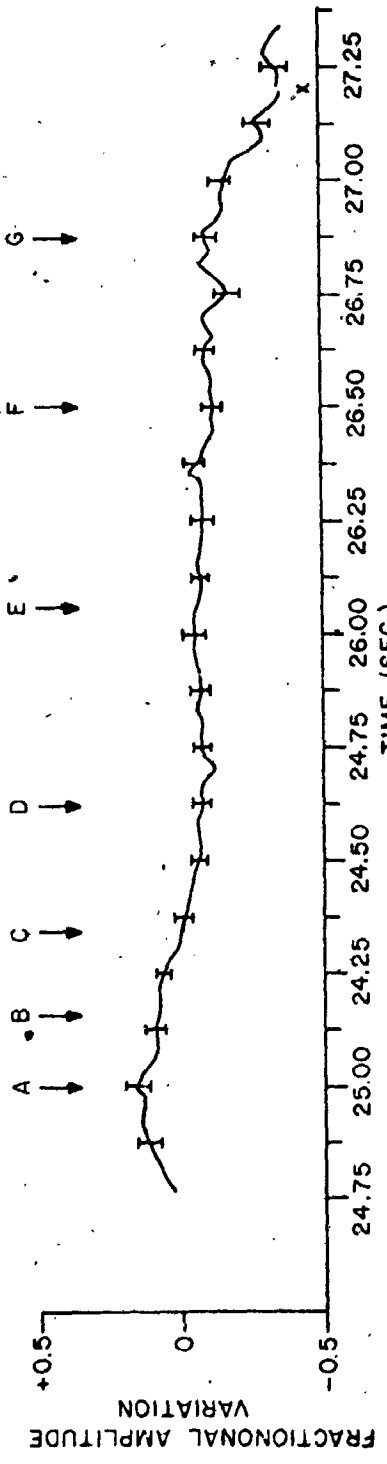

Figure 5.10. Fractional amplitude variation - Echo II

creased to zero about 0.28 seconds later at the time "C". A small almost constant negative slope then appeared, which after a further 1.6 seconds, at the time "G", began to increase in magnitude.

It might again be supposed that the correlation between the change in sign of the fractional amplitude variation and the beginning of the change in angle of arrival at the time "C" could be explained on the basis of the small-magnitude secondary signal model (cf. Section 5.1.1). The relative amplitude and angular separation of the secondary signal with respect to the main echo were apparently small for most of the life of the echo, as attested to by the relatively small estimated standard deviations for the LSBF angle of arrival and fractional amplitude deviation estimates. Any assumption that the difference in angle of arrival between the main and secondary echoes was small, however, was not supported by the more detailed analyses below.

5.2.2 Spatial Phase and Amplitude Observations - Echo II

Figures 5.11 a-c and Figures 5.12 a-c, which show respectively the phase and normalized amplitude observed across the array, reveal near the time "D" the occurrence of small-magnitude fluctuations with scale size significantly less than the length of the array. The amplitude fluctuations show the effect of systematic distortions, but the phase fluctuations, although of small magnitude, are clearly visible. After the time "F", larger magnitude fluctuations appear in both the normalized amplitude and the phase plots; the scale size of these fluctuations was again substantially less than the length of the array.

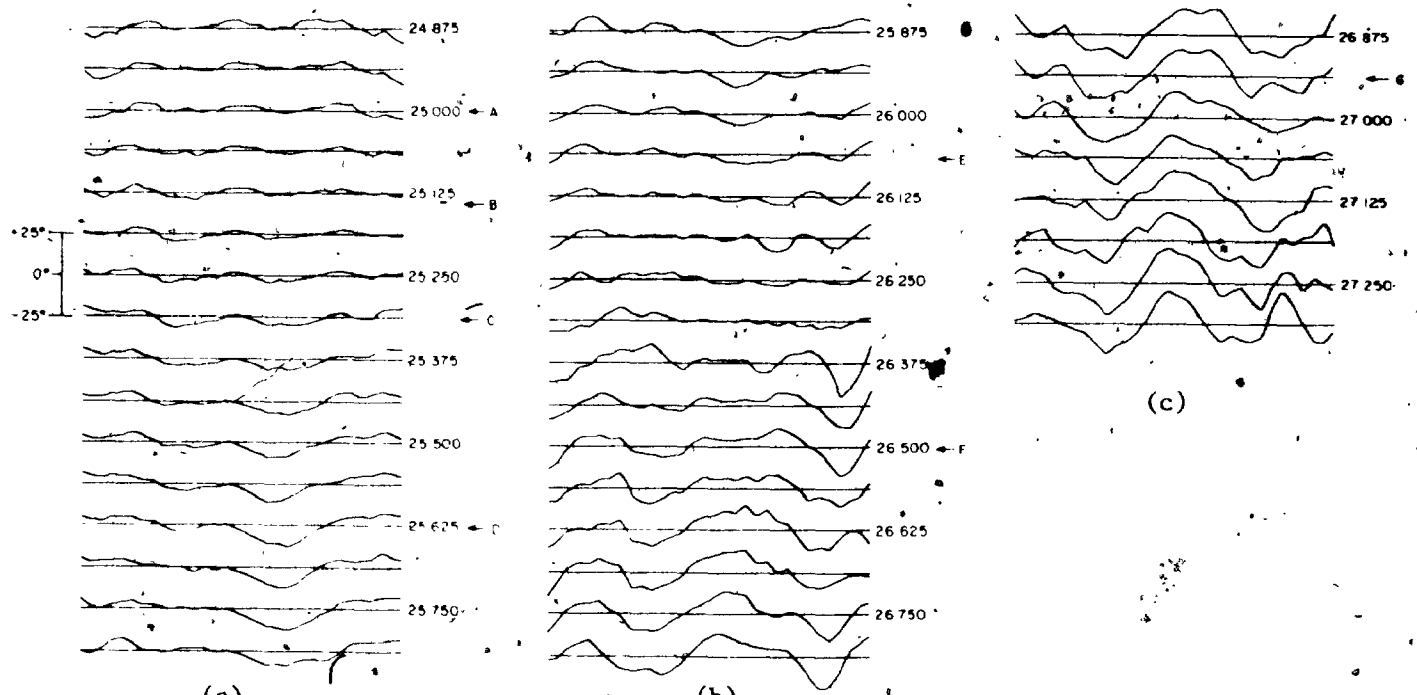

Figure 5.11. Spatial phase fluctuations - Echo II

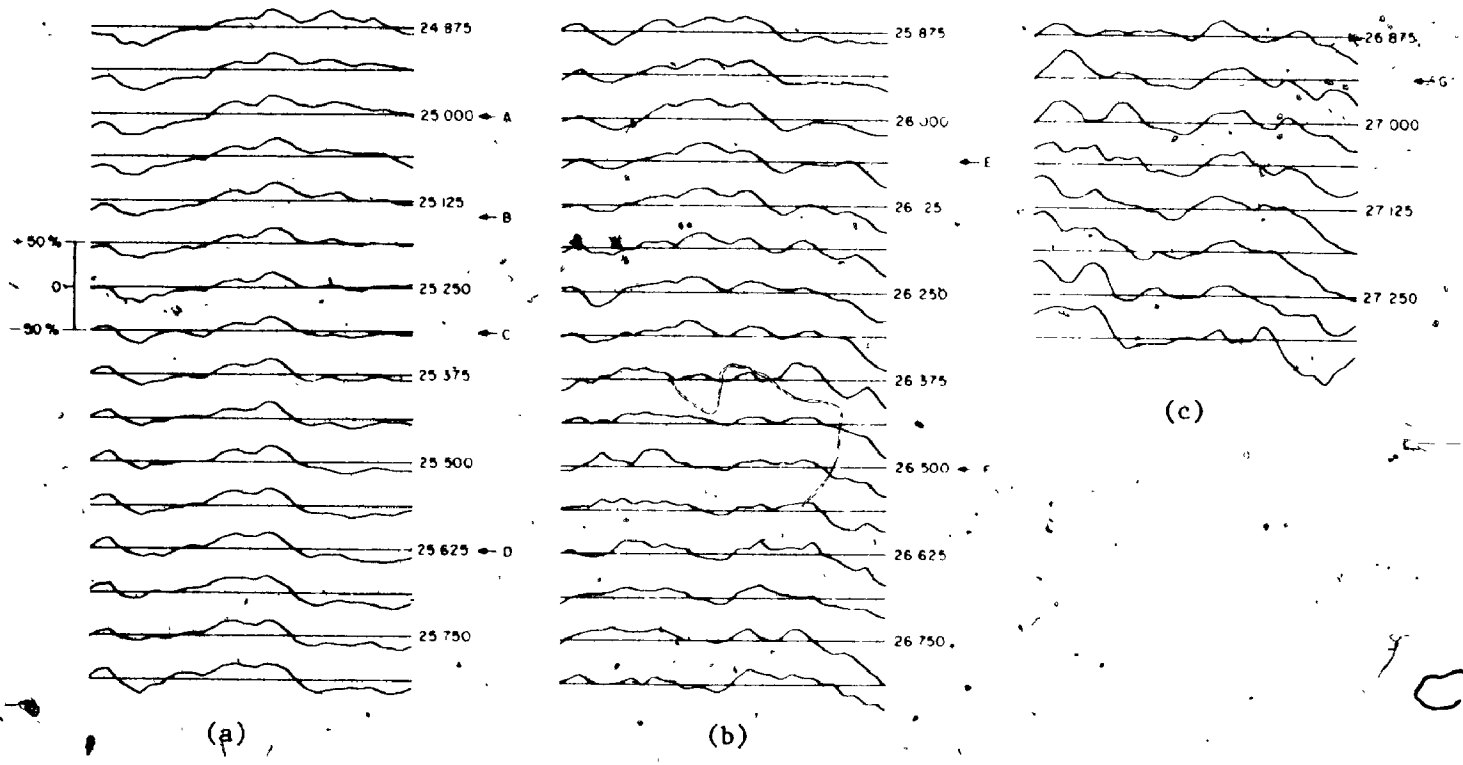

Figure 5.12. Spatial amplitude fluctuations - Echo II

ion of the secondary trail was not grossly different from that of the main trail, so that eqn. (5.14) is valid, a wind-shear component in the "normal" direction of 18 m/sec per kilometre of axial displacement can be scaled from Figure 5.14. This would correspond to a vertical shear of the horizontal wind component in the $(\hat{n}_o, \hat{\ell})$ plane of -52 m/sec per kilometre of vertical displacement, over a height increment of about 1.5 km. The cause of the sudden reversal in the direction of motion of the secondary echo scattering centre near the end of its life is not explainable in terms of this simple model; it could, however, be associated with the dissipation of the upper part of the trail.

Again it is evident that the wind shear was different over differing height ranges, as evidenced by the mean wind shear of -1.3 m/sec per kilometre of axial displacement as deduced from the mean motion of the main specular reflection point. This would correspond to a vertical shear of the horizontal wind component in the $(\hat{n}_o, \hat{\ell})$ plane of 3.7 m/sec per kilometre of vertical displacement.

Analysis of the secondary echo amplitude data from this example might not be expected to have been as consistent as in the previous case, where there appeared to be good reasons to assume some quite direct relation between the secondary echo and the main echo. For the present case, eqn. (5.10) becomes

$$\rho_A(\text{dB}) = -10.5 \times [t_o - t_s \exp(-\hat{\ell}_s \cos \chi / 6.5)] + \rho_{AO} \qquad (5.15)$$

and in the absence of any better information, it was assumed that $t_o = t_s$ and $\rho_{AO} = 0$ for purposes of calculating ρ_A (Theory) in Table 5.3. The "Difference" column of that table shows a reasonable consistency

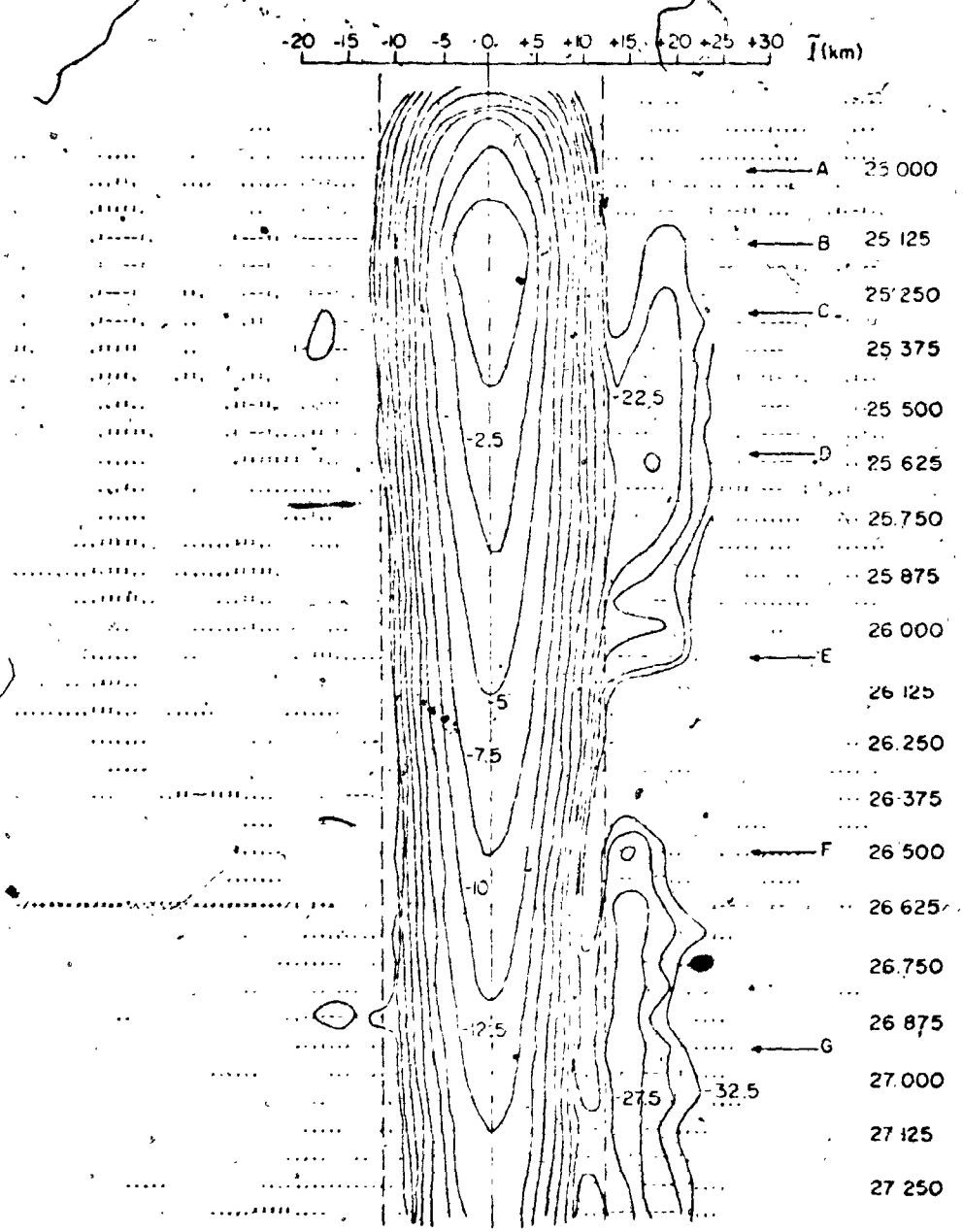

Figure 5.13. Angular spectra - Echo II

the increase in the negative slope of the absolute amplitude across the array, is consistent with the incipient formation of another scattering centre close to and slightly above the main specular reflection point. It is not likely that this effect was due to the resolved secondary signal introducing an odd half-integral number of cycles of amplitude fluctuation across the array, since the angular separation of this signal from the main echo corresponded to about two cycles of amplitude or phase fluctuations across the array. Furthermore, the F-ratio of the RMS scatter of the absolute amplitude about its mean value relative to the RMS scatter about the LSBF line increased from 1.4 to about 4.0. This is indicative that the spatial amplitude slope was highly significant (less than 0.5% chance of random occurrence). The effect is also clear in Figure 5.8, where after the time "F" error bars for both the estimated standard deviation of the amplitude about the mean (longer bars) and the RMS deviation about the LSBF linear variation across the array (shorter bars) are plotted. It can readily be seen that the amplitude scatter about the LSBF straight line is much smaller than the scatter about the mean.

5.2.4 The Data in Terms of Wind Shears - Echo II

This trail has also been subjected to the same analyses as the previous example (Section 5.1.4). The locations of the observed scattering centres have been plotted in Figure 5.14; note the discontinuity in the vertical scales of that figure.

The most noteworthy features of that figure are that the secondary echo became visible before the expected time of local passage of the main meteoroid, and the large angular divergence between the

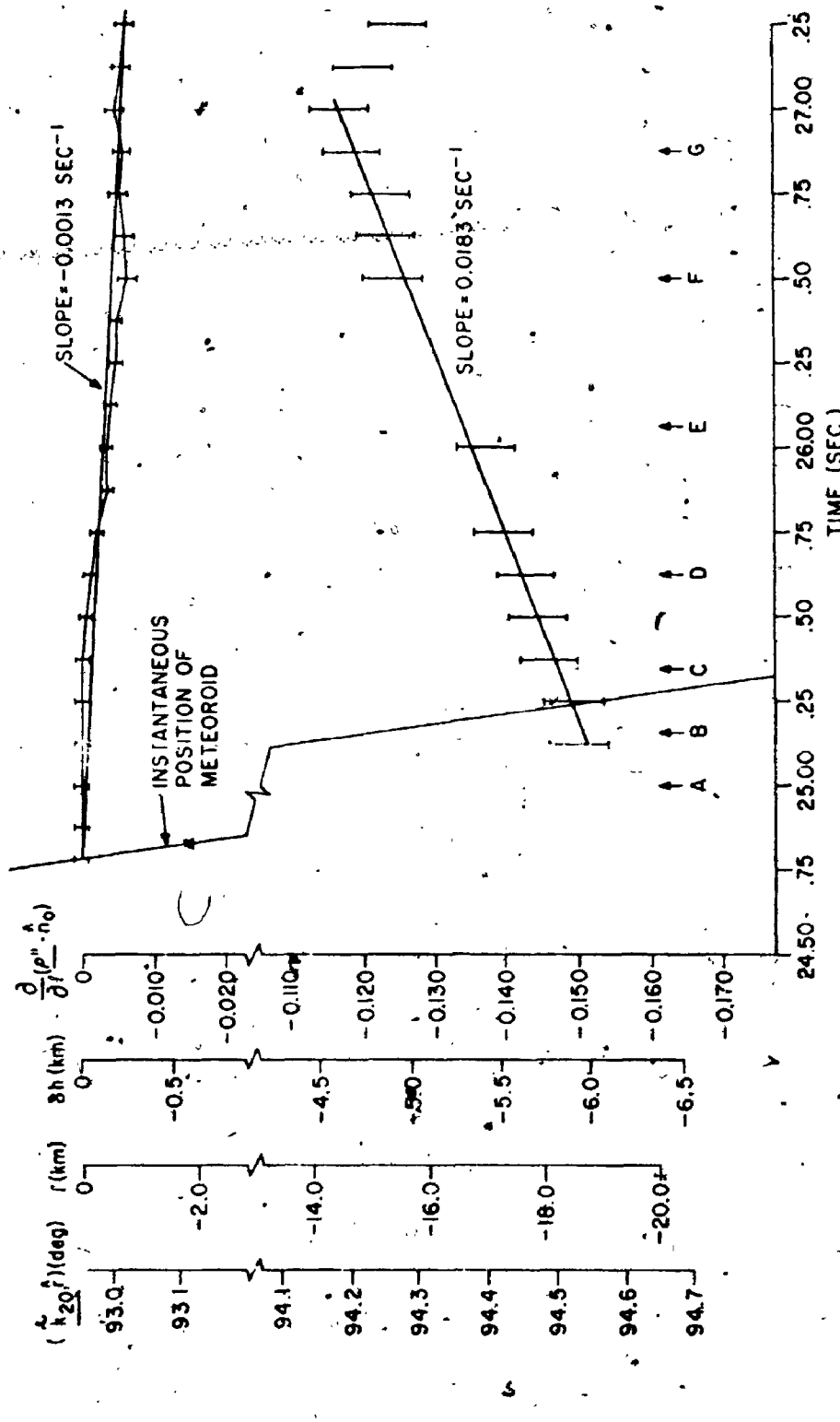

Figure 5.14. Estimated locations of echo scattering centres - Echo II

path of the main meteoroid and the required orientation of the axis of the secondary scatterer in the $(\hat{n}_o, \hat{\ell})$ plane. For the present case eqn. (5.7) becomes:

$$\tilde{\ell}_s(t) = -(124 \pm 4) \frac{\partial}{\partial \ell} (\underline{\rho}'' \cdot \hat{n}_o)_{\ell=\ell_s} \qquad (5.14)$$

so that the appearance of a secondary reflection at $\tilde{\ell}_s = 18.6$ km would correspond to a rotation from the trail axis in the $(\hat{n}_o, \hat{\ell})$ plane of 8.5^o. Thus it is concluded that the main specular reflection and the secondary reflection were not due to the passage of a single meteoric particle.

5.2.5 The Data in Terms of Meteoroid Fragmentation — Echo II

In spite of the fluctuations in the amplitude of the secondary echo, the bulk of the observations of its location fell on a straight line. A possible explanation for the occurrence of this secondary echo is that an irregular trail was formed by the passage of a small meteoroid about 1/4 second before the local passage of the meteoroid which caused the main echo, and this irregular trail was then rotated by a uniform wind shear. Such a small meteoroid might or might not have been associated with the main echo meteoroid, although a temporal separation of 1/4 second would imply a spatial separation in the axial direction of order 10 km, so that such association seems unlikely.

The major restriction on the location of the secondary echo trail is that its echo range offset frequency be within ± 2-3 Hz of that of the main echo, so that its amplitude would not be attenuated by the digital integrators (Section 4.3.1). On the assumption that the locat-

ion of the secondary trail was not grossly different from that of the main trail, so that eqn. (5.14) is valid, a wind-shear component in the "normal" direction of 18 m/sec per kilometre of axial displacement can be scaled from Figure 5.14. This would correspond to a vertical shear of the horizontal wind component in the $(\hat{n}_o, \hat{\ell})$ plane of -52 m/sec per kilometre of vertical displacement, over a height increment of about 1.5 km. The cause of the sudden reversal in the direction of motion of the secondary echo scattering centre near the end of its life is not explainable in terms of this simple model; it could, however, be associated with the dissipation of the upper part of the trail.

Again it is evident that the wind shear was different over differing height ranges, as evidenced by the mean wind shear of -1.3 m/sec per kilometre of axial displacement as deduced from the mean motion of the main specular reflection point. This would correspond to a vertical shear of the horizontal wind component in the $(\hat{n}_o, \hat{\ell})$ plane of 3.7 m/sec per kilometre of vertical displacement.

Analysis of the secondary echo amplitude data from this example might not be expected to have been as consistent as in the previous case, where there appeared to be good reasons to assume some quite direct relation between the secondary echo and the main echo. For the present case, eqn. (5.10) becomes

$$\rho_A(\text{dB}) = -10.5 \times [t_o - t_s \exp(-\hat{\ell}_s \cos \chi / 6.5)] + \rho_{AO} \qquad (5.15)$$

and in the absence of any better information, it was assumed that $t_o = t_s$ and $\rho_{AO} = 0$ for purposes of calculating ρ_A (Theory) in Table 5.3. The "Difference" column of that table shows a reasonable consistency

TABLE 5.3

Comparison of Theoretical and Observed Amplitude Ratios for Echo LI

t_o (sec)	t_s (sec)	$-\tilde{\ell}_s \cos \chi$ (km)	ρ_A (dB) THEORY	ρ_A (dB) OBSERVED	DIFFERENCE (dB)
0.344	0.344	-6.0	- 2.2	28.6	-30.8
0.469	0.469	-5.9	- 2.9	26.4	-29.3
0.594	0.594	-5.8	- 3.7	24.1	-27.8
0.714	0.719	-5.7	- 4.4	22.8	-27.2
0.844	0.844	-5.6	- 5.1	21.5	-26.6
0.969	0.969	-5.5	- 5.8	21.2	-27.0
1.219	1.219	-5.4	- 7.2	23.1	-30.3
1.719	1.719	-4.9	- 9.6	20.0	-24.6
1.844	1.844	-4.9	-10.2	17.5	-27.7
1.969	1.969	-4.8	-10.9	17.3	-28.2
2.094	2.094	-4.7	-11.3	16.8	-28.1
2.219	2.219	-4.6	-11.9	15.3	-27.2
2.344	2.344	-4.8	-12.8	14.3	-27.1
2.469	2.469	-5.0	-13.8	14.6	-28.4

between the amplitude ratios predicted by the simple model and those calculated directly from the data. During the period of about 2 seconds when both echo components were observable, the theoretically predicted change in the amplitude ratio was about 11.6 dB, with the amplitude of the secondary echo increasing relative to that of the main echo. The observed ratio of the main to secondary echo amplitude followed this trend, so that the average difference between the theoretical and observed amplitude ratios implied a value for ρ_{AO} of 28.2 $\pm$1.3 dB. Equation (3.75) would then suggest an effective line density for the secondary echo trail of order 4% of that of the main-echo trail.

The disappearance of the secondary echo between the times "E" and "F" could be due to a gross irregularity of the secondary-echo trail line density. On the assumption that the trail was being rotated by a uniform wind shear, the length of trail from which no echo was being received would be (from Figure 5.14) of order 1.6 km. This compares favorably with the effective reflecting length $|L_o|$ of an undistorted trail of 1.7 km, as calculated from eqn. (3.37), and which is thus the length of trail which would have to be non-reflective in order to result in a significant suppression of echo signal strength.

Numerical analyses of the secondary echo scattering geometry were performed using the geometric model of Chapter 3. The assumption that the secondary echo trail were initially parallel to the main echo trail and had the same echo range $2R_o$ of 948 km required that such a trail be located about 180 km closer to the receiver array and also be about 7 km higher than the main echo trail. The observed behavior of the amplitude ratio ρ_A was completely inconsistent with the hypothesis of a secondary trail at that height. An attempt to rationalize this

height discrepancy by reducing the estimated echo range required a reduction of the range or order 6 to 9 km (2 to 3 Hz in range offset frequency), and this reduction also implied an additional 50 km horizontal separation between the estimated reflection points. The only logical conclusion would be that if two meteoroids were travelling parallel paths, they must have been quite independent.

If the fragmenting meteoroid model was appropriate, then $\delta\chi = -0.15$ radian and $\tilde{\ell}_m \cos\chi = 4.6$ km, and eqn. (5.12) becomes

$$\Delta h = -2.24\ (\delta h + 4.6) - 4.6 \qquad (5.16)$$

This result implies that for $\Delta h > \delta h$, as required for the fragmentation hypothesis to have been valid, then it must have been that $\delta h < -4.6$ km. This means that the secondary trail must have been situated at or below the height given by the simple geometric estimate $-\tilde{\ell}_s \cos\chi$.

The simple geometric estimate of the height range over which the secondary echo trail was visible implies that $\Delta h > -4$ km and that fragmentation must have occurred above a height of 97 km. Equation (5.16) also suggests that if fragmentation occurred at a height of 105 km, then the actual height of the secondary echo trail would have been about 3.8 km below the simple geometric estimate. This is inconsistent with the amplitude data.

However, Figure 5.14 shows that the secondary echo meteoroid passed $\tilde{\ell}_s = -18.6$ km at least 100 msec before the main echo meteoroid. This would imply that at a speed of 41 km/sec, the path traversed by the secondary echo meteoroid must have been about 4 km shorter than that traversed by the main echo meteoroid. It can be shown from Figure D.1 that the expression for this path difference is given by

$$\Delta\ell = (\Delta h \sec \chi - \ell)(1 - \cos \delta\chi) \qquad (5.17)$$

By substituting $\Delta\ell$ = 4 km into eqn. (5.17) and solving for Δh, a value for Δh of 120 km can be obtained. This settles at last the question of whether the secondary echo was directly associated with the main echo: it was not.

In summary, while there is overwhelming evidence that the main and secondary echoes were due to the passage of two independent meteoric particles, there is an underlying consistency in the amplitude and angle-of-arrival data which suggests that the wind-shear observations were valid.

5.3 Echo III - A Fluctuating Transitional Echo

The third and final echo to be investigated was a transitional echo observed starting at 15:51:17.125 EST on 3 January 1973. This echo, which displayed minor fluctuations in its amplitude behavior, was certainly the most complex of the three analyzed echoes. The pertinent geometric parameters have again been summarized in Table 5.1.

5.3.1 Spatially Averaged Parameters - Echo III

Figure 5.15 shows the temporal behavior of the absolute amplitude of the echo averaged across the array. The initial rise in echo amplitude as the meteor trail was formed, as limited by the 1/16th second time constant of the digital integrator, was certainly complete by the time "A" (3/16 or 0.19 seconds after the start of the initial rise in amplitude). However, the echo amplitude continued to increase in a fluctuating but essentially linear manner for another 0.30 seconds to the time "C", and then the rate of increase became progressively

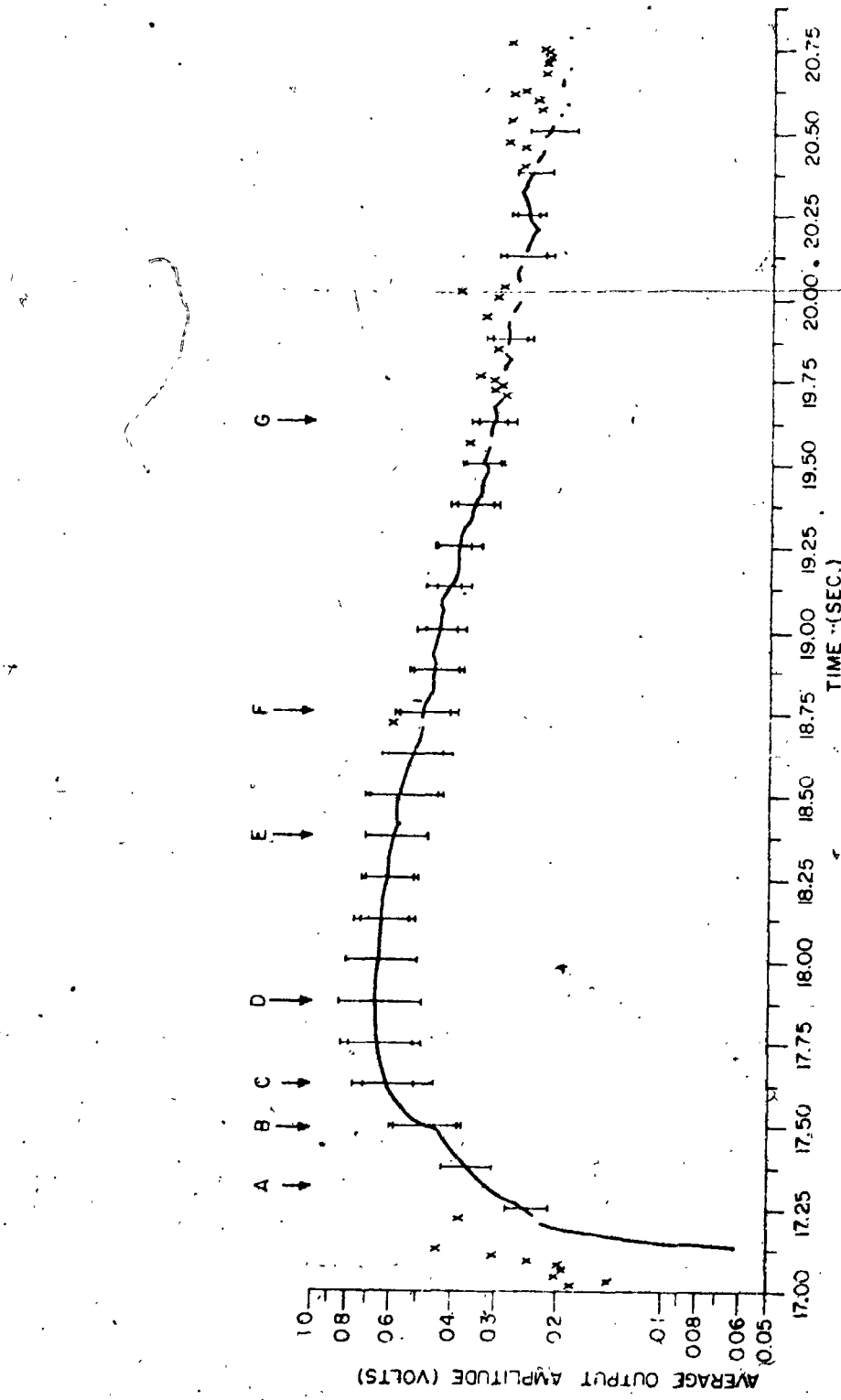

Figure 5.15. Spatially averaged amplitude - Echo III

smaller. The echo amplitude reached its ultimate maximum after the passage of another 0.25 seconds, at the time "D", and then it decreased until the echo signal was finally lost in noise and interference about 2.6 seconds later. The decay time constant of 2.0 seconds scaled from Figure 5.15 between the times "E" and "G" implies from eqn. (3.76) an ambipolar diffusion coefficient of 5.2 m^2/sec and hence from eqn. (5.2) an apparent reflection height of 94 ($\pm$5) km. This result is in somewhat poorer agreement with the geometric estimate of reflection height of 100 ($\pm$5) km than were the corresponding sets of estimates for the two previous examples, but this discrepancy is characteristic of the trend which would be expected for a transitional trail with somewhat greater line density than that of the previous example.

Figure 5.16 shows the temporal behavior of the LSBF phase-slope estimate of the angle of arrival, and Figure 5.17 shows the temporal behavior of the LSBF fractional amplitude variation across the array. Even before the initial rise in echo amplitude was complete, significant quasi-sinusoidal fluctuations in both the angle of arrival and the fractional amplitude variation had begun to occur. As well, there was a small linear trend in the angle of arrival, which could have been due to a wind-shear induced motion of the main echo specular reflection point. If this trend is allowed for, the corresponding temporal fluctuations of the amplitude and phase slopes appear to be in quadrature, consistent with the single secondary signal model of Section 3.5.3, and in particular with eqns. (3.58) and (3.61).

In addition, eqns. (3.57) and (3.61) show that the spatially averaged temporal fluctuations of the absolute amplitude and the large-scale phase-slope fluctuations should be either in phase concert or in

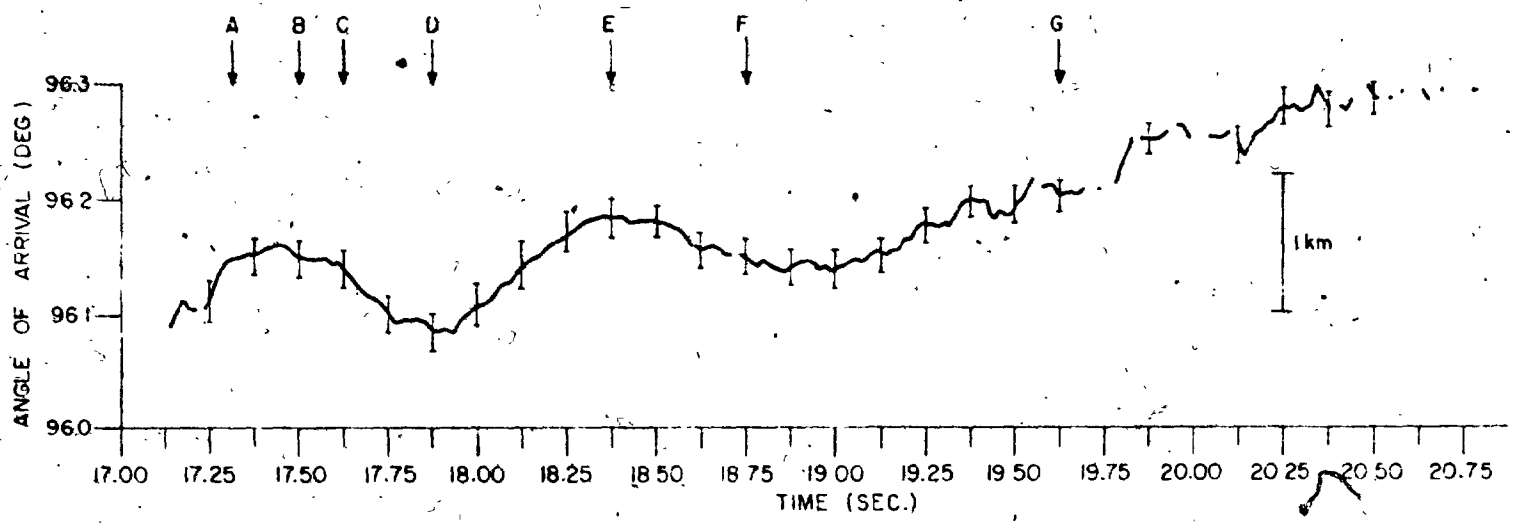

Figure 5.16. Angle of arrival from LSBF phase slope - Echo III

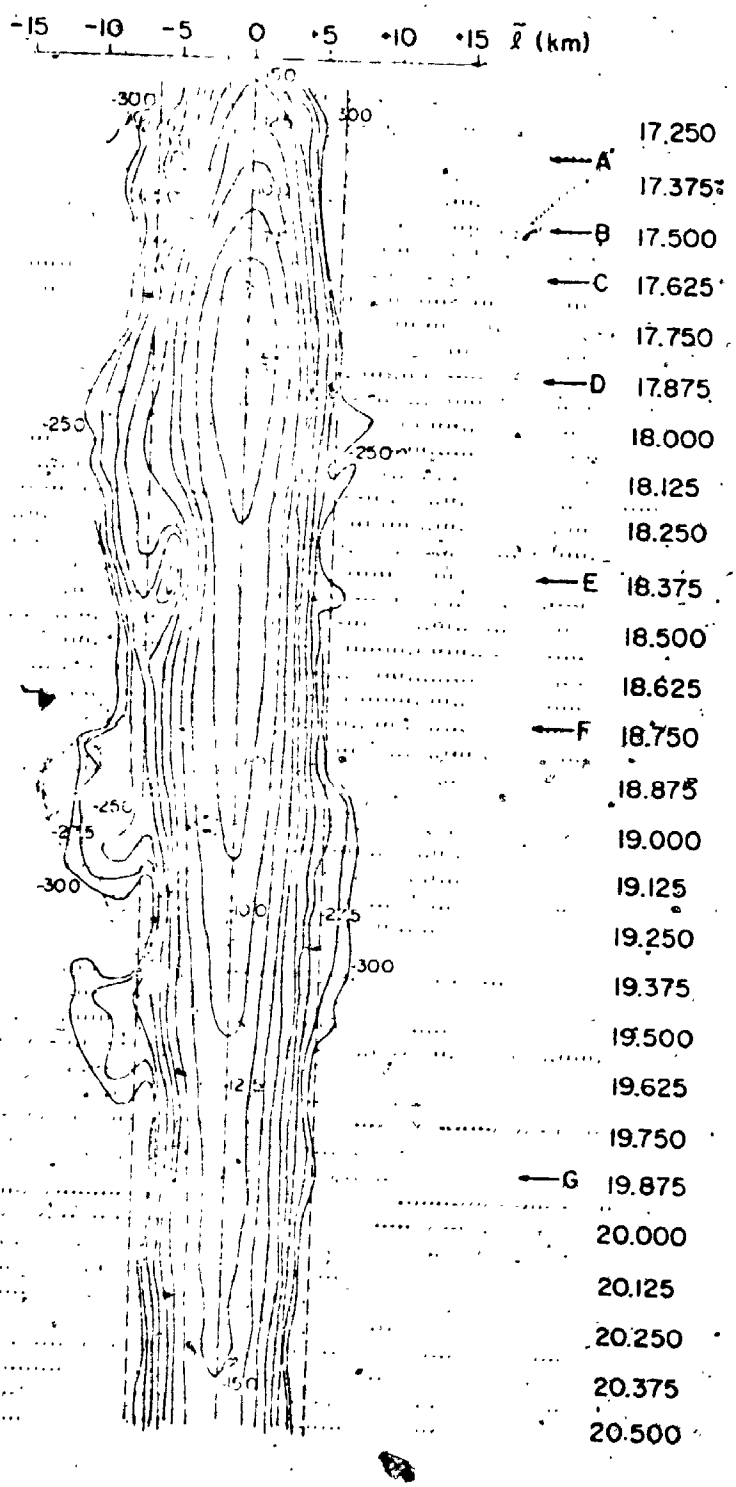

Figure 5.20. Angular spectra - Echo III

phase opposition, according to whether the algebraic sign of k_1 was negative or positive, respectively. Thus the coincidence at the time "B" of the negative fluctuation in the absolute amplitude with the local maximum of a positive fluctuation in the angle of arrival (negative fluctuation in phase-slope) is also in agreement with the single secondary signal model. The inference that k_1 was negative and hence that the secondary signal scattering centre was located upwards along the trail axis from the main echo reflection point can also be made.

5.3.2 Spatial Phase and Amplitude Observations - Echo III

Figures 5.18 a-d show the phase variations observed across the array, and Figures 5.19 a-d show the normalized amplitude observed across the array. These figures indicate the presence in the spatial data of structure with significant amplitude and with scale-size comparable to the length of the array. The implication of the presence of such structure is two-fold. First, for this example the deduced LSBF fractional amplitude variations and LSBF angle of arrival fluctuations were based on somewhat invalid attempts to fit straight lines to temporally varying quasi-sinusoidal spatial fluctuations with wavelengths approximately equal to the length of the antenna array; certainly the linear approximation model for the amplitude and phase slopes of eqns. (3.63) and (3.64) was not valid. Second, resolved secondary echo signals should be observable in the spatial Fourier transforms of the data.

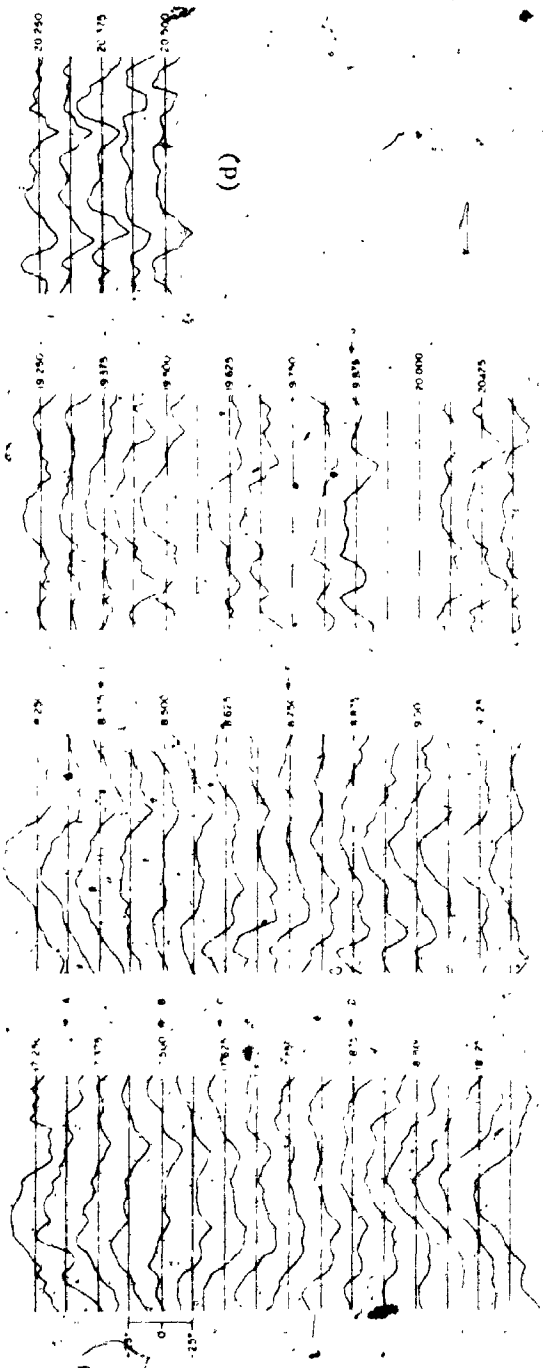

Figure 5.18. Spatial phase fluctuations - Echo III

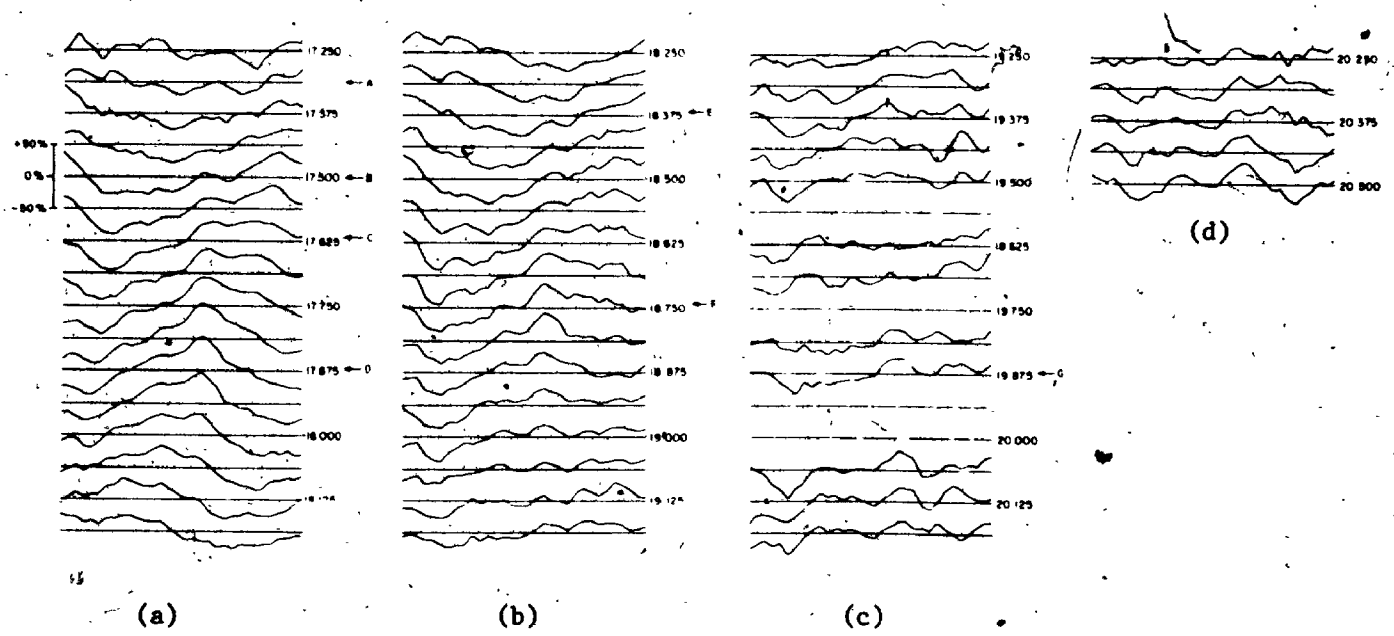

Figure 5.19. Spatial amplitude fluctuations - echo III

5.3.3 Angular Spectra - Echo III

Figure 5.20 shows the spatial Fourier transforms of the data of Figures 5.15, 5.18 a-d and 5.19 a-d as computed using -30 dB side-lobe Dolph-Chebyshev weighting. This figure shows a clearly resolved secondary echo signal which, although about 15 dB below the main echo amplitude (18% of the main echo amplitude), appears to have had an initial amplitude rise similar to that of the main echo. The apparent location of the scattering centre for this secondary echo was a point about -6.6 km along the trail axis above the main echo reflection point, at a vertical height of 2.6 km above the main echo reflection point. The LSBF amplitude-slope and phase-slope fluctuations observed between the times "A" and "F" can then be explained on the basis of the readily observed subsequent angular convergence and divergence of the main and secondary echo signals and the consequent effect of the temporal changes in the relative phase ϕ_d (eqn. (3.54)) on the spatial derivatives of the amplitude and phase (eqns. (3.58) and (3.61)). The cessation of these fluctuations at the time "F" can be seen to have coincided with the disappearance of the secondary echo.

There is also evidence in Figure 5.20 of the development and disappearance of two more almost-resolved secondary echoes scattered from points apparently above the main specular reflection point, as well as the intervening appearance and disappearance of a less well resolved secondary echo apparently from below the main specular reflection point. The presence of these three secondary echoes is not readily inferred from any of the four previous figures.

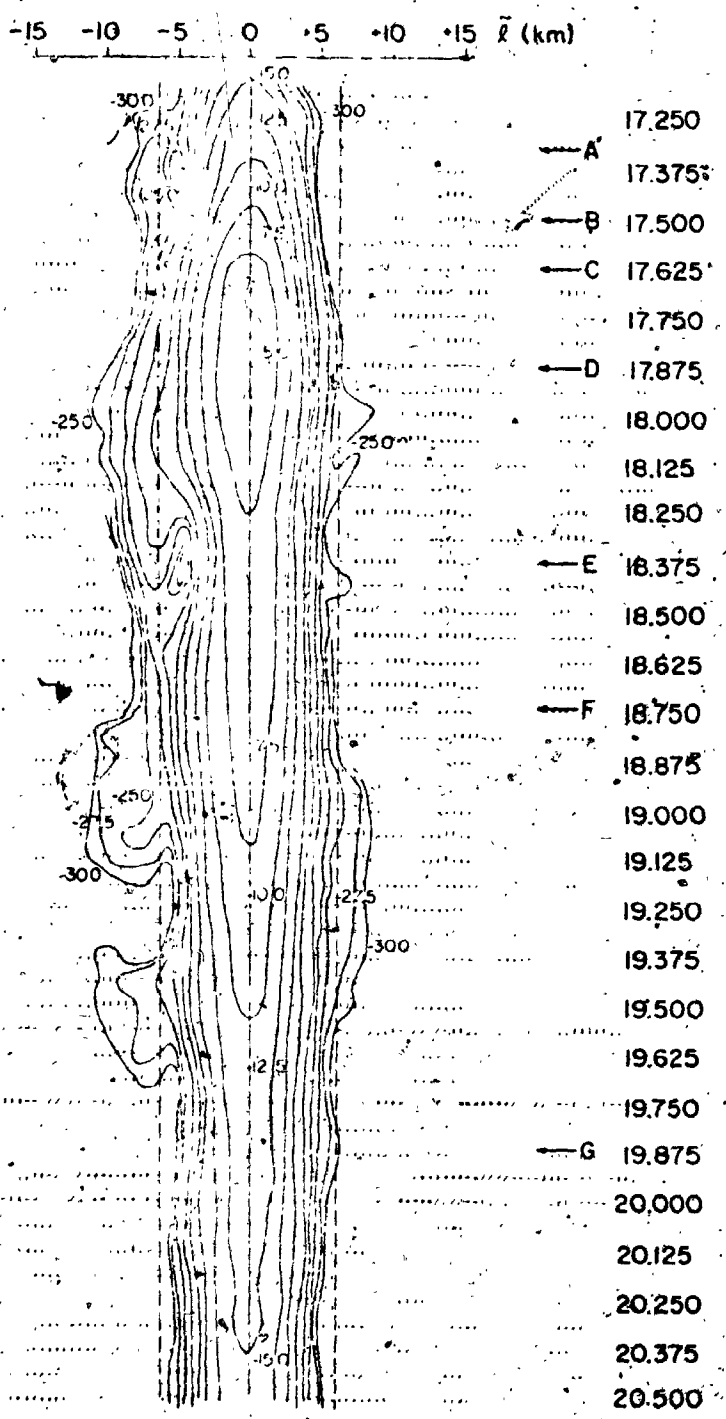

Figure 5.20. Angular spectra - Echo III

5.3.4 The Data in Terms of Meteoroid Fragmentation - Echo III

Figure 5.21 shows the location of the main specular reflection point and the resolved secondary scattering centres as scaled from the data shown in Figure 5.20. The loss of resolution of the secondary echo signal for apparent axial separations of the secondary scattering point and the main reflection point of less than 6.2 km due to the width of the central peak of the aperture response function is the reason for the absence of data between the times "B" and 1/8 second before the time "E".

It can be seen in Figure 5.21 that the first secondary echo began to appear at $\tilde{\ell}_s = -6.8$ km about 0.22 second after the expected time of passage of the main meteoroid. Equation(5.7) becomes, for this example,

$$\tilde{\ell}_s(t) = -(128 \pm 7) \frac{\partial}{\partial \ell} (\underline{\rho}'' \cdot \hat{n}_o)_{\ell=\ell_s} \qquad (5.18)$$

Therefore if this secondary echo were due to a specular reflection from a trail component caused by a fragment of the same meteoroid which caused the main echo, then such a trail component must have been oriented about 3.8° from the main echo trail axis as measured in the $(\hat{n}_o, \hat{\ell})$ plane. After formation, the secondary reflection point moved towards the main reflection point at a rate corresponding to a vertical shear of the horizontal wind in the $(\hat{n}_o, \hat{\ell})$ plane of 58 m/sec per kilometre of vertical displacement, until the secondary echo became unresolvable from the main echo. The observable correlation between the upward fluctuation of the apparent location of the main specular reflection point and the loss of resolution of the secondary echo supports the

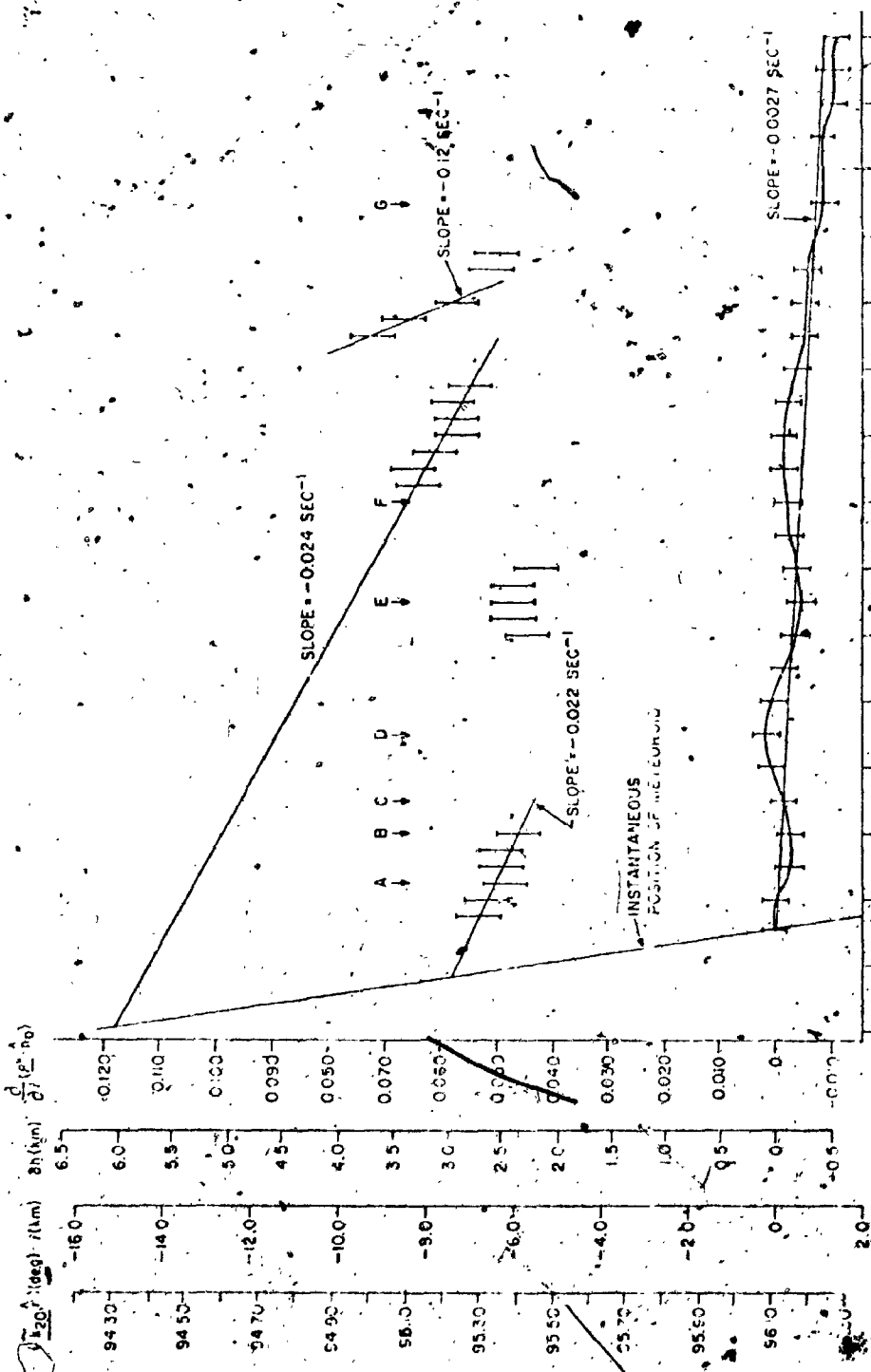

Figure 5.21. Estimated locations of echo scattering centres - Echo III

assertion made above that the fluctuations of the apparent location of the main echo reflection point were due to interference with the secondary echo.

The re-emergence of the secondary echo about 0.75 second later indicates that if the motions of the secondary reflection point were due solely to wind-shear effects, then such shears must have been more complicated than those inferred from the previous two examples. There is also the additional complicating factor that the reflection coefficient of the main trail was transitional, so that the simple model of eqn. (5.9) was not applicable. Figure 5.22 shows a plot of the instantaneous amplitude of the resolved secondary echoes as scaled from the data of Figure 5.20. This plot shows that the amplitude of the first secondary echo increased as time passed, as would be expected in the case that the trail was being distorted by winds in such a manner that the effective length of trail contributing to the reflection was increasing more quickly than the reflection coefficient was decreasing due to trail diffusion. Such a "focussing" effect would also imply the existence of nonlinear vertical shears of the horizontal winds.

In view of the relatively small amplitude of the first secondary echo as compared to the main echo, it might seem likely that the reflection coefficient of the secondary echo scatterer behaved in an underdense manner. By assuming this to be the case, it can be shown from eqns. (3.76) and (5.2) that at 100 km, the geometrically estimated height of the secondary echo, the estimated underdense echo decay time would be 0.83 second. Thus, over the observed 1.3 second lifetime of the secondary echo, the reflection coefficient would be expected to have decreased by a factor of 0.21, or 13.6 dB. Extrapolating back

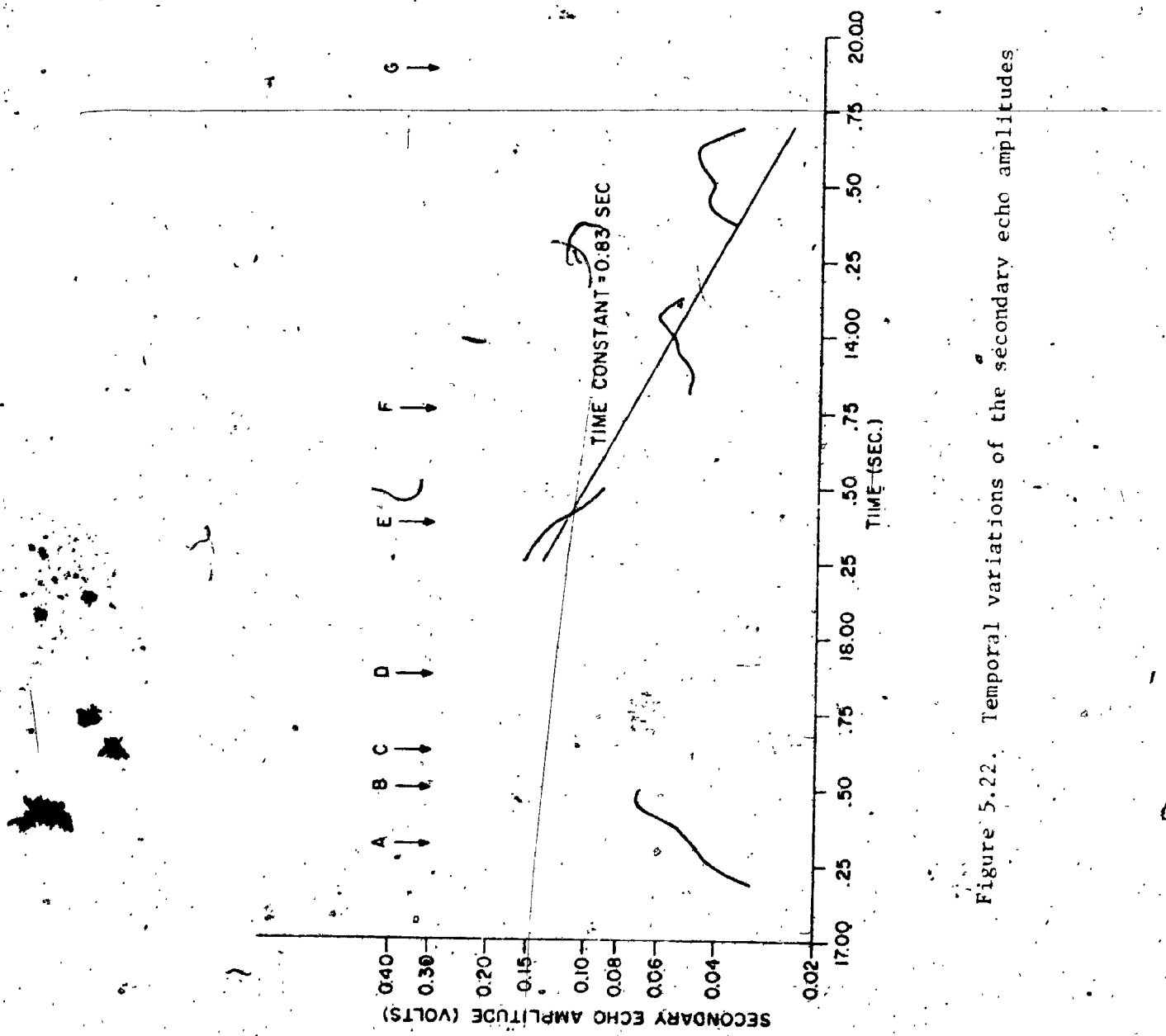

Figure 5.22. Temporal variations of the secondary echo amplitudes

from the echo amplitudes observed near the end of the life of the secondary echo shows that if all the increase in echo amplitude were to be attributed to wind-shear distortion effects, then for a suitably oriented secondary trail segment an initial amplitude as great as 0.4 volts might have been observed. Since this amplitude is greater than the observed initial amplitude of the main echo, the validity of such an extrapolation is suspect.

The data, however, are consistent with the assumption that the reflection coefficient of the secondary echo scatterer was non-uniform. If this were the case, then the observed increase in echo amplitude would be attributable to the increase in the reflection coefficient as the reflection point moved along the trail axis. This argument is dealt with again below.

The location and amplitude of the secondary echo which appeared at the time "F" have also been plotted in Figures 5.21 and 5.22 respectively. While there was significant spatial separation between this and the earlier secondary echo, it is interesting to note that a line corresponding to an exponential decay time of 0.83 second can be drawn through the amplitudes of both echo components with reasonable agreement, indicating the possibility that both secondary echoes could have been due to the same secondary trail segment. Also, the wind-shear component of 63 m/sec per kilometre of vertical displacement deduced from this secondary echo is within 10% of that estimated from the first observation of the secondary echo.

There were also two other secondary echo components present. One was angularly unresolved, lying below the main specular reflection point and occurring about 3/16 second after the time "F". The other

displayed an angularly broad peak and occurred above the main reflection point about 5/8 second after the time "F". The observed locations and amplitudes of the latter secondary echo were also plotted in Figures 5.21 and 5.22. Figure 5.21 shows that although the same range of apparent reflection point locations was traversed as by the first two secondary echoes, the deduced wind shear of 292 m/sec per kilometre of vertical displacement is almost five times as great as that deduced above. Figure 5.22 shows that the observed amplitude of the secondary echo was close to that expected if the trail segment responsible for this reflection were the same one as above. However, there is no simple explanation as to how a single trail segment could be reoriented so quickly except if extremely variable wind shears of large magnitude were present. This seems unlikely, and inconsistent with other observations.

The most reasonable explanation again seems to be that each discontinuous secondary echo was due to a different secondary trail, and that the apparent consistency of the amplitude data was simply fortuitous. This hypothesis is also consistent with the observation that the secondary echoes were located at heights above the main specular reflection point and yet exhibited a downward motion. This is contrary to what would be expected intuitively if all the secondary echoes were due to distortion of a single trail: that secondary echoes due to linear vertical wind shears would tend to move away from the main specular reflection point.

The geometry of the first and second echoes were then investigated in a manner similar to the previous two cases (Sections 5.1.5 and 5.2.5). If the first secondary echo were to have been initially parallel

to the main echo trail and at the same echo range when first observed, then it would have been located about 200 m higher than the main echo trail and about 66 km closer to the transmitter. Similarly, if the second secondary echo were to have been initially parallel to the main echo trail and at the same echo range when first observed, then it too would have been located about 200 m higher than the main echo trail and about 70 km closer to the transmitter. For both these cases the incremental changes in the estimated heights and locations as a function of the error in estimating the echo range were similar to those given for the main echo location in Table 5.1; i.e., a ± 3 km error in the estimate of range would correspond to a ± 5 km error in estimated height and a ∓ 16 km error in location along the transmitter-receiver axis. Thus it is clear that initially parallel secondary echo trails would have been independent of the main echo meteoroid.

The hypothesis that the first two secondary echoes were due to diverging fragments of the main echo meteoroid was also further explored. The echo which occurred at the time "A" corresponded to an initial value for $\delta\chi$ of 0.058 radian or 3.3° as mentioned above, and for $\ell_m \cos\chi$ of -2.7 km. Substitution of these values into eqn. (5.12) yielded the formula

$$\Delta h = 7.5\,(\delta h - 2.7) + 2.7 \qquad (5.19)$$

This equation is consistent with the clearly obvious inference of Figure 5.22, that the fragment could have been cast off at any incremental height Δh greater than about 2.7 km or altitude h greater than about 103 km. It further shows that a 1 km error in estimating δh would correspond to a 7.5 km error in estimating Δh.

Similarly, for the secondary echo observed at the time "F", $\delta\chi \simeq 0.12$ radian or 6.7^{o} and $\ell_m \cos\chi \approx 3.3$ km so that eqn. (5.12) became

$$\Delta h = 3.6\ (\delta h - 3.3) + 3.3 \qquad (5.20)$$

and this secondary meteoroid could have been released at any altitude h greater than about 103.5 km. Each kilometre error in the estimated value of δh would correspond to an error of 3.6 km in the estimated value of Δh.

The fact that the first and second secondary echoes occurred over contiguous regions of the height and yet the first and apparently lower secondary echo was observed initially at a lower height suggests that the first secondary echo trail did indeed separate from the main meteoroid at lower heights than the second; for had the ionization of the first secondary echo extended higher, it should have been observed at those greater heights, since it appears to have experienced the same wind shear as the second secondary echo trail. This suggestion is also consistent with the observed temporal increase in the amplitude of the first secondary echo. Such an increase would be expected if the reflection point was moving down the axis of a secondary trail from the point at which the secondary meteoroid began to ablate, since then both the length and the reflection coefficients of the portion of the trail contributing to the echo would be expected to be increasing.

The same argument regarding the maximum height of observation as used above could also be applicable to the second secondary echo, since its amplitude was also increasing with decreasing altitude. The abrupt end to its observation could be attributed to the possibility

that the lower end of the trail was encountered as the reflection point moved along the rotating trail.

The reappearance of the first secondary echo is not straightforward to explain. It is not clear from the angular spectra plot of Figure 5.20 whether the portion of this echo centred about the time "E" was due to the same secondary trail as the first part, although the temporal continuity of the spatial amplitude and phase data strongly suggests that it was. If, in fact, this was so, then there must have been a discontinuity with height in the wind shear at about 2.4 km above the main echo height. The wind shear of 6.6 m/sec per kilometre of vertical displacement deduced from the observed mean motion of the main echo reflection point was certainly much less than that deduced from the motions of the secondary echoes observed at greater heights, but whether the wind shear actually changed abruptly over an apparently very small height increment is not clear. However, such a possibility is consistent with the chemiluminescent rocket trail observations of Bedinger *et al.* (1968) mentioned above.

It also is not clear by what mechanism the echo amplitude essentially doubled, if the first and second secondary echoes were due to the same secondary trail, but perhaps the smaller "stretching" effect associated with a region of smaller wind shear combined with the longer echo decay time at the slightly lower height could explain the effect. However, it seems most likely that the line density of the trail was greater at the lower height, especially if the secondary meteoroid had fragmented off the main meteoroid only about a kilometre or two higher than the observation points along the secondary trail. The ultimate disappearance of this secondary echo appears to be due to

obscuration by the main echo combined with the decay of the secondary echo.

In summary, this echo appears to have been due to a larger meteoroid and it displayed a more complicated behavior than the previous two examples. The meteoroid appeared to have cast off at least two fragments which produced clearly observable secondary echoes, and there was evidence of a third, unresolved, secondary echo as well. The behavior of both the main and secondary echoes after their formation indicated the presence of significant wind shears which varied considerably as a function of height.

CHAPTER 6

SUMMARY, CONCLUSIONS, DISCUSSION AND SUGGESTIONS FOR FURTHER STUDIES

6.0 Summary

In this thesis, a brief review of relevant radio meteor research has been given, the experimental equipment has been described, a theory for interpreting the diffraction pattern of radio signals scattered by meteor trail ionization has been developed, and three typical sets of meteor echo data have been analyzed. The conclusions of this study are given below in Section 6.1, the results are discussed in Section 6.2, and suggestions for further studies are given in Section 6.3.

6.1 Conclusions

New and direct observations of the existence of angularly resolved multiple reflections from three apparently simple radio meteor echoes have been presented in Chapter 5. These observations were made by computing the spatial Fourier transforms of the diffraction patterns of the echoes observed at 38.1 m (125 foot) intervals across a 1181.1 m (3875 foot) aperture. The transformed data yielded estimates of the angular spectra of the received echo signals. Because echoes from meteors from a shower of known orientation (the Quadrantid shower) were observed, it was possible to make quantitative estimates of the reflection point locations and of one component of their motions.

A major conclusion drawn from the observations is that the deduced vertical gradients or shears of the (assumed) horizontal winds appeared to be insufficient to cause the observed secondary echoes by the distortion of a single initially straight meteor trail. While the magnitudes of the deduced shears were reasonable, being up to the order of a few tens of metres per second per kilometre of vertical displacement, the relatively short times which elapsed between the observations of the main and secondary echoes were too brief to have allowed the deduced shears to have rotated a segment of a single straight trail through the angle necessary for it to satisfy the specular reflection condition. Therefore it was concluded that the secondary echoes were due to different trails than the main echoes.

Analysis of the geometry showed that if the meteor trails which gave rise to the secondary echoes were initially parallel to the main echo trail, then the horizontal separations between the various trails in two cases (Sections 5.2 and 5.3) would have been so great as to preclude the possibility of a common source for the responsible meteoroids. Conversely, it appeared in two cases (Sections 5.1 and 5.3) that if there were a small angular divergence of a few degrees between the axes of the main and secondary echo trails, as might occur if a parent meteoroid were to fragment at a height above that at which the secondary echo reflections were observed, then both the main echo and secondary echo trails could have had a common source. However, there is an absence of independent corroborative evidence that meteoroids of sizes which give rise to underdense and transitional echoes undergo fragmentation at heights of more

than 100 km and with fragment path angular divergences of greater than a degree. Hence the fragmentation hypothesis must as yet be regarded as speculative.

6.2 Discussion

The geometry of the fragmentation hypothesis was developed in Appendix D and the dynamics of this hypothesis were considered in Appendix E. The fragmentation hypothesis was shown to be consistent with the observations in two cases (Sections 5.1 and 5.3) where the secondary echoes were observed at heights greater than the main echo, and inconsistent in one case (Section 5.2), where the secondary echo was observed at an apparently lower height than the main echo. That trails due to fragments which could be associated with the main echo meteoroid were observed only above the main echo reflection point is not inconsistent with the classical theory of meteoroid ablation (McKinley, 1961), which predicts that smaller meteoroids ought to ablate and "burn out" at higher heights than do the larger ones.

The mechanisms of meteor fragmentation and ablation are still the subject of much study: a recent paper by Hawkes and Jones (1975) summarizes much of this work. Current opinion is that even small "meteoroids have a porous, loosely conglomerate structure similar to that found for photographic and visual meteoroids..." (Hughes, 1974).

Some previous radio studies of meteors have attempted to examine fragmentation effects by observing the amplitude and phase of echoes as the meteor trails were being formed (Rice, 1964; Rice and Forsyth, 1964;

Brown, 1972; and Cook *et al.*, 1972). These experiments showed the effects of enhanced ionization expected from the ablation of fragments close to the main meteoroid, but if these fragments were cast off at angles of a few degrees to the paths of the main meteoroid, then most of the echo power scattered by the trails thus generated would be reflected in directions other than towards the receiving antenna. Other experiments, using pulse radar techniques to examine the behavior of overdense echo amplitudes as a function of range and time during and after the time when the trails were being formed, have observed the almost simultaneous formation of small but significant echoes from ranges other than those of the main echo specular reflection points (McKinley and Millman, 1949; McKinley, 1961). These same experiments also often observed the formation of additional small but significant echoes at times well after the time of passage of the meteoroid through the observed echo range. The inference of these experiments was that the observed echoes must have been due to "rough" trails, produced by fragmenting meteoroids, and that wind motions could have been responsible for the later formation of the additional observed echoes.

The present experiment, conversely, was incapable either of observing the formation of the echo, due to the narrow (30 Hz) system bandwidth, or of resolving the differential range between the main and secondary echoes; but it was possible to observe the echoes from secondary trails produced by those fragments which were large enough and which were fortuitously oriented so as to produce angularly resolved secondary echoes of detectable amplitude.

The question of whether or not fragments actually can be cast off from a meteoroid at angles of a few degrees appears not to have been investigated. This question is attacked in Appendix E, using simple energetic considerations. It is shown there, in Table E.1, that only a small fraction of the initial meteoroid kinetic energy would be required to scatter a small but significant fragment of the main meteoroid along a path a few degrees divergent from that of remaining major portion of the meteoroid, which itself would be deviated through a much to somewhat smaller angle.

There is direct photographic evidence (Hemenway and Soberman, 1962) that some small meteoroids are highly irregular in shape, and it is reasonable to expect that small fragments could be broken off such meteoroids early in their encounter with atmospheric friction. Even the smooth spherical dustball model for meteoroids considered by Hawkes and Jones (1975), "...consisting of grains of a high melting-point material (e.g., stone or iron) ... held together by ... some binding material of a lower melting-point ..." was shown for meteoroids of the size responsible for strong underdense and trasitional echoes to have fragmented almost completely due to the melting of the binding material above altitudes where significant deposition ofionization due to ablation of the grains would occur. This model makes no predictions about the angular spread of the paths of the fragments, but it is pointed out in the conclusion of the paper that a combination of this spherical model with some other fragmentation theory is possible. It seems plausible that particles formed in space, and not previously subjected

to any erosive conditions, ought to be somewhat rough, so that if the Hawkes and Jones model for meteoroid composition is correct, some larger chunks as well as the elementary grains could be cast off as the binding material melts. Such larger chunks would then behave as small, independent meteoroids which would produce secondary echoes in the manner observed here.

6.3 Suggestions for Further Studies

In view of the interesting results obtained by this experiment, it is natural to enquire in what manner better data capable of yielding more information could be obtained. The key questions for such improvement lie in the realm of increasing the system sensitivity and the spatial resolution along the trail axis.

The straightforward approach of increasing the system sensitivity by increasing the transmitted power would certainly increase the number of echoes observed. The majority of the additional data collected would be from underdense trails, which theoretically ought to be the simplest to analyze. System sensitivity could also be increased by replacing the essentially non-directive transmitting and receiving antenna elements with more directive elements, at a cost of reducing the radio frequency bandwidth over which the system could be operated.

The resolution along the trail axis could be improved either by increasing the length of the antenna array or by altering the scattering geometry by moving the transmitter closer to the receiving array. It is apparent from the data that for the present geometry, a much coarser aperture sampling than was actually used would have been satisfactory.

Therefore a system of no greater electronic complexity and simply having a longer effective array length by using a longer inter-element spacing would have been more effective. Of course, it would be necessary to have a few elements at close spacing, of the order of half a wavelength of the transmitted signal, in order to be able to determine the angle of arrival of the echo signal unambiguously and thus to deduce the location of the trail in the sky.

Moving the transmitter closer to the receiving array would enhance the axial resolution of the system, since as can be seen from either eqn. (3.68) or (3.70) this resolution is proportional to the distance from the trail to the receiving array. The cost of this enhanced resolution would be the decrease in observation time caused by the loss of the geometric enhancement of the underdense echo decay time which occurs in the case of large forward-scatter angles (cf. eqn. (3.76)). As well, the larger echo elevation angles which would be observed would require the use of antenna elements which are sensitive at these higher elevation angles, so that the use of inefficient loop elements might be required. The losses incurred by such elements could easily exceed the increase in echo power realized by the decrease in the spatial attenuation factor due to the decreased echo range.

APPENDIX A

MEASUREMENT AND CORRECTION OF SYSTEM DISTORTION EFFECTS

A.0 Introduction

The philosophy adopted by users of the CRC HFDF system has been to measure accurately as many system characteristics as possible, and then to use these measurements to calibrate the recorded data as they were being processed. Two readily compensated sets of systematic effects were those due to the use of two sets of antenna cables of grossly different lengths (and hence attenuation and phase retardation characteristics), and those due to the slightly differing gain and phase-shift characteristics of the individual receivers.

A.1 Correction of Antenna Cable Effects

A.1.1 Correction of Cable Phase Effects

Careful measurement and analysis of the cable phase characteristics by E.L. Winacott showed that the following empirical formula yielded the difference in propagation delay-time $\Delta\tau$ cable (in μsec) for identical signals propagated down typical long and short cables, within a tolerance of $\pm 8 \times 10^{-5}$ μsec:

$$\Delta\tau_{cable} = 1.987676\ (1 - 40.7 \times 10^{-6}\ T_{cable})(1 + 0.01237272/f_{RF}^{\frac{1}{2}}) \qquad (A.1),$$

In this formula T_{cable} is the ambient temperature of the cable (in degrees Celcius) and f_{RF} is the radio frequency of the signal (in MHz). Evaluation of the relation

$$\Delta\phi_{cable} = 360^{o} f_{RF} \Delta\tau_{cable} \qquad (A.2)$$

will yield $\Delta\phi_{cable}$, the relative phase difference (in degrees) between the two signals.

This phase correction was applied to the phases of all data recorded from receivers connected to long cables before the data were further processed.

A.1.2 Correction of Cable Attenuation Effects

Over the frequency band 2-30 MHz, a good fit to the manufacturer's specification of the attenuation characteristics of the cables, which were presented in the form of an empirical graph, is given by the value 0.26 dB loss per 100 feet at a frequency of 10 MHz, varying as frequency to the power 0.53. Thus for a "short" cable 488.4 feet in length

$$\gamma_s = 1.27 \cdot (f_{RF}/10)^{0.53} \qquad (A.3)$$

where γ_s is the attenuation loss for a "short" cable (in dB) and f_{RF} is the radio frequency (in MHz). Similarly, for a "long" cable 2084.9 feet in length the attenuation loss γ_L (in dB) is given by

$$\gamma_L = 5.42 \, (f_{RF}/10)^{0.53} \qquad (A.4)$$

If it is assumed that the figure 0.26 dB/100 ft. is accurate to within 0.005 dB/100 ft., then at a frequency of 30 MHz the maximum expected error in γ_s and γ_L would be 0.04 dB and 0.19 dB respectively. Actual measurements have confirmed that the errors were no larger than this magnitude.

A.2 Measurement and Correction of Receiver Distortion Effects

A.2.1 Measurement and Calculation of the Receiver Distortions

When a signal of known amplitude and phase was applied to all the receiver inputs simultaneously, the amplitudes and phases of the signals observed at the various receiver outputs differed. In spite of careful adjustment of the receivers, typical variations in receiver gain were of order 0.8 dB in amplitude (10%) and the phases were quite random, although the variation of the phase differences between any arbitrarily selected pair of receivers rarely exceeded 10^{o} over the frequency band 2-30 MHz. Additional small distortions were introduced by minor differential gain imbalances in the gains of the two phase-sensitive-detector output channels (usually more than 35 dB below signal amplitude) and departures from phase quadrature (usually less than 1^{o}). The gain and phase variations were only slowly varying functions of radio frequency, and in all cases this dependence could be ignored over frequency bands of order 100 kHz in width.

To measure the receiver distortion effects, a known signal

$$s_{test} = a_o \cos[2\pi(f_{RF} + \Delta f)t] \qquad (A.5)$$

was applied simultaneously to the inputs of all the receivers. Here a_o is the test signal amplitude, of order 2 μV across 50 ohms (-110 dBm), f_{RF} is the test signal frequency, in the range 2-30 MHz, and Δf is an offset frequency within the passband of the receiver output filters.

Then the signals observed at the "in-phase" (I) and "quadrature" (Q) outputs of a particular receiver can be represented as

$$s_I(t) = a_o G_I \cos(2\pi \Delta f t + \phi_I) \quad \text{(A.6a)}$$

and

$$s_Q(t) = a_o G_Q \sin(2\pi \Delta f t + \phi_Q) \quad \text{(A.6b)}$$

where s_I and s_Q were the output signals from the I and Q channels, G_I and G_Q were the amplitude gain factors of the I and Q channels, and ϕ_I and ϕ_Q were the phase shifts of the I and Q channels.

The complex Fourier transform of the complex output signal

$$s_C(t) = s_I(t) + j\, s_Q(t) \quad \text{(A.7)}$$

where $j = (-1)^{\frac{1}{2}}$, is given by

$$S(f) = a_o[G_+ \delta(f - \Delta f) + G_- \delta(f + \Delta f)] \quad \text{(A.8)}$$

where

$$G_+ = \frac{1}{2}[G_I \exp(j\phi_I) + G_Q \exp(j\phi_Q)] \quad \text{(A.9a)}$$

and

$$G_- = \frac{1}{2}[G_I \exp(-j\phi_I) - G_Q \exp(-j\phi_Q)] \quad \text{(A.9b)}$$

In practice, finite discrete Fourier transforms which yield factors directly proportional to G_+ and G_- are computed.

Equations (A.9) can be manipulated to show that

$$G_I = \left\{[\mathrm{Re}(G_+ + G_-)]^2 + [\mathrm{Im}(G_+ - G_-)]^2\right\}^{\frac{1}{2}} \quad \text{(A.10a)}$$

$$G_Q = \left\{[\mathrm{Re}(G_+ - G_-)]^2 + [\mathrm{Im}(G_+ + G_-)]^2\right\}^{\frac{1}{2}} \quad \text{(A.10b)}$$

and

$$\tan \phi_I = \mathrm{Im}(G_+ - G_-)/\mathrm{Re}(G_+ + G_-) \qquad \text{(A.11a)}$$

$$\tan \phi_Q = \mathrm{Im}(G_+ + G_-)/\mathrm{Re}(G_+ - G_-) \qquad \text{(A.11b)}$$

If the definitions

$$G_o = \frac{1}{2}(G_I + G_Q) \qquad \text{(A.12)}$$

$$\delta G = (G_I - G_Q)/G_o \qquad \text{(A.13)}$$

and

$$\phi_o = \frac{1}{2}(\phi_I + \phi_Q) \qquad \text{(A.14)}$$

$$\delta\phi = \phi_I - \phi_Q \qquad \text{(A.15)}$$

are introduced, where G_o is the receiver mean amplitude gain factor, δG is the relative channel gain imbalance, ϕ_o is the receiver main phase shift, and $\delta\phi$ is the channel phase-shift imbalance (departure from quadrature), then,

$$G_I = G_o\left[1 + \frac{1}{2}\delta G\right] \qquad \text{(A.16a)}$$

$$G_Q = G_o\left[1 - \frac{1}{2}\delta G\right] \qquad \text{(A.16b)}$$

and

$$\phi_I = \phi_o + \frac{1}{2}\delta\phi \qquad \text{(A.17a)}$$

$$\phi_Q = \phi_o - \frac{1}{2}\delta\phi \qquad \text{(A.17b)}$$

Thus, for a known input test signal, all relevant distortion effects of each of the receivers can be measured.

A.2.2 Application of the Receiver Correction Factors

For a known sinusoidal input test signal, the outputs of a receiver can be expressed as

$$s_I(t) = a_o G_o \left[1 + \frac{1}{2}\delta G\right] \cos\left[2\pi \Delta f t + \phi_o + \frac{1}{2}\delta\phi\right] \qquad (A.18a)$$

$$s_Q(t) = a_o G_o \left[1 - \frac{1}{2}\delta G\right] \sin\left[2\pi \Delta f t + \phi_o - \frac{1}{2}\delta\phi\right] \qquad (A.18b)$$

The first step in the correction process is to eliminate the effects of I and Q channel gain imbalance by a pair of real multiplications to get

$$s'_I(t) = \left[1 + \frac{1}{2}\delta G\right]^{-1} s_I(t) = a_o G_o \cos\left[2\pi \Delta f t + \phi_o + \frac{1}{2}\delta\phi\right] \qquad (A.19a)$$

and

$$s'_Q(t) = \left[1 - \frac{1}{2}\delta G\right]^{-1} s_Q(t) = a_o G_o \sin\left[2\pi \Delta f t + \phi_o - \frac{1}{2}\delta\phi\right] \qquad (A.19b)$$

Then the effects of the channel phase imbalance can be eliminated between $s'_I(t)$ and $s'_Q(t)$ to show that

$$s''_I(t) = \left[s'_I(t) \cos\left[\frac{1}{2}\delta\phi\right] + s'_Q(t) \sin\left[\frac{1}{2}\delta\phi\right]\right] / \cos(\delta\phi)$$

$$= a_o G_o \cos(2\pi \Delta f t + \phi_o) \qquad (A.20a)$$

and

$$s''_Q(t) = \left[s'_Q(t) \cos\left[\frac{1}{2}\delta\phi\right] + s'_I(t) \sin\left[\frac{1}{2}\delta\phi\right]\right] / \cos(\delta\phi)$$

$$= a_o G_o \sin(2\pi \Delta f t + \phi_o) \qquad (A.20b)$$

It is obvious that if δG and/or $\delta\phi$ are negligible, the above manipulations reduce to identity transformations.

The correction of the effective receiver gain from G_o to a desired value G_{oo} and the elimination of the phase shift ϕ_o can now be accomplished by the performance of a single complex manipulation of the complex signal

$$s''_C(t) = s''_I(t) + j\, s''_Q(t) \tag{A.21}$$

by the complex factor $(G_{oo}/G_o)\exp(-j\phi_o)$:

$$\begin{aligned} s'''_C(t) &= (G_{oo}/G_o)\exp(-j\phi_o)[s''_I(t) + j\, s''_Q(t)] \\ &= a_o G_{oo} \exp(j\, 2\pi\Delta f t) \end{aligned} \tag{A.22}$$

If the receivers were linear, then any narrow band signal with output centre frequency Δf and unknown amplitude and phase could be corrected by application of the above procedures.

For values of output frequency Δf near the filter cut-off frequency the characteristics of the individual filters differed more than at lower frequencies. This problem was easily overcome by measuring the values of G_o, ϕ_o, δG and $\delta\phi$ for each receiver for different values of Δf, and then choosing the set of correction factors appropriate to the data to be corrected.

Two simplifying assumptions were made tacitly for the above analysis. The first was that there were no dc offsets in the I and Q outputs, a chronic problem with phase-sensitive detectors. In practice, these offsets were measured during the calibration procedure and the

observed dc offsets were subtracted from the data before any further corrections were applied. The second assumption was that constant frequency test signals were used. In practice SFCW test signals were employed so that operating conditions as close as possible to those existing when actual data were being recorded were achieved.

A.3 The Effect of Sequential Sampling of the Receiver Output Signals

The sequential multiplexer and analog-to-digital converter could sample and quantize a sequence of input signals at the rate of 23.15 μsec per conversion. Therefore, to sample both outputs of a single receiver required 46.3 μsec, and to sample the outputs of 64 receivers required 2.96 msec. For an output signal of frequency $\Delta f = 15$ Hz, the phase shift which could occur in the signal from the last receiver to be sampled relative to the signal from the first due to the effect of sequential sampling would be 15.6°. Because this phase shift was linear across a set of recorded receiver outputs, however, a crude estimate (e.g., ± 1 Hz) of the value of Δf was sufficient to allow reduction of this phase shift to acceptable levels (e.g., about $\pm 1^{\circ}$ of pulse for $\Delta f = 15$ Hz, and proportionally less for smaller values of Δf).

APPENDIX B

LOCATING THE SPECULAR REFLECTION POINT OF A TRAIL FROM A KNOWN RADIANT

B.0 Introduction

It is possible to determine the location of the initial specular reflection point (SRP) of a radio echo from a straight-line meteor trail if the celestial coordinates of the meteor radiant point are assumed known and the angle of arrival of the echo to the axis of the antenna array and the echo propagation path length $2R_o$ can be measured. The problem consists of two distinct parts: the first is to determine the direction cosines of the trail in the local coordinate system defined in Chapter 3, and the second is to solve a set of simultaneous equations which determine the location of the SRP in this coordinate system.

B.1 Determination of the Trail Direction Cosines

The determination of the trail direction cosines consists of solving a spherical triangle on the surface of the celestial sphere. If at the mid-point M of the great-circle path joining the transmitter T and the origin of the receiving array R the instantaneous zenith angle of the radiant point is χ_M and its instantaneous azimuth angle relative to the great circle directed from T to R is Φ_M (reckoned positive clockwise, following the astronomical and geographical convention) then the local direction cosines of the trail, (α,β,γ), are given by

$$\alpha = \sin \chi_M \sin \Phi_M \qquad \text{(B.1a)}$$

$$\beta = -\cos \chi_M \qquad \text{(B.1b)}$$

$$\gamma = -\sin \chi_M \cos \Phi_M \qquad \text{(B.1c)}$$

The angles Φ_M and χ_S are readily computed from the known or assumed right ascension and declination of the radiant point by following the procedure outlined in the Explanatory Supplement to the Astronomical Ephemeris and the American Ephemeris and Nautical Almanac (1963).

B.2 Determination of the Reflection Point

The following set of four equations in four unknowns can be solved to determine the SRP (ξ_o, η_o, ζ_o) if the echo propagation path length $2R_o$ and the angle $(\underline{k_{20}}, \hat{r})$ are known:

$$\xi_o^2 + \eta_o^2 + \zeta_o^2[1 - (Z_0/R_0)^2] = R_0^2[1 - (Z_0/R_0)^2] \qquad \text{(B.2a)}$$

$$\xi_o^2 + \eta_o^2 + (Z_0 - \zeta_o)^2 = R_{20}^2 \qquad \text{(B.2b)}$$

$$a\xi_o + b\eta_o + c(\zeta_o - Z_0) = -R_{20} \cos(\underline{k_{20}}, \hat{r}) \qquad \text{(B.2c)}$$

$$\alpha\xi_o + \beta\eta_o + \gamma\zeta_o[1 - (Z_0/R_0)^2] = 0 \qquad \text{(B.2d)}$$

Equation (B.2a) is the equation of the surface of the prolate spheroid on which the measured value of R_0 constrains the SRP to lie; eqn. (B.2b) is an explicit formula for the length of the vector $\underline{R_{20}}$; eqn. (B.2c) is the vector dot product of $\underline{R_{20}}$ and a unit vector

$$\hat{r} = a\hat{i} + b\hat{j} + c\hat{k} \qquad \text{(B.3)}$$

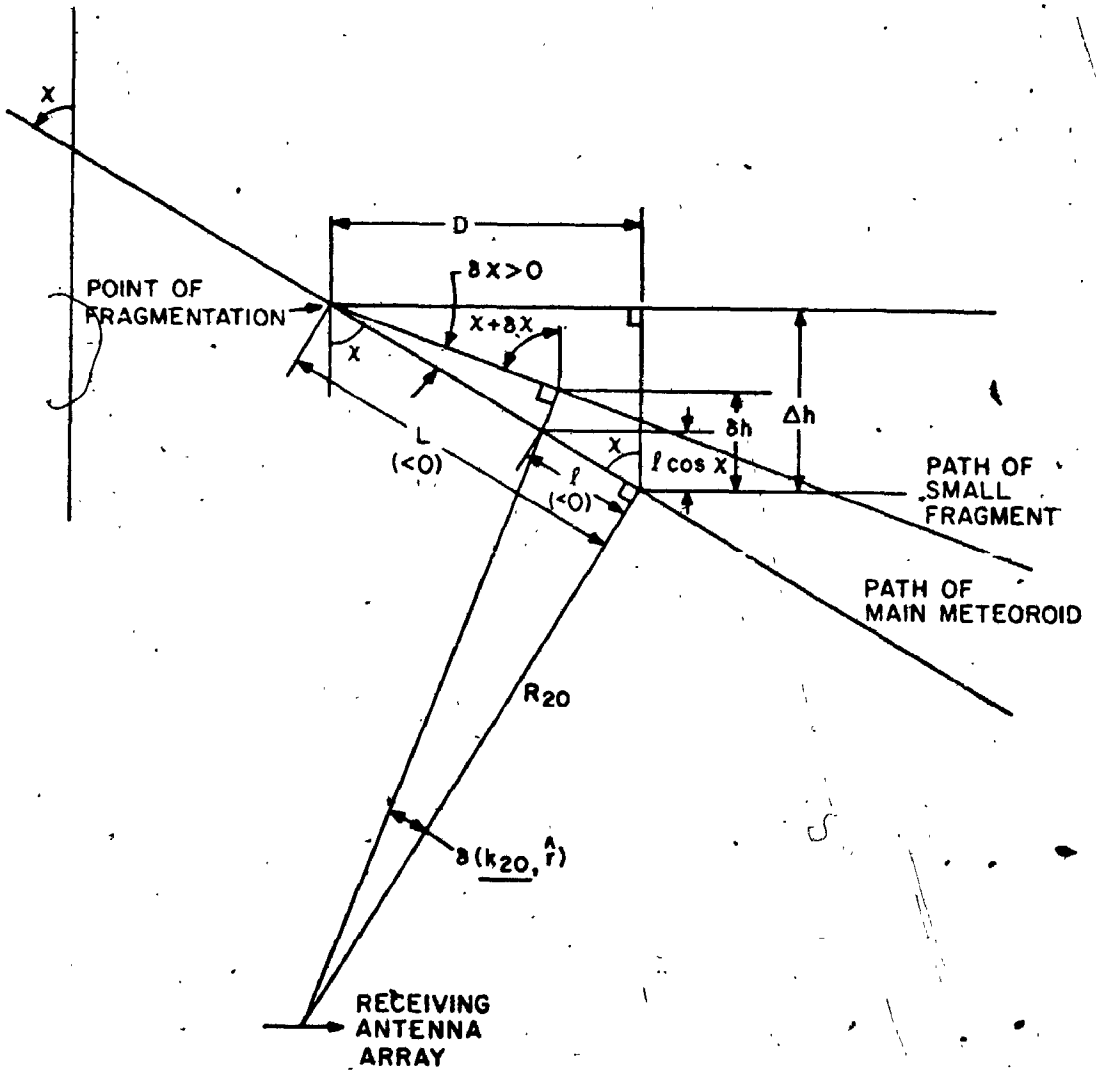

Figure D.1. Secondary trail scattering geometry

$$R_{20} = R_0 - (Z_0/R_0)\zeta_o \qquad (B.8)$$

Finally ξ_o can be calculated from

$$\xi_o = -(1/a)[R_{20}\cos(\underline{k_{20}}, \hat{r}) + b\eta_o - c(Z_0 - \zeta_o)] \qquad (B.9)$$

B.3 Determination of the Height of Reflection and the Local Radiant Zenith Angle

Simple geometric considerations show that the height h of the SRP above the surface of the spherical earth is given by

$$h = \left\{\xi_o^2 + [\eta_o + (R_E^2 - Z_o^2)^{1/2}]^2 + \zeta_o^2\right\}^2 - R_E \qquad (B.10)$$

where $R_E = 6371$ km is the assumed radius of the earth, and the local zenith angle χ of the radiant is given by

$$\cos\chi = -B\left\{\frac{1 + (\eta_o - \delta)/R_E}{1 + h/R_E}\right\} - \frac{\alpha\xi_o + \gamma\zeta_o}{R_E + h} \qquad (B.11)$$

where

$$\delta = R_E - (R_E^2 - Z_o^2)^{1/2} \qquad (B.12)$$

is the distance of the origin of the coordinate system below the surface of the spherical earth.

APPENDIX C

EXTERNAL NOISE AND INTERFERENCE OBSERVATIONS

C.0 Introduction

In the frequency band 22-27 MHz, within which most of the potentially reducable data were obtained, the interfering noise was due primarily to two external sources: natural, or galactic and atmospheric noise, and man-made interference, in the form of fixed-frequency transmissions. The energy from each of these two types of sources caused two distinct types of interference.

C.1 Naturally Occurring Noise

Naturally occurring noise tends to be broadband and incoherent. The absolute noise amplitudes observed at the receiver outputs and averaged across the antenna array were typically 200 mV (cf. the receiver noise amplitude of 22 mV, from Table 2.1). If it is assumed that the noise power is spatially isotropic, spectrally white, and has Gaussian statistical distribution, the amplitudes observed at the individual receiver outputs will be Rayleigh distributed. The RMS noise voltage at each receiver output will then be $(2/\pi)^{\frac{1}{2}} \times 200$ mV, or 160 mV (S.O. Rice, 1944). Further, the expected value of the ratio of the observed standard deviation of the instantaneous receiver noise amplitudes to their mean across the antenna array should be $(4/\pi - 1)^{\frac{1}{2}}$ or 0.52. The observed values of this ratio, in the absence of readily identifiable fixed-frequency interference, were all of this order, not inconsistent with the assumed model for the noise.

C.2 Fixed-Frequency Interference

At frequencies below 22 MHz, much interference due to ionospherically propagated signals from fixed-frequency transmitters was observed. Similar interference was also occasionally noted at higher frequencies, due to ground-wave propagation from more nearby transmitters, particularly at frequencies near 27 MHz.

Fixed-frequency interference was typified by a [redacted] duration, large amplitude burst at the receiver outputs as the narrow-band receivers were swept across the bandwidth of the interfering transmission and the phase-sensitive detectors were overdriven. The duration of the burst was equal to the length of time the interference remained within the 10 kHz bandwidth of the phase-sensitive detector stage, and for a 100 kHz/sec sweep rate, this time was typically of order 0.1 second. The effective duration of the burst could, of course, be lengthened further by the finite response time of the narrow-band low-pass output filters. The peak amplitudes of a fixed-frequency interference bursts were observed to range from 0.5 to 5 volts or more, depending on the interfering signal strength, and this type of interference usually disrupted the echo phase coherency by overriding the desired echo signal.

APPENDIX D

SECONDARY TRAIL GEOMETRY

D.0 Introduction

This appendix comprises an investigation of the geometry associated with the hypothesis of meteoroid fragmentation. It is assumed that the meteoroid fragments in the $(\hat{n}_o, \hat{\ell})$ plane and that an echo is subsequently observed from the secondary trail caused by the fragment, at an apparent axial distance ℓ from the main echo specular reflection point. It is assumed that the trails are formed in a stationary atmosphere, and the secondary echo is observed as soon as the secondary trail has been formed. In practice, this may not be the case, since either the secondary meteoroid may not have begun to ablate at the point where the specular reflection condition occurs, or conversely, the secondary meteoroid may have burned out by that point. In either case, however, wind shears could rotate the secondary trail until the specular reflection condition is achieved, and an echo reflection from the secondary trail would then be observed. This point is discussed further in the main text of the thesis (Sections 5.1.5, 5.2.5 and 5.3.4). It is also assumed that the mass of the fragment is negligible, so that the path of the remainder of the meteoroid is undeviated.

D.1 The Geometry

The geometry of the fragmentation of a meteoroid incident at a zenith angle χ and casting off a fragment at an angle $\delta\chi$ in the $(\hat{n}_o, \hat{\ell})$ plane is shown in Figure D.1. This diagram is strictly applicable to the backscatter case only, but Table 5.1 shows that for the forward-

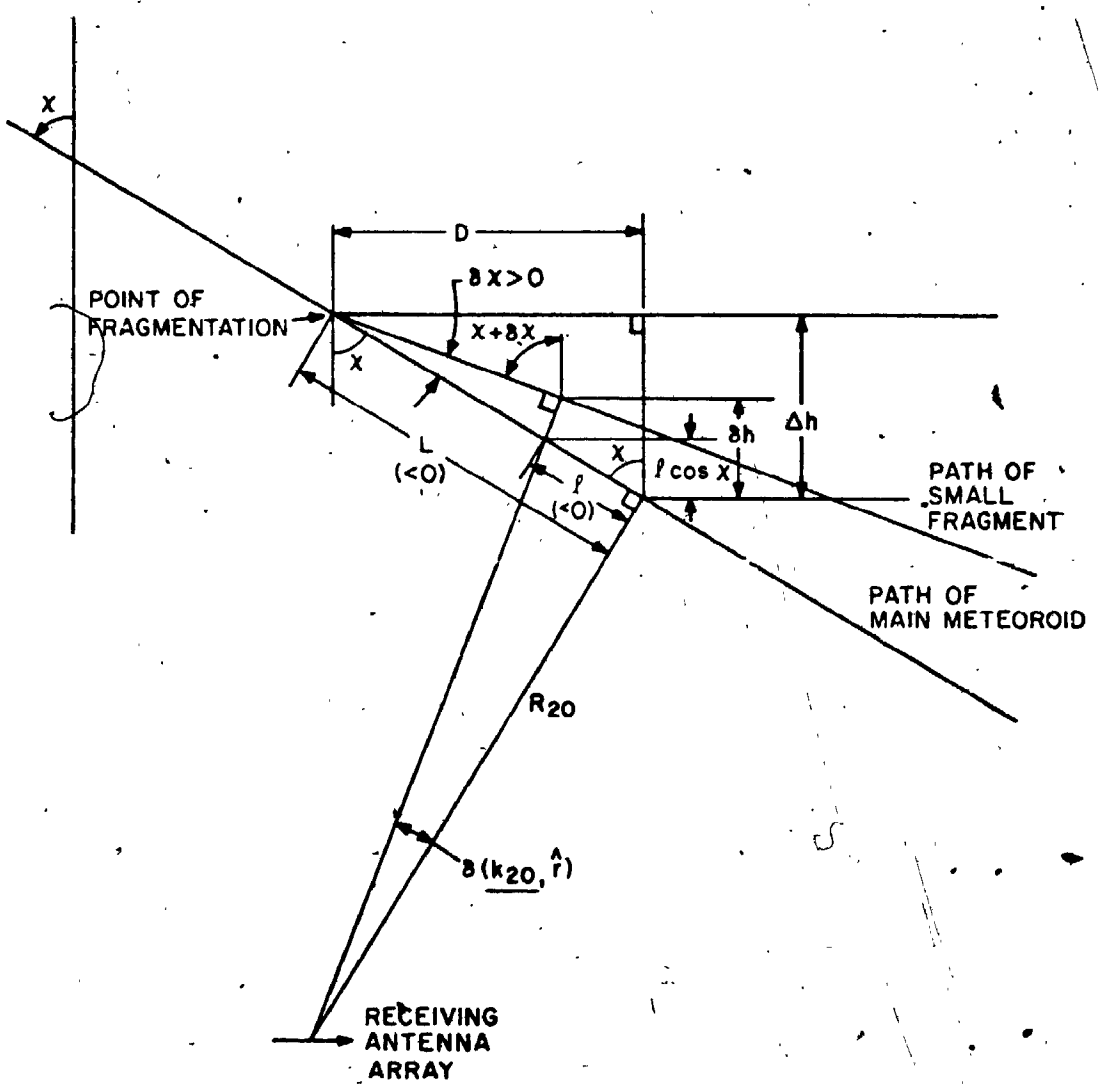

Figure D.1. Secondary trail scattering geometry

scatter meteor echoes under investigation, the $(\hat{n}_e, \hat{\ell})$ plane is almost perpendicular to the transmitter-receiver axis and therefore the diagram is valid to a good approximation.

From the diagram, the equations (D.1) and (D.2) follow:

$$\Delta h = -L \cos \chi \tag{D.1}$$

$$\Delta h - \delta h = -(L-\ell) \cos \delta\chi \cos(\chi+\delta\chi) \tag{D.2}$$

Here ΔH (>0) is the vertical distance (in kilometres) above the main echo specular reflection point at which the meteoroid fragmented, L (<0) is the distance (in kilometres) along the trail axis from the main echo specular reflection point to the fragmentation point, χ is the zenith angle (in radians) of the trail, δh (>0) is the actual height difference (in kilometres) between the secondary and main echo specular reflection points, ℓ (≤ 0) is the apparent axial distance (in kilometres) between the secondary and main echo specular reflection points and $\delta\chi$ is the angle of divergence (in radians) between the main and secondary meteor paths. The distance R_{20} (in kilometres) is the distance from the main echo specular reflection point to the receiving antenna array and $(\underline{k}_{20}, \hat{r})$ is the differential angle-of-arrival between the main and secondary echo signals.

By eliminating the variable L between eqns. (D.1) and (D.2), an exact expression for Δh in terms of the remaining variables can be obtained:

$$\Delta h = \frac{\delta h + \ell \cos \delta\chi \cos(\chi+\delta\chi)}{1 - \cos \delta\chi \cos(\chi+\delta\chi)/\cos \chi} \tag{D.3}$$

For the case $\delta\chi << 1$, as obtained for the present data, the equation for Δh becomes:

$$\Delta h = \frac{\delta h + \ell \cos \chi}{\delta\chi \tan \chi} - \ell \cos \chi \qquad (D.4)$$

It is this last equation which was used in Chapter 5.

APPENDIX E

DYNAMICS OF METEOROID FRAGMENTATION

E.0 Introduction

There are two major dynamical considerations which must be taken into account in order to decide whether or not the meteoroid fragmentation hypothesis is plausible. The first is the consideration of the amount of energy required to impart finite separation velocities to the two meteoroid fragments after fragmentation has occurred - this energy would have to be a small fraction of the kinetic energy of the unfragmented meteoroid, if the particles are not to undergo dramatic decelerations in their direction of forward motion. The second consideration is based on the conservation of momentum, which determines the angular deviations of the larger and smaller particles from the trajectory of their centre of mass. The deviation of the larger particle would have to be small (a fraction of a degree) or else the geometric techniques used to determine the location of the trail, as described in Chapter 3 and Appendix B, could be expected to lead to grossly erroneous results. The results of Chapter 5 implied that this was not the case.

E.1 Some Elementary Physics

The first of the three basic conservation relations describing the situation is the conservation of energy:

$$\Delta E = \frac{1}{2} m_1 v_1^2 + \frac{1}{2} m_2 v_2^2 \qquad (E.1)$$

where m_1 is the mass of the larger fragment and m_2 is the mass of the smaller; v_1 and v_2 are the velocities of the larger and smaller fragments in the centre of mass reference frame; and ΔE is the incremental amount energy which must be input to the meteoroid in order to impart finite separation velocities to the already severed fragments. This energy, as well as that required to actually fracture the meteoroid, is presumed to come from the frictional heating effect of the meteoroid's plunge through the atmosphere.

The second conservation relation is the conservation of momentum:

$$m_1 v_1 = m_2 v_2 \tag{E.2}$$

and the third relation is the conservation of mass:

$$m_1 + m_2 = m_0 \tag{E.3}$$

where m_0 is the mass of the unfragmented meteoroid. The geometry of the vector velocities is described in Figure E.1.

If the ratio of the mass of the smaller fragment to the mass of the unfragmented meteoroid is denoted by ρ_M, i.e.,

$$\rho_M = m_2/m_0 \tag{E.4}$$

and the kinetic energy of the unfragmented meteoroid is denoted by E_o, i.e.,

$$E_o = \frac{1}{2} m_o v_o^2 \tag{E.5}$$

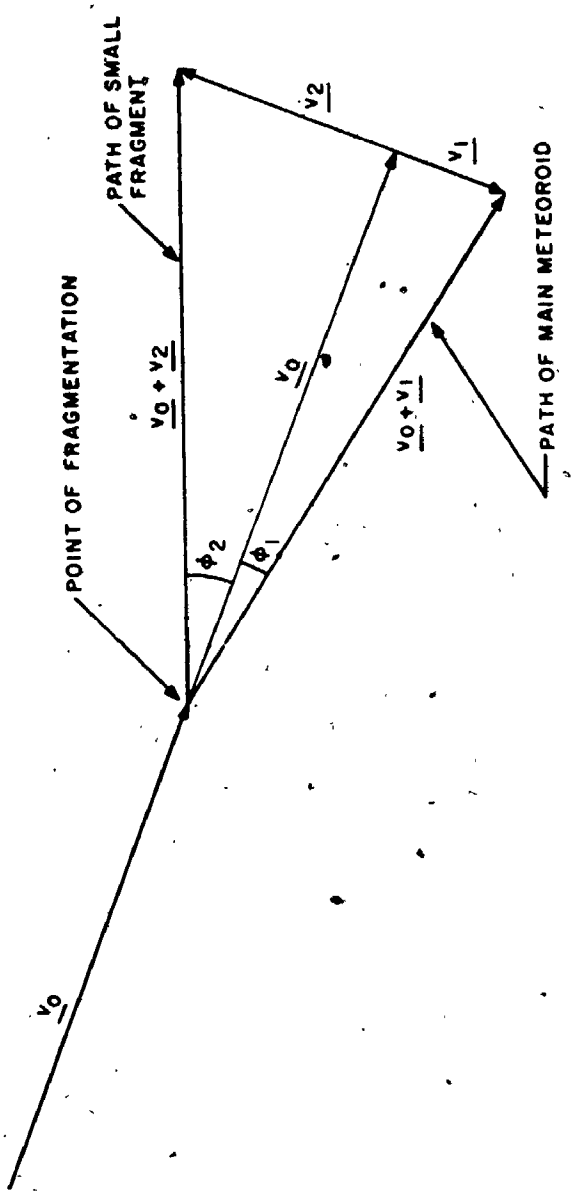

Figure E.1. The geometry of meteoroid fragmentation

some straightforward algebraic manipulation of eqns. (E.1) - (E.5) leads to the results

$$\frac{\Delta E}{E_o} = \frac{\rho_M}{1 - \rho_M} \tan^2 \phi_2 \qquad (E.6)$$

and

$$\phi_1 = \tan^{-1} \left\{ \frac{\rho_M}{1 - \rho_M} \tan \phi_2 \right\} \qquad (E.7)$$

where the angles ϕ_1 and ϕ_2 are the angular deviations of the larger and smaller fragments respectively from the centre of mass trajectory. These angles are also defined in Figure E.1. The simplifying assumption that $\underline{v}_1$ and $\underline{v}_2$ are perpendicular to $\underline{v}_0$ has been made in this derivation.

Solutions for $\Delta E/E_o$ and ϕ_1 for selected reasonable values of ρ_M and ϕ_2 have been presented in Table E.1. It can be seen there that the essential requirements for small $\Delta E/E_o$ and ϕ_1 are easily met if either the mass ratio ρ_M or the angle ϕ_2 is small.

TABLE E.1

Some Theoretical Examples of Fragmentation Parameters

ρ_M	$\phi_2 = 3^o$		$\phi_2 = 6^o$		$\phi_2 = 9^o$	
	$\Delta E/E_o$	ϕ_1	$\Delta E/E_o$	ϕ_1	$\Delta E/E_o$	ϕ_1
0.025	7.04×10^{-5}	0.08	2.83×10^{-4}	0.15	6.43×10^{-4}	0.23
0.050	1.45×10^{-4}	0.16	5.81×10^{-4}	0.32	1.32×10^{-3}	0.48
0.075	2.23×10^{-4}	0.24	8.96×10^{-4}	0.49	2.03×10^{-3}	0.74
0.100	3.05×10^{-4}	0.33	1.23×10^{-3}	0.67	2.79×10^{-3}	1.01
0.125	3.92×10^{-4}	0.43	1.58×10^{-3}	0.86	3.58×10^{-3}	1.30
0.150	4.85×10^{-4}	0.53	1.95×10^{-3}	1.06	4.43×10^{-3}	1.60

REFERENCES

Appleton, E.V., (1930), *On some measurements of the equivalent height of the atmospheric ionised layer*, Proc. Roy. Soc., A126, 542-569.

Bedinger, J.F., H. Knaflich, E. Manring and D. Layzer, (1968), *Upper-atmosphere winds and their interpretation - I. Evidence for strong nonlinearity of the horizontal flow above 80 km*, Planet. Space Sci., 16, 159-193.

Brown, N., (1972), *A Radio Study of Meteoric Ionization*, Ph.D. Thesis, University of Adelaide.

Brown, N. and W.G. Elford, (1971), *Radio echoes from randomly ionized meteor trails*, J. Atmosph. Terr. Phys., 33, 1659-1666.

Cook, A.F., M.R. Flannery, H. Levy II, R.E. McCrosky, Z. Sekanina, C.-Y. Shao, R.B. Southworth and J.T. Williams, (1972), *Meteor Research Program*, NASA Contractor Report NASA CR-2109.

Dolph, C.L., (1946), *A current distribution for broadside arrays which optimizes the relationship between beam width and side-lobe level*, Proc. IRE, 34, 335-348.

Eastwood, E. and K.A. Mercer, (1948), *A study of transient radar echoes from the ionosphere*, Proc. Phys. Soc., 61, 122-134.

Eshelman, V.R., (1952), *Mechanisms of Radio Reflection from Meteoric Ionization*, Stanford University Electronics Res. Lab. Report 49, July 1952.

Gold, B. and C.M. Rader, (1969), *Digital Processing of Signals*, McGraw-Hill Book Company, Inc., New York, Toronto, London.

Greenhow, J.S., (1952), *Characteristics of radio echoes from meteor trails, III: The behavior of the electron trails after formation*, Proc. Phys. Soc., 65, 169-181.

Greenhow, J.S. and E.L. Neufeld, (1955), *The diffusion of ionized meteor trails in the upper atmosphere*, J. Atmosph. Terr. Phys., 6, 133-140.

Hatch, J.F., W. Struszynski and H. Thurgood, (1966), *The Marconi Eight Aerial Adcock H.F. Direction Finder Type S.48D*, Marconi Rev. XXIX, No. 160, 1-23.

Hawkes, R.L. and J. Jones, (1975), *A quantitative model for the ablation of dustball meteors*, Mon. Not. R. astr. Soc., 173, 339-356.

Hemenway, C.L. and R.K. Soberman, (1962), *Studies of micrometeorites obtained from a recoverable sounding rocket*, Astron. J., 67, 256-266.

Hey, J.S. and G.S. Stewart, (1947), *Radar observations of meteors*, Proc. Phys. Soc., 59, 858-883.

Hines, C.O. and P.A. Forsyth, (1957), *The forward-scattering of radio waves from overdense meteor trails*, Can. J. Phys., 35, 1033-1041.

Hughes, D.W., (1974), *Even small meteoroids are fluffy*, Nature, 248, 99.

Jacchia, L.G., (1955), *The physical theory of meteors. VIII. Fragmentation as cause of the faint-meteor anomaly*, Astrophys. J., 121, 521-527.

Jones, J., (1969), *The reflection of radio waves from irregularly ionized meteor trains*, Planet. Space Sci., 17, 1519-1526.

Jones, J. and J.G. Collins, (1974), *On the validity of certain approximations in radio meteor echo theory*, Mon. Not. R. astr. Soc., 168, 433-449.

Jones, J. and R.L. Hawkes, (1975), *Television observations of faint meteors - II. Light curves*, Mon. Not. R. astr. Soc., 171, 159-169.

Jones, J. and B.A. Read, (1972), *The effect of wind shear gradients on underdense radio meteor decay times*, Can. J. Phys., 50, 1277-1281.

Jones, L.F., (1933), *A study of the propagation of wavelengths between 5 and 8 meters*, Proc. IRE, 21, 349-386.

Manning, L.A., (1953), *The strength of meteoric echoes from dense columns*, J. Atmosph. Terr. Phys., 4, 219-225.

Manning, L.A., (1959), *Oblique echoes from over-dense meteor trails*, J. Atmosph. Terr. Phys., 14, 82-93.

Manning, L.A., (1963), *Ray-path calculation of over-dense meteor echo strength*, J. Atmosph. Terr. Phys., 25, 182-183.

McIntosh, B.A., (1969), *The effect of wind shear on the decay constant of meteor echoes*, Can. J. Phys., 47, 1337-1341.

McKinley, D.W.R., (1961), *Meteor Science and Engineering*, McGraw-Hill Book Company, Inc., New York, Toronto, London.

McKinley, D.W.R. and P.M. Millman, (1949), *A phenomenological theory of radar echoes from meteors*, Proc. IRE, 37, 364-375.

Millman, P.M., (1973), *Meteors, Fireballs and Meteorites*, in the Observer's Handbook 1973, The Royal Astronomical Society of Canada: Toronto, page 75.

Phillips, E., (1969), *Wind structure from the amplitude fluctuations in persistent radio meteor echoes*, Planet. Space Sci., 17, 553-559.

Pierce, J.A., (1938), *Abnormal ionization in the E-region of the ionosphere*, Proc. IRE, 26, 892-902.

Revah, I., (1969), *Etude des vents de petite échelle observés au moyen des traînées météoriques*, Ann. Geophys., 25, 1-45.

Riblet, H.J., (1947), Discussion on *A current distribution for broadside arrays which optimizes the relationship between beam width and side-lobe level*, Proc. IRE, 35, 489-492.

Rice, D.W., (1964), *Inhomogeneities in Underdense Meteor Trails*, Ph.D. Thesis, University of Western Ontario.

Rice, D.W. and P.A. Forsyth, (1963), *Variations in meteoric radio signal decay rates*, Can. J. Phys., 41, 679-690.

Rice, D.W. and P.A. Forsyth, (1964), *The distribution of ionization along underdense meteor trails*, Can. J. Phys., 42, 2035-2047.

Rice, S.O., (1944), *Mathematical analysis of random noise I-II*, Bell System Tech. J., 23, 282-332.

Schafer, J.P. and W.M. Goodall, (1932), *Observations of Kennelly-Heaviside layer heights during the Leonid meteor shower of November, 1931*, Proc. IRE, 20, 1941-1945.

Skellett, A.M., (1931), *The effect of meteors on radio transmission through the Kennelly-Heaviside layer*, Phys. Rev., 37, 1668 (letter).

Skellett, A.M., (1932), *The ionizing effect of meteors in relation to radio propagation*, Proc. IRE, 20, 1933-1940.

Skellett, A.M., (1935), *The ionizing effect of meteors*, Proc. IRE, 23, 132-149.

Stegen, R.J., (1953), *Excitation coefficients and beamwidths of Tschebyscheff arrays*, Proc. IRE, 41, 1671-1674.